# Image-Based Modelling of the Electrophysiological and Structural Effects of Fibrosis on the Mechanisms of Atrial Fibrillation

Morgan, Ross John

*Awarding institution:*
King's College London

# Image-Based Modelling of the Electrophysiological and Structural Effects of Fibrosis on the Mechanisms of Atrial Fibrillation

*A thesis submitted for the fulfilment of the requirements for the degree of Doctor of Philosophy in the*

Division of Imaging Sciences and Biomedical Engineering,
Faculty of Life Sciences and Medicine,
King's College London

**Ross Morgan**

**2016**

**Contents**

# List of abbreviations

| | |
|---|---|
| $I_{X,Y}$ | Ionic current (of ion X and cell-type Y) (pA/pF) |
| $I_{CaL}$ | L-type calcium current (pA/pF) |
| $I_{Cl}$ | Chlorine current (pA/pF) |
| $I_{K1}$ | Inward rectifier potassium current (pA/pF) |
| $I_{KACh}$ | Acetylcholine-activated potassium current (pA/pF) |
| $I_{KS}$ | Slow potassium current (pA/pF) |
| $I_{Kur}$ | Ultra rapid Potassium current (pA/pF) |
| $I_{Na}$ | Fast sodium current (pA/pF) |
| $I_{to}$ | Transient outward current (pA/pF) |
| 4-AP | 4-aminopyridine |
| AF | Atrial fibrillation |
| AP | Action potential |
| APA | Action potential amplitude (mV) |
| APD | Action potential duration (ms) |
| AS | Atrial septum |
| AV | Atrio-ventricular (i.e. node, valve) |
| BB | Bachmann's bundle |
| BZ | Border zone |
| $Ca^{2+}$ | Calcium ion |
| CFAE | complex fractionated atrial electrograms |
| CHF | Chronic heart failure |
| $Cl^{-2}$ | Chlorine ion |
| CRN | Courtemanche Ramirez Nattel (model) |
| CT | Cristae terimnalis |
| CV | Conduction velocity (m $s^{-1}$) |
| Cx-(40/43/45) | Conexins (of type: 40, 43 or 45) |
| DAD | Delayed after depolarisation |
| $D_L$ ,$D_T$ | Diffusion coefficients (longitudinal and transverse) ($mm^2$ $ms^{-1}$) |
| EAD | Early after depolarisation |
| ECV | Extracellular volume |
| ERP | Effective refractory period |
| FK | Fenton-Karma (model) |

| | |
|---|---|
| ICD | Intercalated disks |
| IR | Ionic remodelling |
| IVC | Inferior vena cava |
| $K^+$ | Potassium ion |
| LA | Left atrium |
| LAA | Left atrial appendage |
| LGE MRI | Late gadolinium enhance MRI |
| LIPV | Left inferior pulmonary vein |
| LSPV | Left superior pulmonary vein |
| LV | Left ventricle |
| M-F | Myocyte-fibroblast (coupling) |
| MRI | Magnetic resonance imaging |
| pAF | Persistent atrial fibrillation |
| PDE | Partial differential equation |
| PM | Pectinate muscles |
| PSIR | Phase-sensitive inversion recovery (MRI) |
| PV | Pulmonary veins |
| RA | Right atrium |
| RAA | Right atrial appendage |
| RF | Radiofrequency (ablation catheter) |
| RIPV | Right inferior pulmonary vein |
| RMP | Resting membrane potential |
| RSPV | Right superior pulmonary vein |
| RV | Right ventricle |
| SAN | Sino-atrial node |
| SNR | Signal to noise ratio |
| SR | Sinus rhythm |
| SVC | Superior vena cava |
| TGF-β | Growth factor |
| WL | Wavelength (m) |

# Abstract

ABSTRACT OF THESIS submitted by Ross Morgan

For the degree of Doctor of Philosophy and titled

Image-Based Modelling of the Electrophysiological and Structural Effects of Fibrosis on the Mechanics of Atrial Fibrillation

April 2016

Atrial fibrillation (AF) is a degenerative cardiac arrhythmia characterised by high incidence rate and limited effectiveness of clinical treatments. Fibrosis is one of the major pathological factors linked with AF progression. However, mechanistic links between this pathology and AF arrhythmogenesis are incompletely understood. This project investigates the diverse arrhythmogenic effects of fibrosis using computational model of the human atria, which integrates electrophysiological and structural changes associated with fibrosis. Structural data is reconstructed based on magnetic resonance imaging (MRI) from AF patients.

The computational model of the 3D human atria integrated the Visible Female cardiac geometry, rule-based fibre orientation, region-specific atrial electrophysiology and its changes due to AF-induced ionic remodelling. Fibrosis was modelled by integrating (i) a novel electrophysiologically detailed model for a single atrial fibroblast, (ii) electrotonic myocyte-fibroblast (M-F) coupling, (iii) structural effects of fibrosis on the anisotropy of atrial tissue and (iv) either random or patient-specific distributions of fibrosis in the 3D atrial model. Patient-specific distributions were reconstructed from late-gadolinium enhanced (LGE) MRI.

At the single-cell level, electrotonic M-F coupling via gap junctions resulted in changes of the atrial myocyte electrophysiological properties, including the resting membrane potential, action potential duration (APD) and its restitution, regional APD heterogeneity, effective refractory period and cell excitation threshold. At the 3D atria level, these changes translated into the altered susceptibility for atrial re-entry. Additional changes of the tissue anisotropy and heterogeneity, both associated with non-uniform fibrosis in the atria, resulted in the breakdown of re-entry into multiple rotors and wavelets, which is characteristic of AF.

Application of LGE MRI enabled the segmentation of patchy fibrosis from AF patients. An image processing and modelling pipeline was developed to maps the distributions of fibrosis into the 3D atrial model and investigate the effects of regional fibrosis patches on the genesis of AF. Simulations the patient-specific

model revealed pinning of re-entrant waves primarily at the border zone of dense fibrosis patches. Patient-specific atrial wall thickness was also reconstructed using novel PSIR MRI protocol and integrated into the 3D model. This non-uniform structural feature provided additional locations for the wave pinning in regions of minimum atrial wall thickness.

In summary, the developed MRI processing and computational modelling pipeline has been applied for dissecting the multiple effects of fibrosis in the genesis of AF. Novel insights provided by the image-based models pave a way for understanding of the disease and providing treatment on a patient-by-patient basis.

## Declaration

I declare that the thesis hereby submitted to King's College London for the degree of Doctor of Philosophy has not been previously submitted for a degree at this, or any other University; that it is my work in design and in execution and that all material contained therein has been duly acknowledged.

## Copyright statement

## Dedication

This work is dedicated to Ms Leanne Black, who throughout the writing up phase was thoroughly neglected and without her love and support it would likely not have been finished.

## Acknowledgments

First and foremost I would like to thank Dr Oleg Aslanidi, for his supervision and support over the course of my PhD. Looking back at my first year I have learnt and achieved a great deal, none of which would have been possible without his help. I would also like to thank Kawal Rhode for his support during this work. Marta Varela deserves a special mention, as a Matlab whizz-kid, there was never a problem or question that she couldn't solve.

Our collaborators were also instrumental in this work and I would personally like to thank Dr Martin Krueger and Dr Gunnar Seemann from Karlsruhe institute of technology for the use of their excellent fibre orientation geometry. I would also like to thank Dr Michael Colman for his help and his work on regional heterogeneities and ionic remodelling. A great deal of this work was reliant on obtaining LGE MRI data from AF patients, for which, I would like to thank Dr Henry Chubb.

I am greatly indebted to my family (Dr Frances Ross, Dr Fergus Morgan and Mr Patrick Morgan) and my girlfriend Ms Leanne Black for their help in proof reading my thesis as well as their continued psychological support throughout the process.

# Supporting Publications

‘Electrophysiological and structural effects of fibrosis on the mechanisms of atrial fibrillation: Insights from multi-scale human atrial modelling.’
Morgan RJ, Chubb H, Colman M, Aslanidi O. *Frontiers in Physiology.* (Submitted)

‘Novel MRI Technique Enables Non-Invasive Measurement of Atrial Wall Thickness.’
Varela M, Morgan R, Theron A, Peyroteo M, Piqueiro L, Henningsson M, Aljabar P, Chubb H, Schaeffter T, Kolbitsch C, Aslanidi O. *European Heart Journal – Cardiovascular Imaging.* (Submitted)

‘Towards Patient-Specific Modelling of Lesion Formation During Radiofrequency Catheter Ablation for Atrial Fibrillation.’
Soor N, Morgan R, Varela M, Aslanidi O. *Conference Proceedings of the IEEE Engineering in Medicine and Biology Society*, 2016. (Accepted)

‘3D high-resolution atrial wall thickness maps using black-blood PSIR.’
Varela M, Kolbitsch C, Theron A, Morgan R, Henningsson M, Schaeffter T, Aslanidi O. *Journal of Cardiovascular Magnetic Resonance* 17: P239/1-2, 2015.

‘Evaluating effects of fibrosis in atrial arrhythmogenesis using 3D computational modelling.’
Morgan R, Colman M, Kruger M, Seemann G, Rhode K, Aslanidi O. *Computing in Cardiology* 2014: 765–768, 2014.

‘Ionic mechanisms of triggered activity in atrial cell models.’
Varela M, Morgan R, Ghavami N, James S, Aslanidi O. *Computing in Cardiology* 2014: 1021–1024, 2014.

‘Patient-specific modelling of atrial fibrosis and conduction.’
Morgan R, Rhode K, Aslanidi O**.** *Journal of Electrocardiology* 46: e27–e28, 2013.

‘Modelling the effects of fibrosis-associated electrical heterogeneity in atrial fibrillation.’
Morgan RJ, Colman M, Chubb MH, Varela M, Aslanidi O. *Europace* 17: iii13, 2015. (Conference Proceedings)

‘Atlas of atrial wall thickness as a tool for catheter ablation procedures.’
Varela M, Morgan R, Theron A, Peyroteo M, Piqueiro L Henningsson M, Paul Aljabar P, Kolbitsch C, Schaeffter T, Aslanidi O. *Atrial Signals,* 2015. (Conference Proceedings)

‘Electrotonic and structural effects of fibrosis on the genesis of atrial fibrillation: Insights from 3D human atria model.’
Morgan R, Colman M, Kruger M, Seemann G, Rhode K, Aslanidi O. *Virtual Physiological Human Conference,* 2014. (Conference Proceedings)

‘Towards Patient Specific Modelling of Atrial Fibrosis and Arrhythmogenesis.’
Morgan R, Aslanidi O. *MEC Annual Meeting,* 2013. (Conference Proceedings)

# 1. Introduction

Atrial fibrillation (AF) is a common degenerative cardiac arrhythmia. The incidence rate of this condition is high, however current clinical treatments have limited effectiveness. It develops in the atria and produces an irregular heart rate, reducing the cardiac output of the organ. Although the condition is largely confined to the upper chambers of the heart and may be relatively benign, it is known to lead to severe complications such as stroke or congestive heart failure. The patient suffering from AF also has reduced quality of life due to the lower cardiac output which can cause fatigue and requires long-term medication.

The progression of the disease is such that up to 24% of paroxysmal patients will progress to persistent AF[1] and 31% will progress to permanent AF[2]. This process is self-sustaining, as described by the idiom "AF begets AF". A further complication is that treatments become less effective as the duration of AF increases.[1] A definitive cause for the disease progression is unknown, but various functional and structural factors have been associated with arrhythmogenesis.

The risk of stroke in AF patients is 5 times greater than non-sufferers.[3] Due to the lack of organised atrial contraction, blood can stagnate within the atria, and lead to thrombus formation. Over a quarter of patients diagnosed with AF also have congestive heart failure (CHF), with 16% of AF diagnoses developing CHF later in life[4]. The co-morbidity of these conditions leads to greatly increased risks of cardiovascular events and fatalities.[5] The lifetime risk of developing the disorder after the age of 40 is 26% for men, and 23% for women[6] with global prevalence in

2010 being 33.5 million[7]. With a globally aging population and continued improvements to life expectancies, this number will continue to grow.

Existing treatments have varied and limited levels of success which leads to high rates of recurrence. Treatments such as, front-line anti-arrhythmic drug therapy and emerging catheter ablation are characterised by ~30-50% recurrence. This shows that a better understanding of the disorder is required for the development of more effective treatments. Due to the complexity of AF and a large number of underlying structural and electrophysiological factors, a single definitive cause has not yet been identified. The limitations of current in-vivo electrophysiology recording methods are a major hindrance for experimental AF studies.

Biomedical engineering is increasingly relying on computational modelling in order to investigate the physiological and pathological factors that contribute to cardiovascular disease, including AF arrhythmogenesis. Modelling allows in-silico simulation of atrial electrophysiology and non-invasive dissection of the complex cell-to-organ factors underlying the development and progression of AF.

## 1.1. Aims of the thesis

Atrial fibrosis is one of the major pathological factors associated with AF progression. There is a strong correlation between AF duration and increased atrial fibrosis, which has been used for AF condition stratification. This form of structural remodelling leads to increasing collagen deposits within the tissue and it has been hypothesised that fibrotic invasion of the myocardium has arrhythmogenic effects. Moreover, ablation of fibrotic areas identified from clinical imaging or electro-anatomical mapping can significantly improve the ablation therapy success rates[8,9].

However, due to the difficulty in matching the recordings of AF patient electrophysiology with the underlying tissue structure, this has not yet been supported with solid evidence.

The aim of this thesis is to develop a computational model to investigate the effects of fibrosis on the generation and sustenance of AF. To accomplish this goal, a multi-scale 3D whole-atria model was created to integrate several state-of-the-art elements developed in collaboration with leading groups. The model includes human image-based atrial structure and established cell electrophysiology models.

Individual aims for each chapter have been identified to investigate the overall effects of fibrosis and atrial structure:

1. Investigate the effects of myocyte-fibroblast coupling in single cell simulations,
2. Investigate the 3D effects of homogenous fibrosis,
3. Investigate patient specific aspects of fibrosis,
4. Investigate the variations and effects of atrial wall thickness on arrhythmogenesis.

The modelling results will be used to provide a mechanistic explanation for the success of ablation around fibrotic areas.

## 1.2. Thesis overview

The thesis is divided by topic of investigation; an overview of the structure of the thesis is detailed below.

*Chapter 2* introduces the problems faced in AF research and gives background information, from basic cardiac anatomy to mathematical modelling techniques, and outlines the methods used for the modelling, imaging and image processing.

*Chapter 3* provides details of the development of single cell models, including a single atrial fibroblast model and the myocyte-fibroblast coupling model. This chapter also explores the dynamic effects of these models, such as the effects of fibroblasts on myocyte electrophysiology.

*Chapter 4* describes the investigation into the 3D dynamics of the human atrial model. Specifically, it looks into the electrophysiological effects of uniform diffuse fibrosis within 3D atrial tissue. In addition the investigation of the effect of fibrosis-related tissue anisotropy on arrhythmogenesis is also described.

*Chapter 5* describes the investigation into patient-specific fibrosis. The image processing pipeline is described, which was developed to process late gadolinium enhanced MRI into a volumetric dataset compatible with the 3D atrial model. This chapter concludes with the in-silico findings of the 3D re-entrant wave dynamics in heterogeneous fibrosis distributions.

*Chapter 6* details the investigation into atrial wall thickness reconstructed from novel MRI data and its additional effects on AF arrhythmogenesis. Atrial wall thicknesses were measured from both AF patients and volunteers, and an atlas of volunteer thicknesses was created. Simulations using the reconstructed 3D atrial geometries were preformed to show the effects of wall thickness on electrophysiology.

*Chapter 7* provides an overview of the whole thesis, linking the conclusions for each chapter. It also assesses the clinical relevance for this work as well as assessing the limitations

# 2. Background

## 2.1. Cardiac anatomy

The heart is the primary mechanical driver for the human cardiovascular system. It is responsible for driving the transport of blood, containing oxygen and nutrients to and from all tissues in the body. The organ comprises of four chambers (Figure 1).

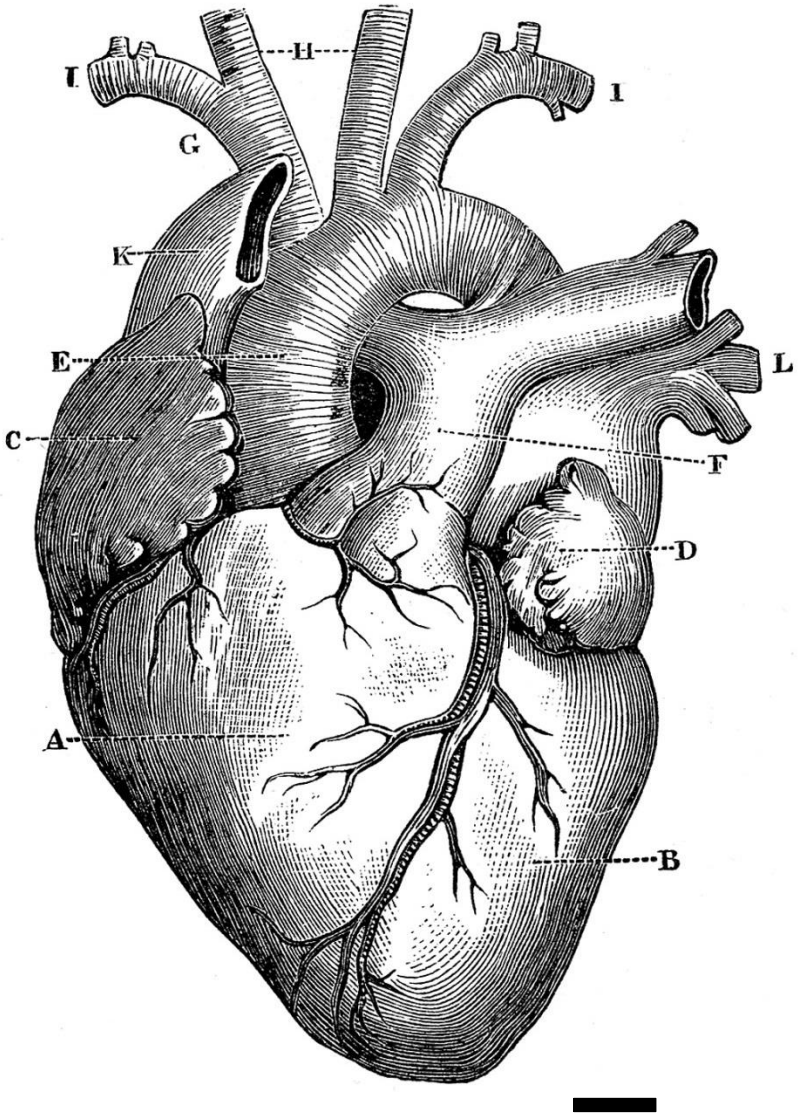


***Figure 1.*** *Illustration of cardiac anatomy. A. Right ventricle, B. Left ventricle, C. Right atrium, D. Left atrium, E. Aortic Arch, F. Pulmonary trunk, G-J. Carotid arteries, K. Superior Vena Cava, L. Pulmonary veins. This image is an open source resource. Black scale bar is 10mm.*

The two lower and larger chambers, the ventricles, provide the muscular contraction as the driving force for blood circulation. The atria are the two smaller superior chambers of the heart. The walls of the atria are much thinner (1-5mm) than the ventricles (11mm) due to lower mechanical workload. They also have no valves on the inflow vessels and therefore have a lower pressure capacity. The four chamber structure of the heart enables the separation of the pulmonary from the systemic circulation systems. This partitions the oxygenated blood and the de-oxygenated blood within the heart.

The left atrium (LA) is supplied with blood by the pulmonary veins (PV), the most common configuration of the veins is two entering on both the left and right sides. The chamber empties into the left ventricle (LV) via the mitral valve. The right atrium (RA) is supplied by the superior and inferior vena cava (SVC and IVC) and fills the right ventricle (RV) via the tricuspid valve.

The atria have several unique anatomical structures (Figure 2), which directly influence their functional and electrophysiological properties. Examples include the sinoatrial node (SAN) which generates the stimulus for cardiac contraction to the atrial septum (AS) which separates the blood volumes of the atria.

The atrial appendages in the LA and RA (LAA and RAA respectively) extend beyond the atria and over their respective ventricles. These chambers contain high density networks of pectinate muscles (PM), which are large muscle fibre bundles. The function of the appendages is disputed but it has been suggested that they increase

chamber volume prior to ventricular filling or act as a decompression chamber for periods of atrial hypertension[10].

The two atria are separated by the AS which prevents blood transfer between the atria, except in the foetus, where transfer is permitted through a leaflet opening known as the foramen ovale. At birth the decrease in pulmonary circulation pressure permanently closes the foramen ovale. The septum has a bilaminar muscular structure separated by connective tissue,[11] which reduces electrophysiological conduction across the structure and between atria.

The SAN is difficult to identify by observation due to its small size and macroscopic similarity to the surrounding myocardium. It can be identified histologically by the finer and more irregular fibre structure or by the presence of proteins responsible for its pacemaking function. The SAN is comprised of autonomously activating myocardial cells, moderated by the adrenergic and vagal nerves. It is responsible for initiating the electrophysiological waves that cause the organ to contract.

Several fibrous bundles facilitate trans-septal conduction between the atria. The largest of these is the Bachmann's bundle (BB). It runs from the top of the RA into the anterior tissue of the LA, the origin of the BB is located close to the SAN providing rapid progression of the wave into the LA. The coronary sinus (which is a coronary vein) and other smaller posterior septal conduction pathways have also been shown to promote trans-septal conduction[12].

The crista terminalis (CT) is a large fibrous bundle that is the junction between the right atrium and the right atrial appendage. It runs from the SVC to the IVC. As with

the BB, the CT accelerates conduction along the bundle. This increases the speed of wave propagation from the SAN (which is located at superior end of the CT) towards the ventricles.

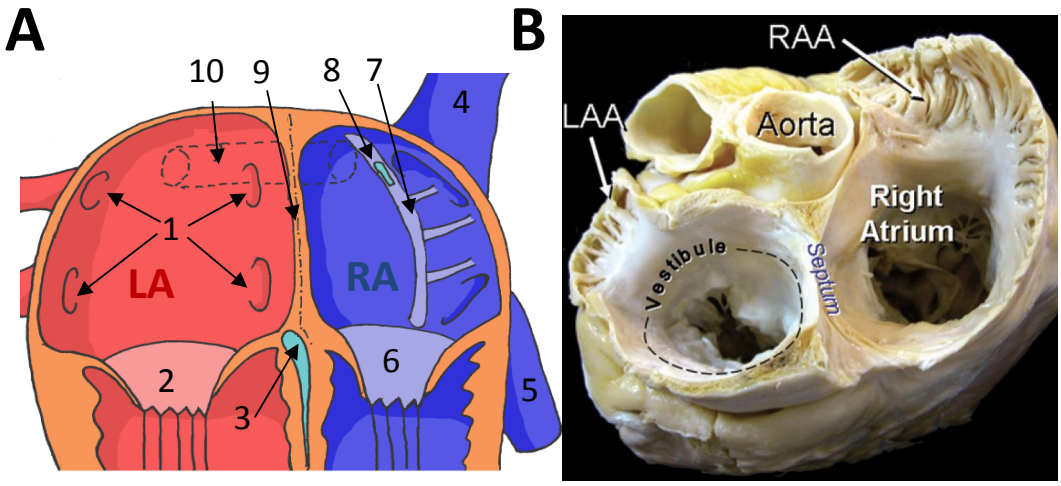


***Figure 2***. *Atrial structures and features. A is a schematic diagram of a coronal dissection through both atria. The main structures of the LA are the PV (1), the mitral valve (2), the LAA and the AV node (3). The main structures of the RA are the SVC and IVC (4,5), the tricuspid valve (6), RAA, CT (7) and SAN (8). Some structures are shared between the atria, and control conduction pathways: the atrial septum (9) which electrically separates the atria and the BB (10), a fibrous tissue which facilitates controlled inter-atrial conduction. B shows a lateral dissection through both atria and is sourced from Ho et al.*[13]

The tissue of all cardiac chambers is comprised of striated muscle and is relatively homogeneous in terms of cell diversity, with the main cell mass comprising of myocytes. Myocytes (Figure 3) provide the mechanical force for all muscular tissue. They are elongated, tubular cells and contain longitudinal myofibrils which allow the cell to contract. Unlike skeletal myocytes, cardiac myocytes have a single nucleus. The cells are connected end to end via intercalcated disks (ICD) which contribute to tissue synchrony by allowing ionic transfer between cells and act as anchoring points for myofibrils. The structure of bundles of fibres is optimal for continuous contractile effort, but it also promotes anisotropic conduction.

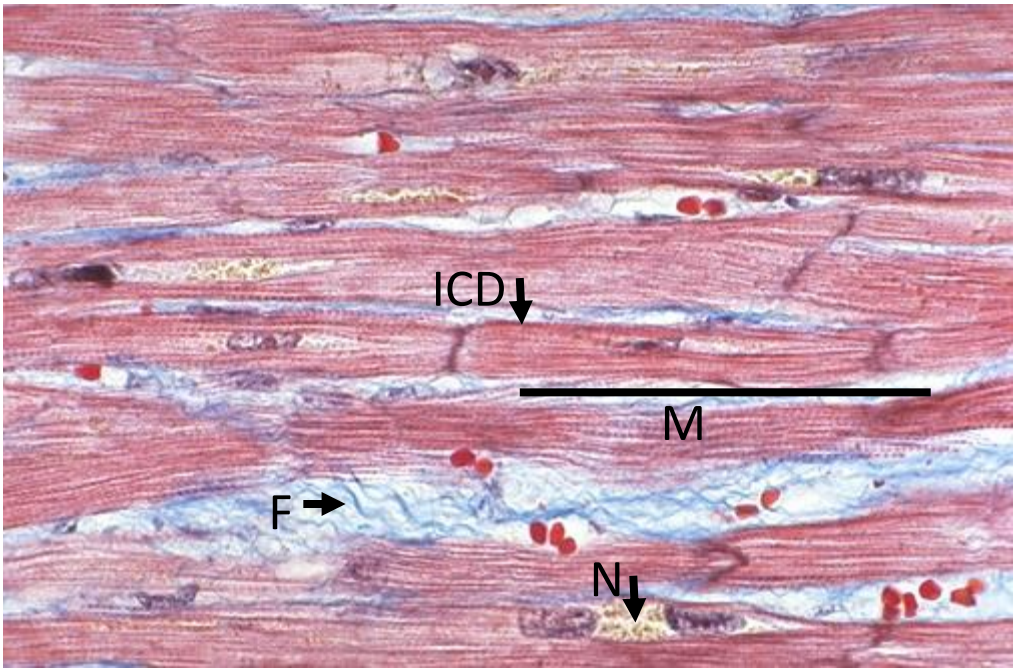


***Figure 3.*** *Illustration of the structure of atrial tissue using histology. The image is a trichrome stained histological slide of atrial myocardium. It shows the fibrous structure of the tissue and parts of the cell including the inter-calated disks (ICD) the nucleus (N) and fibrosis (F, stained in blue). A whole myocyte length of approximately 100 µm is indicated by the line M (myocytes are stained in red). Image reproduced with permission from WebPath*[(R)]14

Although the main function of the cell is to provide mechanical force for tissue contraction, the cell also acts as an electrical signal transceiver. This function is explored in more detail throughout the following section along with the facilitation of anisotropic conduction.

## 2.2. Atrial function

The main mechanical function of the atria is to facilitate the passage of blood to the ventricles uni-directionally via the atrio-ventricular (AV) valves. The stages of this process have passive (conduit phase) and active (booster pump phase) phases as well as an inactive filling (reservoir) stage. The atria also allow for the generation and ordered conduction of electrical excitation waves through the heart. These

waves originate in the SAN and initiate contraction of the cells as they pass through atrial and then ventricular tissues, regulating the contraction order of the heart chambers.

In sinus rhythm, the conduction of the electrical waves through the tissue must follow a regimented route. The electrical signal (action potential) is initiated in the RA by autonomously activating cells of the SAN. The wave then propagates across the RA aided by fast conduction along the CT and pectinate muscles, resulting in their contraction. Accelerated trans-septal conduction is promoted through the BB. The wave passes through the LA from top to bottom, ensuring its contraction after the RA. Simultaneously, propagation in the RA has reached the inferior wall and the AV node, which promotes conduction into the ventricles via the bundle of Hiss.

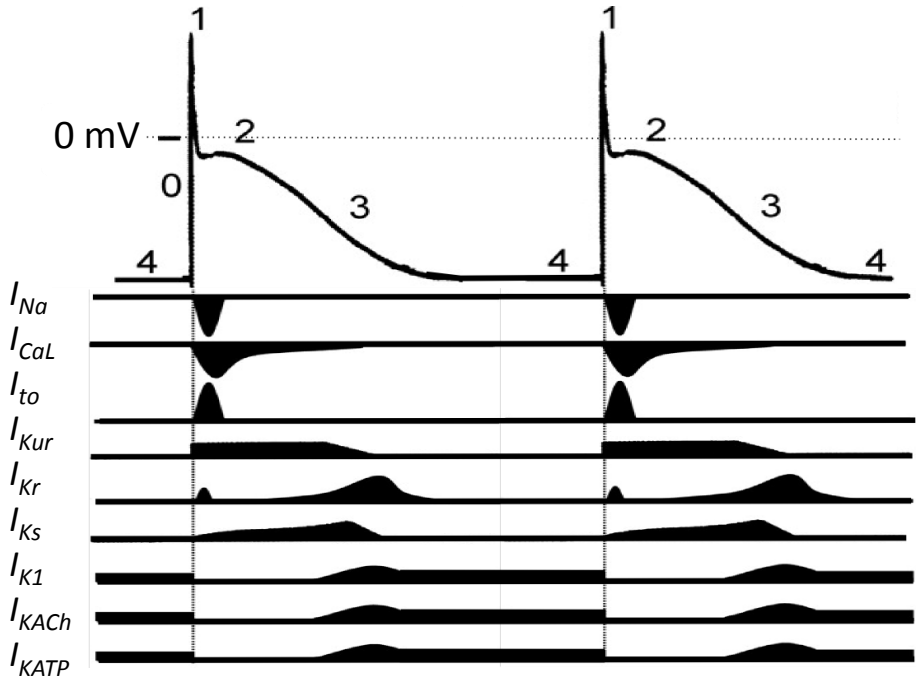


***Figure 4**. Atrial action potentials and traces of underlying ionic channel currents. The top plot shows a membrane voltage trace of two action potentials marking phases 1-4 as well as the active currents. $I_{Kur}$, $I_{KACh}$ are unique to atrial myocytes.*

The excitation waves responsible for initiating the heart contractions are sustained by a cascade of action potentials generated in each cardiac cell. Due to the capacitive properties of the cell membrane and ionic concentrations gradients across the membrane, myocytes can maintain a resting potential across the membrane. Through a series of voltage-dependent opening and closing of specific ionic channels in the membrane and the subsequent fluxes of ions across the membrane, the cells can create a “voltage spike” known as an action potential (AP). The ionic fluxes are driven by the potential and concentrations gradients across the membrane, whereas the voltage-dependence of ionic channels is based on conformational changes of the channel-forming proteins.

The major ionic channel currents seen in Figure 4B are activated in a specific sequence to generate a cardiac AP (Figure 4A). This differs from a neuronal AP by the plateau phase (phase 2), which gives cardiac AP a longer duration. This allows for a larger influx of calcium at this phase which activates the myofibrils, facilitating cellular contraction.

Phase 0 (depolarisation). The sodium current drives sodium ions into the cell, which rapidly increases the membrane potential. The sodium activation gate opens when a threshold membrane potential is exceeded, due to current flowing into the cell, from neighbouring cells or through an electrode injected through the cell membrane.

| Current | Direction | Name: Description | Phase | Subunit |
|---|---|---|---|---|
| $I_{Na}$ | In | Fast sodium current: Rapid depolarisation current that initiates the AP | 0 | NaV1.5 |
| $I_{to}$ | Out | Transient outward current: Response to depolarisation, begins to repolarise cell. | 1 | Kv4.3 |
| $I_{Cl}$ | In | Chloride current: Response to depolarisation, similar action to $I_{to}$ | 1 | |
| $I_{Kur}$ | Out | Ultra-rapid potassium current: Response to depolarisation, begins to repolarise cell | 1/2 | Kv1.5 |
| $I_{CaL}$ | In | L-type calcium current: Sustains the long AP plateau, responsible for contraction | 2 | Cav1.2 |
| $I_{Ks}$ | Out | Slow potassium current: Acts to repolarise the membrane later during the plateau | 2/3 | Kv7.1 |
| $I_{Kr}$ | Out | Rapid potassium current: Acts to repolarise the membrane early during the plateau | 3 | Kv11.1 |
| $I_{K1}$ | In/ Out | Inward rectifier potassium current: Repolarises the cell determining the resting potential | 4 | Kir2.1-2.3 |
| $I_{KACh}$ | Out | Acetylcholine-activated potassium current: Repolarising current and only active in the presence of acetylcholine | 4 | Kir3.1/3.4 |

**Table 1.** *Description of main ion channel currents responsible for the consecutive AP phases. Phase 1 (early repolarisation), as the sodium channels close, the transient outward current ($I_{to}$) activates causing a rapid repolarisation and the characteristic ("notch") in membrane potential.*

Phase 2 (plateau) is determined by L-type calcium channels opening and $Ca^{2+}$ ions entering the cell, which prevents the cell being immediately repolarised. During this period the cell physically contracts as the calcium ions initiate the contraction of the microfilaments. During this phase the major currents are in quasi-equilibrium, with calcium (inward) and potassium (outward) balancing each other and resulting in low net current[15].

Phase 3, when the $Ca^{2+}$ channels are closed, the net current is dominated by $K^{+}$ outflow from the cell, which starts to repolarise the cell and ultimately restores the resting potential (Phase 4).

The propagation of the AP waves through the tissue is permitted by the gap junctions, which are non-specific ionic channels present in the intercalated disks at the junction between cells. The gap junctions allow connected cells to exchange ionic charge and change the membrane potential; once a cell reaches a threshold potential, the sodium channel will activate and the AP will be triggered.

Abnormalities of AP generation at the single cell level are considered pro-arrhythmogenic. There are two main types of abnormal impulse, which are defined by the time they are activated within the action potential. Early after depolarisations (EADs) are activated during phases 2-3 and are more likely to occur when the action potential duration is longer. Delayed after- depolarisations (DADs) occur in late phase 3 or phase 4, when the cells are predominantly depolarised. Both EADs and DADs can act as initial triggers of abnormal waves leading to AF.

At the tissue level, the overall wave dynamics can be significantly affected by minimum reactivation time, known as the effective refractory period (ERP). The ERP effectively defines the wavelength of the propagating wave which is a determining factor in the generation of fibrillatory re-entrant circuits (see section 2.3 below). Wavelength (WL) isn't wholly defined by the ERP, but is a product of ERP and the conduction velocity (CV) (equation 1).

$$WL = CV \times ERP \quad (1)$$

The latter, in turn is dependent on the number of active gap junctions between the cells, the proximity of cells and the viability of the tissue. In sinus rhythm, the wavelength of propagating waves is sufficiently long (17cm[16]) that the atria can only accommodate a single wave (the average longitudinal diameter of the LA is 5.7cm[17]), effectively preventing re-entry of the wave. Therefore, structural or electrophysiological changes are required in order for AF to occur.

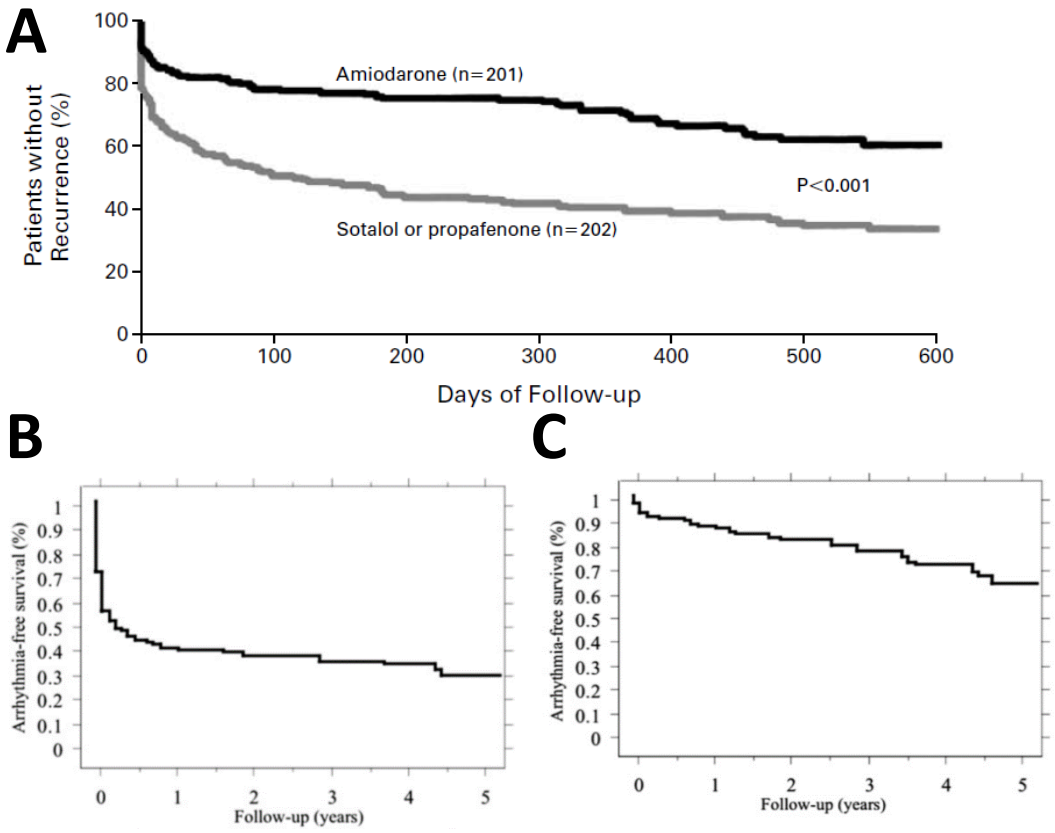


***Figure 5.*** *Recurrence rates of AF after treatments. Standard anti-arrhythmic drug (Sotalol/Propafenone) treatment has a long-term success rate of only about 40%. Although Amiodarone shows a higher effectiveness, it is toxic to the patient[18], limiting its longterm application. B. The follow up of a single ablation attempt has a minimum arrhythmia free survival of 30% (at 5 years). C. The follow up of arrhythmia free survival after multiple ablations, which increases to 65% at 5 years. Images from Weerasooriya et al.*[19]

## 2.3. Atrial Fibrillation

AF is the most common sustained cardiac arrhythmia[6] with an incidence of 2.66 million cases in the US in 2010. Although the arrhythmia may be relatively benign, the condition is known to lead to severe complications such as stroke or congestive heart failure. AF is often chronic and progressive, exhibiting a self-sustained and treatment-resistant nature. The aging population is a major contributing factor for the recent increase in AF incidence. AF is characterised by rapid and chaotic electrophysiological activation of the atrial tissue and is distinct from atrial flutter by its higher and more irregular frequency.

### 2.3.1. Current treatments

Current treatments for AF are limited, have low success rates and high rates of reoccurrence. There are currently three main therapeutic options for patients diagnosed with AF: drug therapies, cardioversion and catheter ablation.

Ablation therapy is used to block conduction in certain areas to in order to prevent AF stabilisation. The pulmonary veins have been identified empirically as sources of electrical activity sustaining AF and are most commonly used as a target for ablation[20]. The pulmonary veins are electrically isolated to prevent electrical interaction with the rest of the atria. The isolation is accomplished using a high energy radiofrequency (RF) catheter to cauterise the endocardial surface of the atria. The resulting thermal damage of the tissue leads to the creation of non-conductive areas. PV isolation has been shown to be effective in the treatment of paroxysmal AF with success rates of 65-80% for multiple surgeries and 40%[19] for single ablations (see Figure 5B). However, ablation procedures are invasive, can be

up to 5 hours long with significantly damage to the atrial tissue and have high recurrence rates.

The effects of different anti-arrhythmic treatments have been investigated using computational modelling. For example, Trayanova et al. have reviewed the impact of current modelling studies on the understanding of resynchronisation therapies and drug treatments. The review is focused on the application of highly detailed biophysical models and suggests that these can augment clinical studies and elucidate novel treatment methods.[21] Furthermore, computation modelling is suggested as particularly useful for predicting ablation therapy targets[22]. Ablation therapy requires more information about electrophysiological substrate and wave dynamics that currently cannot be accurately measured in the clinic. Therefore, modelling can be used to bridge the gap between available measurements (such as patient MRI and electroanatomical mapping, as well as ex-vivo, data) and therapy[23].

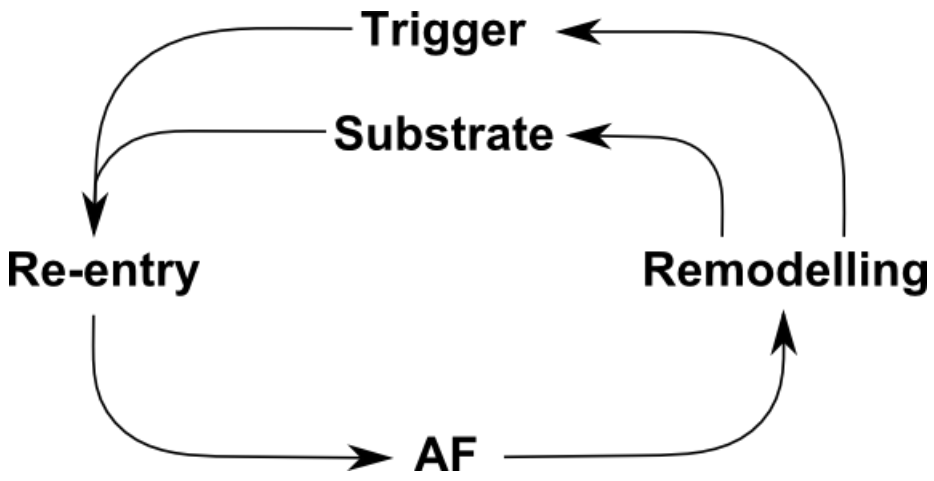


***Figure 6.*** *Flow diagram of the factors contributing to the genesis of AF. It shows the positive feedback loop that describes the notion "AF begets AF".*

### 2.3.2. Mechanisms of AF

High-frequency electrical activity in AF is believed to be sustained by multiple re-entrant circuits. For re-entry to occur a trigger and suitable substrate are required, both of which are facilitated by atrial remodelling. The extent of remodelling is increased during AF progression and completes a positive feedback loop (Figure 6) which explains both the progressive nature of the disorder and the notion "AF begets AF".[24]

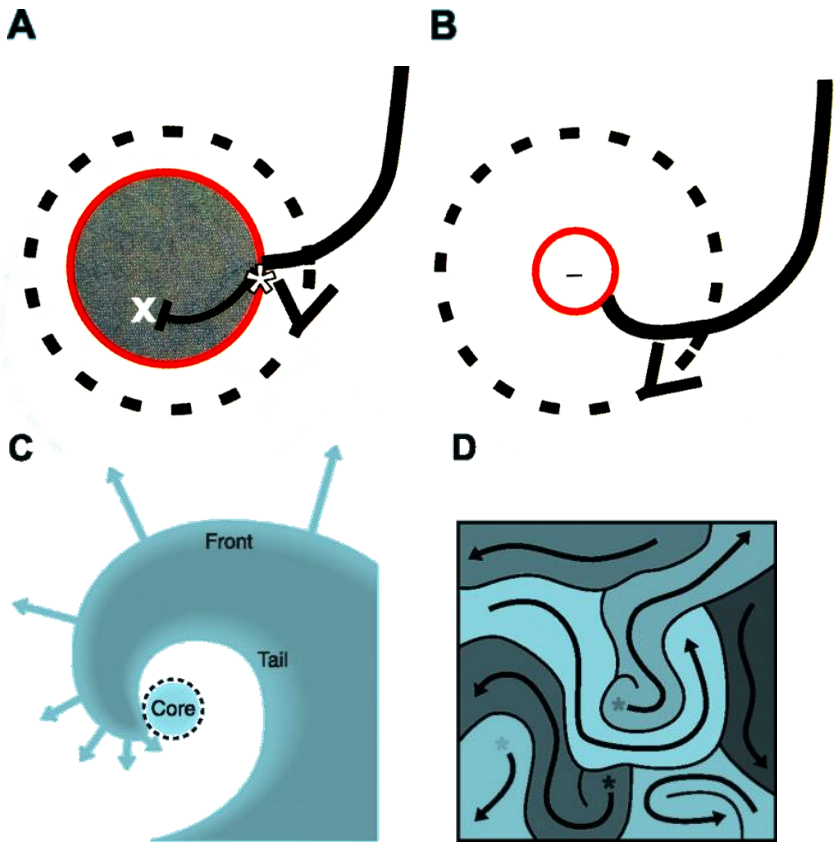


***Figure 7.*** *Current theories for re-entrant AF drivers. A: the leading circle theory, although the core is excitable, it is maintained in a refractory state by impingement of the wave tip. B and C: the rotor theory, where the broken wave forms a tip and rotates as a spiral waveform around and functionally non-excitable core (the arrows indicate conduction velocity). The wave is formed around a core of a minimum radius of rotor propagation. D: the multiple wavelet theory that chaotic small waves randomly activate the tissue. Images A and B from Zipes & Jalife*[25] *and C and D from Schotten et al.*[26]

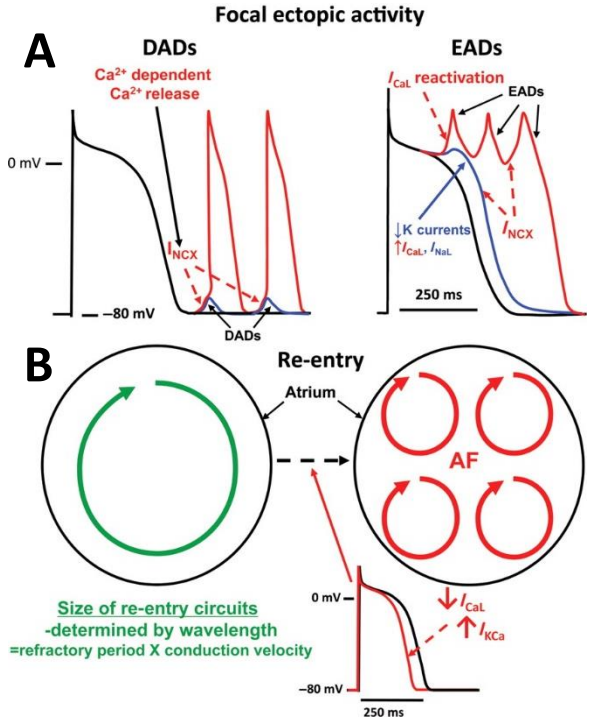


***Figure 8***. *Mechanisms for AF initiation and sustenance. See Figure 7 for the flowchart of AF genesis. A shows the mechanisms for ectopic triggers, in this case focussing on the potential role of calcium currents. B shows the determinants for the dynamics of re-entry arising from the triggers, particularly its dependence on the wavelength. Figure from Nattel & Dobrev.*[27]

When the wavelength is sufficiently short the tissue can provide substrate for the wave to re-enter (Figure 7). Due to the repolarised tissue ahead of the wave this cyclic propagation is not self-terminating. Re-entry can occur around an obstacle (Figure 7A) such as a pulmonary vein or around damaged non-excitable tissue. However this may not always be the case, a further theory predicts a functional rotor as the main mechanism for cyclic re-excitation during AF[28,29]. The theory states that the rotor has a tip arising from a wave break and rotates around this singular point. This has been shown to occur in multiple simulations and animal tissue experiments, but is still contested in patients due to limited clinical observation[30]. It may be the case that because rotors meander, i.e. the tip or core meanders throughout the tissue that it becomes hard to identify it as a single

source. Recently published data from panoramic electro-anatomical mapping of AF patients have provided the first direct evidence for the existence of rotors in a clinical setting.[31]

There is much debate concerning the specific dynamics of re-entry, particularly whether the atria can sustain multiple separate re-entrant circuits or if the stochastic behaviour of AF is caused by the after effects of a single mother rotor.[32] The former, first hypothesised by Moe et al.[33], suggests there is no single re-entrant source but rather, the wave breaks into multiple wavelets, propagating and colliding and breaking into further small waves (Figure 7D).

### 2.3.3. AF Triggers

When the wavelength is sufficiently short and structural or functional obstacles are present in the atria, fibrillatory re-entry cannot occur without an initial stimulus or trigger. Spontaneous ectopic activity in atrial or PV cells has been observed in-vivo[34] and can produce high frequency waves that propagate throughout the atria. The mechanisms for myocytes developing autonomic activation is not fully understood, and in-silico modelling and in-vitro cell experiments can only partially reproduce these effects. Re-entry can be triggered in patients and large animal models through rapid pacing, which mimics rapid spontaneous bursts of action potentials associated with ectopic triggers for AF. During high frequency pacing uni-directional block can occur, which can initiate re-entry[35]. EAD and DAD (Figure 8) have been suggested as mechanisms for this behaviour.

### 2.3.4. AF Substrate

Substrate for re-entry refers to various electrophysiological and structural properties of the atria that make re-entrant conduction and AF possible. The mechanisms for re-entry initiation are commonly due to wave slowing and subsequent wave break, with diverse underlying causes ranging from atrial geometry and structural obstacles, to ionic heterogeneity and non-uniform refractoriness. Re-entry sustenance is not only facilitated by slow conduction but also reduced refractoriness, as both factors contribute to a reduced wavelength. Such factors are enhanced by AF-induced remodelling. Remodelling can lead to altered densities of ionic channels and gap junctions, reduction of the action potential duration (APD), loss of cell-to-cell coupling, as well as fibrosis and increased atrial size due to dilatation or hypertrophy[36,37,38].

Moreover, due to the fibrous structure of the tissue and the predominantly end-to-end coupling of the cells, the propagation of the wave is biased along the fibre. If a wave travels transversally across these fibres, part of the wave can travel faster causing deformation, which could break the wave and create a rotor. In some regions of atrial tissue, sharp changes of fibre orientation occur (e.g. PV trunks,CT and pectinate muscle junctions). It has been suggested that high local anisotropy can cause autonomic activation to produce ectopic waves. [34] These areas may increase the likelihood of wave breakdown or blockage due to the longer refractoriness of lateral propagation across fibres.

A closely related effect occurs due to the intrinsic heterogeneity of the myocardium. Different atrial regions have different electrophysiological properties

and different APD/ERP. If the wave crosses perpendicularly to a border of two regions with different APDs, one could be excitable and the other still refractory, which can result in the breaking of the wavefront.[37,39]

The geometry of the atria provides another complex contributing factor for AF. The irregular atrial wall thickness has been suggested as a substrate for AF [40] due to the sink-source relationship. The theory states that due to the curvature or increase of thickness of atrial wall the current has to diffuse into a larger volume. Due to the current being divided between a much larger number of cells, they each have a lesser electrotonic current, which slows the conduction and facilitates wave breaks and re-entry. This effect can also occur as a result of high wavefront curvature.[41]

### 2.3. 5. Ionic Remodelling

The progressive and treatment-resistant nature of AF suggests a physiological positive feedback loop as mentioned in section 2.3.4. Functional and structural remodelling have been suggested as mechanisms for this and has a profound effect on arrhythmogenesis.

Ionic remodelling has been shown to promote AF[42]. By changing the electrical properties of the cells it reduces the APD/ERP and wavelength, increasing the risk of re-entry. The APD/ERP reductions are promoted by the underlying changes of ion channel currents. Specifically, the decreased plateau phase is mostly due to down-regulation of $Ca^{2+}$ currents and the acceleration of repolarisation due to up-regulation of $K^{+}$ currents.

The reason for this response is incompletely understood, but it may be compensatory and preventative; one example of this is the case of $Ca^{2+}$, overload where ionic remodelling prevents cell death[43]. During rapid electrical activations, myocytes risk calcium overload, which can become cytotoxic[43] and contribute to cardiac failure[24]. To counteract this, the cells remodel the L-type calcium channels to reduce the influx of calcium. Although this "last ditch" preventative reaction has the negative effect of reducing the ERP, which in turn perpetuates AF.

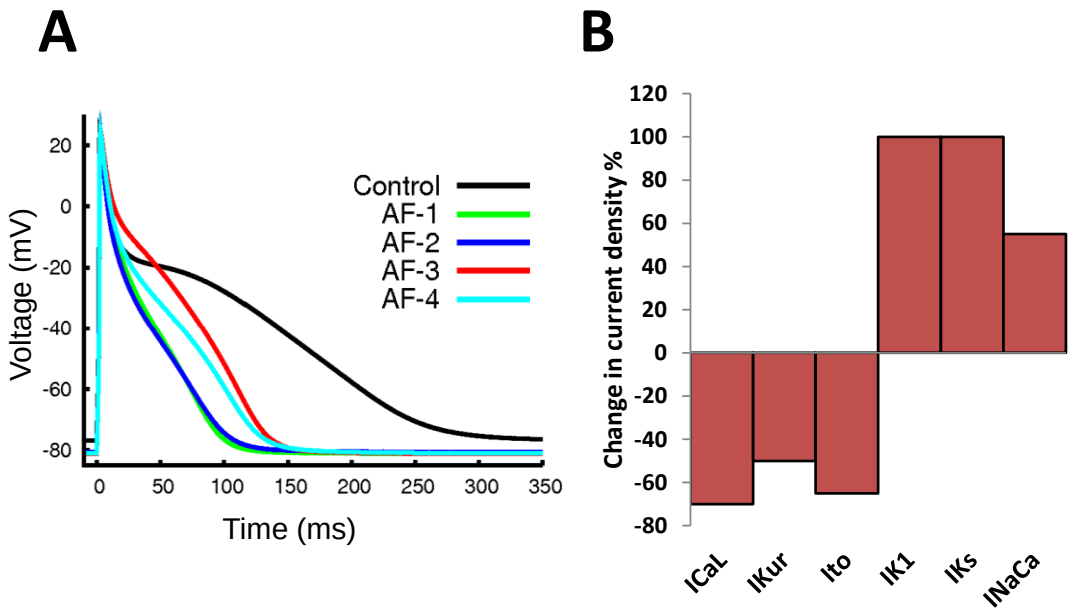


***Figure 9.*** *Cellular effects of AF-induced ionic remodelling. A shows changes of AP morphology due to remodelling during AF[39] (four different AF cases are shown). B shows the underlying changes in the ionic channel current densities for the case of AF-4. These are based on experimental data from literature.[42] Image A is reproduced from Colman et al.* [39]

The remodelling effects in the repolarisation phase are mediated predominantly by changes of $I_{K1}$ and $I_{KAch}$, with the latter current activated by the vagal nerve stimulation which releases acetylcholine (Figure 9). Increased acetylcholine release is known to stabilise AF[44]. Remodelling of some other currents, such as $I_{Kur}$, and its effects on AF are debated and reported experimental results are variable.[43,45]

### 2.3.6. Structural remodelling

Structural remodelling changes tissue morphology, and hence affects conduction pathways, and may affect re-entrant circuits. Cardiac hypertrophy or dilatation enlarges the atria, increasing the potential size of the circuit which promotes re-entry. This form of remodelling is often a response to hypertension. Structural remodelling can also affect the gap junctions, with altered levels of expression and localisation on the myocytes, although precise changes during such a re-localisation are debatable[43].

Structural remodelling can also be expressed as fibrosis which is a process that deposits collagenous matrix in response to mechanical stress on the atria, which in turn may be induced by a number of factors. Fibrosis is the formation of excessive extra-cellular matrix and collagenous tissue deposited by fibroblasts and can occur in all tissues in the body.

Fibrosis may be initiated by a number of factors such as cell damage, hypertension, paracrine stimulation and AF progression[46]. It is initiated by transforming growth factor beta (TGF-β)[46] which causes fibroblasts to proliferate and begin depositing collagenous matrix.

Fibroblasts account for up to 60% of the cellular population within cardiac tissues[47,48], and are reparatory cells, responsible for the deposition of extra cellular matrix. However due to the low regenerative ability of cardiac tissues, pathological fibrotic scarring can occur due to the high density of fibrous matrix. This can result in reduced functionality of the tissue and creates several compounding effects on the electrophysiological properties of the tissue.

Large areas of naturally occurring dense fibrosis can be referred to as ‘scar’ or compact fibrosis (Figure 10); this is functionally similar to fibrotic ‘scar’ induced as a result of ablation. To prevent confusion, in this work, scar will refer to fibrosis from ablation lesions and dense as disease related compact fibrosis. Dense fibrosis be imaged in AF patients using delayed gadolinium enhanced MRI (see Chapter 5). This type of fibrosis can block the conduction of waves, initiating re-entry, and may become sites of rotor anchorage [49].

Less severe regional collagen density, where strands of functional tissue are still present and conduction can still occur is known as patchy fibrosis (Figure 10). This morphology of fibrosis is inhomogeneous. The collagen deposits effectively slow conduction. From a macroscopic viewpoint the tissue is proportionally less excitable, with current from the fewer cells being diffused over a larger area. At a microscopic level, the wave has to travel in a more emphasised zig-zag pattern (Figure 11) due to the alignment of collagen deposits and the myofibres[50]. This latter case also suggests that higher anisotropy is associated with patchy fibrosis as the longitudinal propagation is relatively unhindered [51].

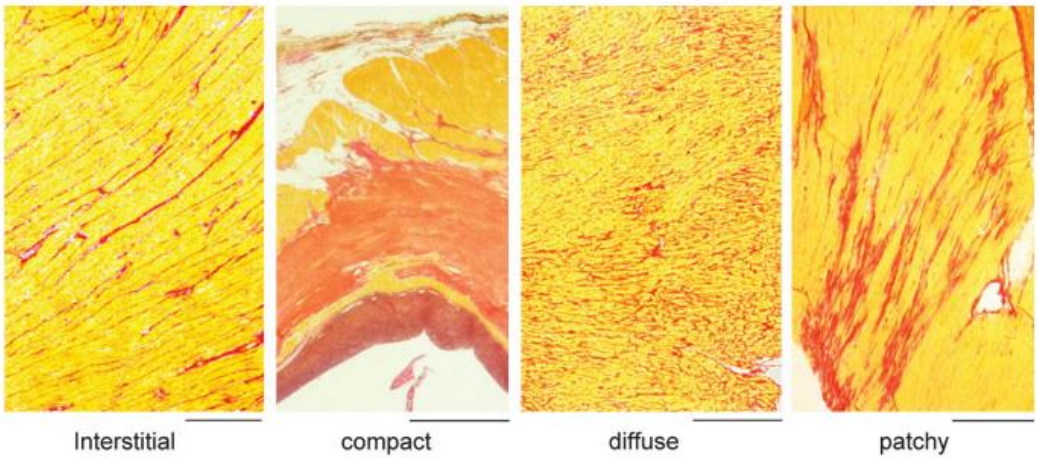


**Figure 10**. Types of fibrosis *(from left to right); interstitial fibrosis, which is present in normal healthy tissue as extracellular matrix. Compact fibrosis (often referred to as scar) consists of dense fibrosis devoid of myocardial cells. Diffuse fibrosis describes a uniform low level increase in fibrosis throughout the organ. Patch fibrosis, which describes larger, elongated collagenous bundles that run in parallel with the myocardial fibres.*[52] *Scale bars are 1mm.*

Diffuse fibrosis (Figure 10) describes the least severe type of fibrosis. It consists of small deposits of collagen spread evenly throughout an area. Diffuse fibrosis usually occurs throughout the whole tissue, and is indicative of a systematic disorder rather than a regional one. Diffuse fibrosis also reduces the conduction velocity but to a lesser extent than patchy fibrosis[53].

In addition to the structural effects of fibrosis, the fibroblast cells may also contribute to arrhythmogenesis. It has been shown that they have a paracrine influence on the myocardium[54] and may influence the structural[55] and electrophysiological properties.[47] Although they do not produce an AP they can conduct current through gap junctions with myocytes[56], and hence act as an electrotonic load on myocytes. They also possess active ion channels (Chapter 3)[57,58] and can generate a resting potential which is more positive than that of myocytes.[59]

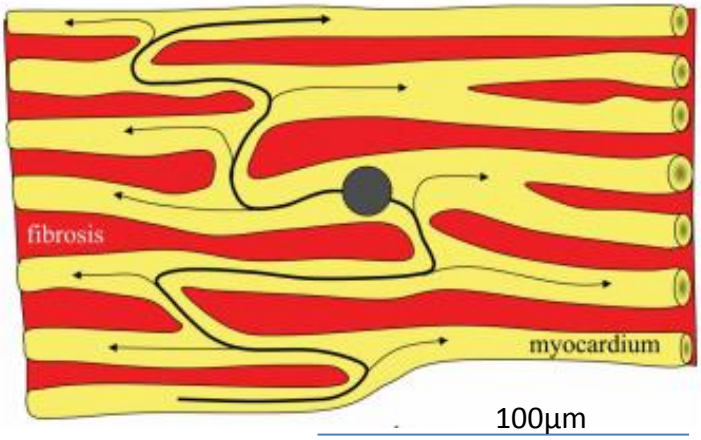


***Figure 11***. *Conduction slowing as a result of zig-zag propagation. Lateral conduction across the tissue sample is reduced due to the tortuousness of the conduction pathway.*[52]

The combination of gap junctional coupling and the resting potential difference between myocytes and fibroblasts creates a current between the two cell types. The coupled fibroblasts (one or more) produce a damping effect to the myocyte, reducing the AP upstroke and affecting the repolarisation and ERP. This could also reduce the conduction velocity due to the loss of current to the fibroblasts by reducing the current transferred to the next myocyte.

## 2.4. Mathematical modelling

Clinical investigation of AF is problematic, since direct measurements of atrial electrophysiology in patients is mostly limited to minimally invasive methods that have poor resolution or are confined to small areas of endocardium. Many studies[60] are focused toward the inverse problem, which uses body surface electrophysiological mapping to non-invasively to calculate the wave dynamics in the atria. However neither approach gives insights to the role of underlying structures or ionic properties of the tissue, and therefore currently have limited uses in determining the mechanisms of AF.

Animal testing has been useful in developing knowledge of AF as it allows for more invasive measurement of the disorder in combination with dissection of the tissue structure. The histology identified from this method has informed detailed cell models and provided physiological information that cannot be obtained from patients. However animal experiments also have limitations, predominantly the inherent differences between animals and human anatomy and physiology.[61] Therefore unequivocal conclusions about human electrophysiology may not be made. Moreover, animal studies can rarely achieve true integration of in-vitro cell and tissue data and in-vivo organ level experimental data.

Biophysically detailed modelling presents an opportunity to observe cell-to-organ electrophysiological dynamics with clinically relevant properties, ethically and with reduced expense. Due to the quantitative nature of computational modelling, it is possible to dissect individual parameters of the simulation that cause the largest changes to the arrhythmogenic wave dynamics in order to identify more significant factors for the development and sustenance of AF.

### 2.4.1. Cell electrophysiology modelling

The foundation of all electrophysiological modelling was laid by Hodgkin and Huxley earning them the Nobel Prize in Physiology or Medicine in 1963. Their model simulates the action potential in a giant squid axon. This was achieved by approximating each excitable cell as an electric circuit, a capacitance represents the cell membrane, time and voltage dependant conductances represent specific ionic currents and electrochemical gradients are represented by batteries.

In their model all specific ionic channel current kinetics are simulated with activation and inactivation variables, which represent the relative proportion of channels within a cell in either active or inactive states. From this relationship it is possible to calculate the ionic current of a particular ion across the cell membrane (equation 2).

$$I_{ion} = m^a h^b g_{max}(V_m - E_{ion}) \quad (2)$$

Where *m* and *h* are activation and inactivation gating variables, $g_{max}$ is the maximum conductance, $V_m$ is the membrane voltage, $E_{ion}$ is the Nernst equilibrium potential. The Nernst equilibrium potential is the point of equilibrium between the gradient of charge and the gradient of concentration so that transmembrane ionic flux is zero.

$$E_{ion} = \frac{RT}{zF} ln \frac{[ion]_e}{[ion]_i} \quad (3)$$

Where *R* is the universal gas constant, *T* is the absolute temperature (Kelvin), *F* is the Faraday constant, *z* is the valence number and $[ion]_{e/i}$ are extracellular and intracellular ionic concentrations. Using the Nernst equilibrium potential it is possible to calculate the driving force. This describes the difference between the membrane potential and the equilibrium potential, which then drives the ionic flux, $I_{ion}$ , through conducting channels, collectively characterised by the conductance $g_{max}$. In cases where currents are not ion-specific and are dependent on multiple ions, the ionic current (2) is considered as the linear sum of the currents carried by individual ions, with each current characterised by a relevant Nernst potential (3).

Hodgkin and Huxley used voltage clamping, an experimental method for characterising ionic channel currents in vitro, by incrementally increasing a constant voltage applied across the cell membrane. From these experiments they were able to formulate the time and voltage dependence of activation and inactivation gates. Considering $p_i$ as the probability that gates of type *i* are open (for example *m* or *h* in equation with a range of 0-1 and $p_i(t)$ is the fraction of gates open at time *t* then 1-$p_i(t)$ is the fraction that are closed. To transition between open and closed states two rate coefficients are required; $\alpha_i$ and $\beta_i$, both of which are voltage dependant.

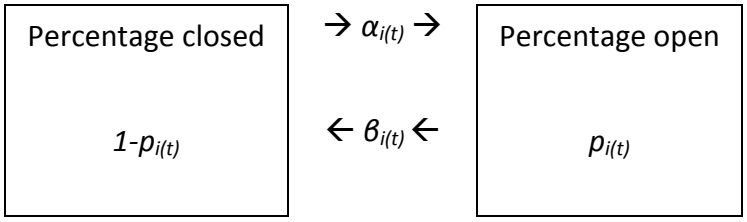


So therefore the change in probability of the state of the gates is

$$\frac{dp_i}{dt} = \alpha_i(V_m)(1 - p_i) - \beta_i(V_m)p_i \qquad (4)$$

If the voltage is fixed or clamped at value $V_m$, the gates will tend towards a steady state probability value $p\infty$:

$$p_\infty(V_m) = \frac{\alpha_i(V_m)}{\alpha_i(V_m)+\beta_i(V_m)} \qquad (5)$$

The time for this equilibrium to occur is denoted by a time constant $\tau_i(V_m)$

$$\tau_i(V_m) = \frac{1}{\alpha_i(V_m)+\beta_i(V_m)} \qquad (6)$$

Therefore, equation 4 can be written in the following alternative form:

$$\frac{dp_i}{dt} = \frac{p_\infty(V_m)-p_i}{\tau_i(V_m)} \qquad (7)$$

For example,

$$\frac{dm}{dt} = \frac{m_\infty(V_m) - m}{\tau_m(V_m)} \quad (8)$$

The total membrane current, $I_m$, is a sum of the capacitive and ionic currents and must be equal zero by Kirchhoff's law for the balance of currents:

$$C_m \frac{dV_m}{dt} = -\sum I_{ion} = -I_{tot} \quad (9)$$

Where; $C_m$ is the membrane capacitance, $I_{tot}$ is the total ionic current carried by various ions. This ordinary differential equation (ODE) can be solved with the simple Euler method with a time step of 0.005ms, which has been shown to work well for most existing ODE-based cardiac cell models[48], including the one used in this study (section 2.5).

### 2.4.2. Tissue modelling

While it is possible to model discrete tissue, where cells are individually modelled and coupled, it is computationally expensive and not viable for large-scale 3D simulations. Continuum models are used to approximate the simulated tissue domain in the 3D space. Two main types of continuum model are used; the monodomain model (equation 10) which assumes the intra and extracellular conductivities are the same and the bidomain model which does not. Although the bidomain is arguably a better approximation of reality, in larger-scale simulations it has been shown to yield little difference in results[62] although useful if simulating external stimuli[63]. The monodomain equation can be written as:

$$\frac{\partial V_m}{\partial t} = \nabla \cdot (\boldsymbol{D} \nabla V_m) - \frac{I_{tot}}{C_m} \quad (10)$$

where ∇ is the 3D gradient operator and ***D*** is the diffusion coefficient, which can be a tensor if the tissue is anisotropic.

### 2.4.3. Numerical solvers

The continuous equations, such as equation 10, require discretisation in order to be solved using an iterative numerical procedure in simulations. This is because analytical solutions are not generally possible for nonlinear partial differential equations (PDEs). There are various numerical methods such as finite element and finite volume, which provide approximate solutions for these PDEs and have been applied specifically to electrophysiological modelling. In this section we will only consider the method used in this thesis.

The finite difference method (see equation 12) is the most common method of calculating spatially discretised voltages in 3D tissue described by the monodomain equation. The method divides the simulation space into a regular grid with a spacing $\Delta x$. Although $\Delta x$ can generally vary throughout the geometry, in this work it will be constant.

The numerical solver used is the forward Euler method. It provides a simple numerical algorithm for differential equation integration by assuming that the change in $y$ is constant for a small change in $t$. A generalised method is shown (equation 12) for the ordinary differential equation (equation 11). The space step used was 0.33mm as this was compatible with the established geometric datasets used in this work (Chapter 4 ).

$$\frac{\partial y}{\partial t} = f(y, t) \tag{11}$$

$$y_{t+dt} = y_t + dt \times f(y_t, t) \quad (12)$$

When applied to the monodomain equation (expression shown here describes a 1D case) voltage can be calculated (at a time *t=t+Δt*):

$$V_{t+\Delta t} = V_t + \frac{D\Delta t}{\Delta x^2}\left(V_{x+\Delta x,t} + V_{x-\Delta x,t} - 2V_{x,t}\right) - \frac{\Delta t I_{ion}}{C_m} \quad (13)$$

Using this simple solver is less computationally expensive that other methods but can be prone to instability. For a stable simulation the criterion (equation 14) must be maintained. This is shown a constant diffusion coefficient in *N*-dimensional space, which can be also applied as a sensible practical estimate for non-linear problems (where a general criterion does not exist):

$$\Delta t \leq \frac{\Delta x^2}{2^N D} \quad (14)$$

## 2.5. Cardiac electrophysiology modelling

Most electrophysiological cell models are based on the Hodgkin-Huxley formulation, and have been modified to represent cardiac electrophysiology[64,65]. These models simulate a diverse range of pathophysiologies relevant to AF, e.g. chronic heart failure remodelling, or drug therapies. This section outlines the various cardiac models used in this work and details their properties.

### 2.5.1. Courtemanche-Ramirez-Nattel atrial myocyte model

Although other cardiac myocyte models exist (Fenton-Karma,[66] Grandi et al.[67]), the Courtemanche-Ramirez-Nattel (CRN) was used in this work, as it provides high biophysical detail and has been extensively studied. The CRN model[64] developed in 1998 is one of the earliest atrial myocyte models. It was developed to provide a useful model of the atrial AP based upon their specific formulations of $K^+$, $Na^+$ and

$Ca^{2+}$ currents. The schematic in Figure 12 shows the relevant ionic channels and the sarcolemic calcium channels. AP morphologies simulated using the CRN model are illustrated in Figure 10. Properties of this model have been extensively studied.[48]

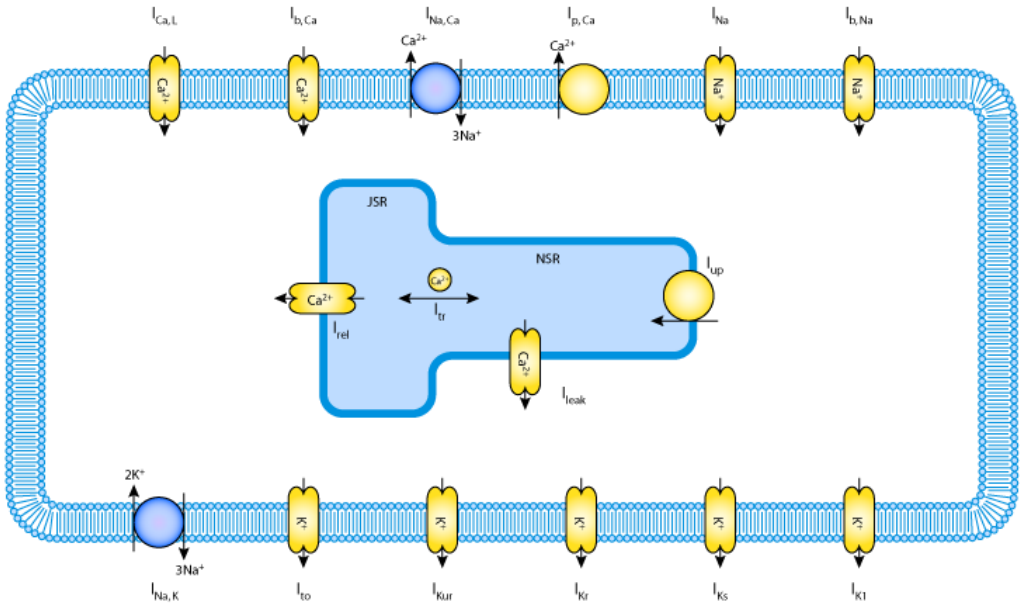


***Figure 12.*** *Schematic of Courtemanche- Rameirez-Nattel model. The cell membrane, in light blue is representative of the phospho-lipid bilayer that maintains the capacitance of the cell. The yellow shapes along this membrane indicate the various currents present in this model. In the centre of the figure is a further membrane that isolates the sarcoplasmic reticulum (JSR and NSR) from the cytoplasm. Figure from CellML model repository.*

### 2.5.2. Modelling arrhythmogenic properties

During AF multiple physiological properties change due to remodelling or have inherent parametric variation. There have been many previous studies[38,42,68] that used existing models such as the CRN model and modified parameters (e.g., ion channel conductances) to simulate such pathophysiological conditions. Due to the wide range of the conditions associated with AF, there is an equal numerous models investigating these conditions. In this study we utilised such modifications

of the CRN model for ionic remodelling, regional heterogeneity and myocyte-fibroblast coupling.

Within the atria there are natural electrophysiological variations between different tissues. These variations can culminate in gradients of AP variation that have been linked to arrhythmogenesis. Colman et al.[69] created a comprehensive model of all the regional APs achieved by altering conductances of different channels to matching the model to experimental data. Figure 13 shows the resultant AP variations. This study applies this family of region-specific atrial cell models both in 1D and 3D.

Ionic remodelling (as discussed in section 2.3.5) was also investigated. The respective model, also developed by Colman et al.,[42] modifies ionic current densities based on experimental data (similarly to how this was done to introduce the regional heterogeneity), in order to simulate the effects of ionic remodelling in AF. The effects on ionic currents and AP can be seen in Figure 9.

A further modification to the standard CRN model was the inclusion of myocyte-fibroblast (M-F) coupling. A novel single fibroblast cell model was developed (Chapter 3) with ionic currents based on the CRN formulation. Another, existing ventricular fibroblast model was utilised for comparison. The details of these models are explained in the following chapter.

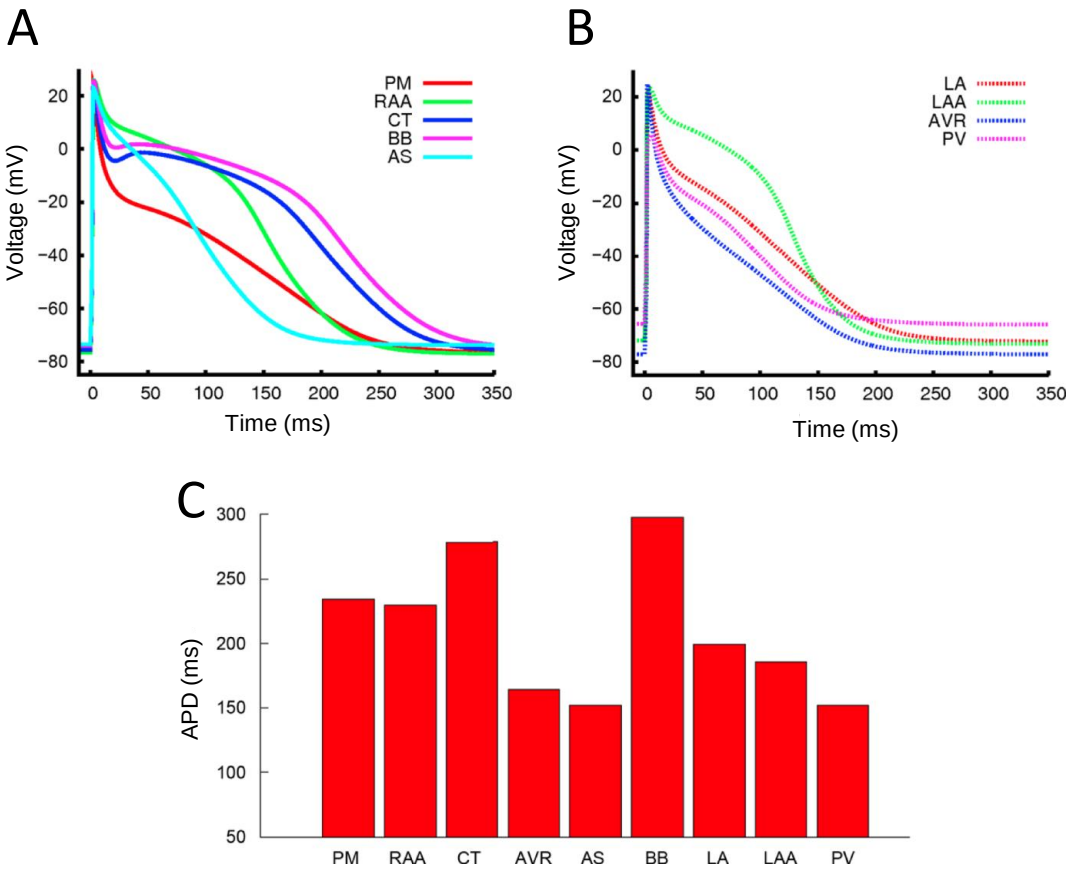


***Figure 13***. *Regional heterogeneity of the Colman et al. atrial myocyte model. A, shows the simulated APs of the regions in the right atrium; PM, RAA, CT, BB and AS. B shows the simulated APs of the regions located within the LA, LAA, AVR, PV. C is a bar chart of the APDs of the regions throughout both atria. Graphs sourced from Colman et al.*[38]

## 2.6. Magnetic resonance imaging

Various aspects of this study are reliant on structural data obtained from patients and healthy volunteers using magnetic resonance imaging (MRI). The method uses magnetic field to measure proton spin changes in water molecules. Different tissues of the body have different quantities of water in their structure and provide resonance contrast. A novel black-blood phase-sensitive inversion recovery sequence (PSIR) was used to maximise the contrast between the atrial wall, blood and lung[70]. This allowed us to investigate variance in the atrial wall (Chapter 6) and had an isotropic resolution of 1.4mm. Late gadolinium (Gd) enhanced (LGE) MRI

images were used to investigate fibrosis distributions in patients (Chapter 5). These images had a higher resolution of 2.5x2.5x4mm. This method uses an intravenous contrast agent, Gd, that perfuses into the myocardium[71]. Regions of high fibrosis have higher residual gadolinium content and higher image intensity.

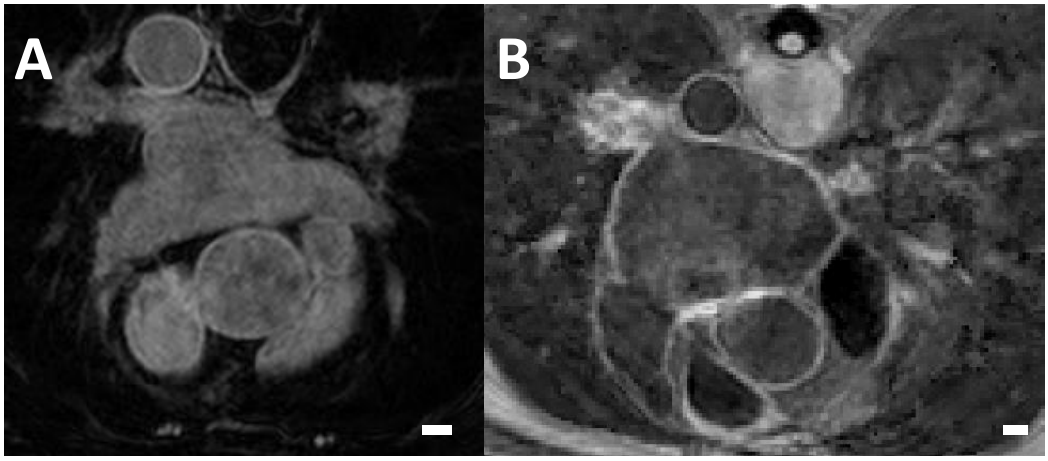


***Figure 14****. Cardiac MRI examples. A shows a LGE MRI of a patient with permanent AF. B shows a PSIR MRI image of a persistent AF patient. White scale bars are 10mm.*

## 2.7. Conclusion

Due to the progressive treatment resistant nature of AF it is clear that better understanding is required to improve treatments. Furthermore, detailed measurement of in-vivo electrophysiology and atrial structure is currently unavailable. Computational modelling provides the perfect link for developing understanding of this condition.

# 3. Myocyte-fibroblast coupling model

## 3.1. Introduction

Fibrosis is a multifactorial degenerative condition that is commonly associated with AF progression. Different pathophysiological mechanisms have been suggested as links between atrial fibrosis and AF. One of the primary links involves the intracellular deposition of collagenous matrix by cardiac fibroblasts. these cells are present in most tissues in the body and makes up 60-70% of the cardiac cell population[72]. Although fibroblasts are more abundant than the cardiac myocyte, they are much smaller than myocytes, at around 10-15µm compared to 100µm length of the myocyte. Thus, fibroblasts provide a smaller contribution to the atrial tissue volume. Fibrosis can affect atrial tissue structure through excessive collagen depositions and by electrophysiological function through electrotonic coupling between fibroblasts and myocytes.

### 3.1.1. Cardiac fibroblasts

In a healthy heart, fibroblasts are responsible for maintaining the structure of the tissue against stress and damage. They act dynamically, modifying and remodelling the atrial structure driven by changes in the mechanical requirements of the organ. This action is modulated by paracrine signals which can increase the localised populations, proliferation and/or activity of fibroblasts.[73] The causes for fibrosis initiation are unclear, but may be due to hypertensive stress response (i.e. mechanical stretch), localised ischemia or neuro-hormonal activity.

Under these pathological conditions, which may be caused by heart failure or localised tissue damage, dormant fibroblasts can differentiate into the phenotype known as myofibroblasts[74]. In this activated form fibroblasts proliferate, migrate, activate an inflammatory response and produce more collagen, creating a higher level of matrix deposition[75]. The phenotypical differences between the myofibroblasts and the fibroblast are underlain by various gene expressions of the cell in its active form[76]. Atrial tissue is more susceptible to fibrosis than ventricular tissue,[77] [78] which may be due to TGF-β being higher in atrial than ventricle fibroblasts [79] or that atrial fibroblasts have a higher propensity to differentiate into the more active myofibroblast [78]. A note must be made that for the rest of this report the term myofibroblast will be generalised and referred to as fibroblasts.

### 3.1.2. Fibroblast electrophysiology

Unlike myocytes, fibroblasts are not electrically excitable, however they can maintain a resting membrane potential (RMP), and hence affect and be affected by the tissue electrophysiology. Myocyte-fibroblast electrotonic coupling has been observed in-vivo and in vitro, current exchange between fibroblasts and myocytes was first confirmed in frogs[80] and later in rats[81] . The M-F coupling mechanism uses gap junctions, in the same manner as inter-myocyte coupling. These gap junctions are comprised of proteins connexin-43 and 45 (Cx43, Cx45), which have been observed in co-cultured neonatal rat fibroblasts and myocytes.[81,82] This was followed with in-vivo observation of Cx45 expressed by fibroblasts in rabbit SAN.[83] Tunnelling nanotubes or membrane nanotubes have been investigated as another gateway permitting M-F interaction. These pathways can directly link the

cytoplasms of myocytes and fibroblasts[84] allowing for ionic transfer, in particular the active transport of calcium ions.[84]

| | **Fibroblast RMP** | **Currents** | **Cell type** | **Cell source** |
|---|---|---|---|---|
| Wu et al.[85] | -42.8mV (LA)<br>-44.9mV (LV) | $I_{Kur}$<br>$I_{to}$ | Human atria and ventricle | freshly isolated |
| Li et al [57] | - | $I_{BkCa}$, $I_{to}$, $I_{K1}$, $I_{Cl}$** | Human ventricle | cultured |
| Shibukawa et al.[86] | -58 ±3.9mV | $I_{ns}$, $I_{Kv}$ | Adult rat ventricle | |
| Chilton et al.[59] | - | $I_{K1}$,$I_{Kv}$ | Rat ventricle | isolated |
| Kiseleva et al.[87] | -22mV | - | Rat atria | isolated |
| Rook et al. [81] | -20 ÷ -30mV | - | Neonatal rat | cultured |
| Kamkin et al.[88] | -37±3 mV | $I_{ns}$ * | Rat atria | |
| Wang et al.[89] | - | $I_{ns}$ †, $I_{BkCa}$ ‡ | Rat ventricle | cultured |
| Miragoli et al.[90] | -14 ÷ -25mV | $I_{K1}$ | Neonatal rat ventricle | cultured |
| Kohl et al.[80] | -15mV | - | Rat atria and SAN | isolated and cultured |
| Kohl et al.[80] | - | $I_{Cl}$, $I_{Kv}$, $I_{K1}$, $I_{Na}$ | Frog SAN | |

***Table 2***. *Electrophysiological properties of cardiac fibroblasts. The table identifies ionic channel currents and RMP of fibroblasts as researched in literature. *(gadolinium sensitive),†(mechanosensitive), ‡ big conductance $Ca^{2+}$, **(volume sensitive) -activated K+ current has been reported in some studies of cultured cells.*

The electrophysiological function of fibroblasts is determined by the presence of a range of ionic channel currents in their cell membrane. It is known that both

cultured and freshly isolated fibroblasts express voltage dependant potassium channels ($I_{Kv}$)[59,74,85,90,80]. A wide variety of currents have now been discovered in the cardiac fibroblast, predominantly potassium ($I_{Kur}$, $I_{Kir}$, $I_{to}$), but also non-specific ionic currents ($I_{ns}$) which can be mechanically and non-mechanically activated and chlorine ($I_{Cl}$). The sources of data for these various currents are diverse, and are summarised in Table 2.

Some of this data should be treated cautiously, due to the differences in cellular physiology between cultured and intact cells[74,91]. A further consideration is the variation between atrial and ventricular electrophysiology, which is also observed in fibroblasts[85,91] as well as myocytes[38]. The differences in fibroblast electrophysiology have been suggested as potential drivers for the variation in fibroblast population between the atria and the ventricles, which is higher in the atria[92]. Due to these observed differences, ventricular models may not be suitable for investigating atrial electrophysiology. The most comprehensive study of atrial fibroblast electrophysiology has been published recently by Wu et al.,[85] who explored the variations between atrial and ventricular fibroblasts in freshly isolated cells.

The presence of ionic channel currents in fibroblasts leads to the generation of RMP in the fibroblast. Direct measurement of the RMP in fibroblasts shows more positive values (from -58 mV in the ventricles and up to -15 mV in the atria, shown in Table 2) than RMP in myocytes (about -80mV). Other electrophysiological effects of M-F coupling on the myocyte have been found. Miragoli et al. found in co-cultured myocytes and fibroblasts that, as the relative concentration of fibroblasts

increased, conduction velocity and maximum upstroke were reduced. This may be due to the higher RMP of the fibroblast depolarising the myocytes.[90]

### 3.1.3. Modelling of fibroblast electrophysiology

There has been previous research using computational modelling to investigate the effects of M-F coupling and the subsequent electrophysiological effects of fibrosis. In-silico research is beneficial due to the difficulty of in-vivo measurement of cellular electrophysiology. These have ranged from simple passive models[93], with only a resistive gap junction connection and no fibroblast ionic channels, to complex models with time and voltage dependant ionic currents[58,94,95].

The state of the art fibroblast model is the MacCannell et al.[58] model and its derivatives. These are based of the electrophysiological findings on Shibukawa et al.[86] which identify $I_{K1}$ and $I_{Kv}$ in ventricular fibroblasts. $I_{Kv}$ is an amalgamated time and voltage dependant potassium current. The subsequent variations of this model vary parameters in order to identify different behaviours of M-F coupling, such as RMP influences[92] of different coupling strengths and propagation[95]. Sachse et al.,[94] built a competitive model based on the same results and Chilton et al.[59] investigated the effects of M-F coupling on conduction. Zlochiver et al.[96] utilised a cell culture and a fluoroscopic dye to initiate re-entry to validate their model. A passive (with no fibroblast ionic currents; simply a membrane resistance and resting potential) computational model was used to quantify the conduction. They found that the M-F coupling had complex effects on conduction velocity, re-entry stability and wave complexity.

A further passive model was developed by Maleckar et al.[93] in for comparison with the MacCannell et al. model. The findings of the latter last study demonstrated that M-F coupling to an active fibroblast model created complex behaviour and changes to the AP which must be considered when investigating AF.

| **Model** | **RMP (mV)** | **Currents** | **$G_{gap}$ (nS)** | **# coupled fibroblasts** | **Animal** | **Cell type** |
|---|---|---|---|---|---|---|
| MacCannell et al.[58] | -47.8 | $I_{Kv}$, $I_{K1}$, $I_{NaK}$, $I_{bNa}$ | 1-3 | 1-4 | Human | Ventricle |
| Maleckar et al.[93] | -47.8<br>-31.4 | See above | 0.5-8 | 1-3 | Human | Atria |
| Jacquemet et al.[92] | - | - | 0.2-138 | 2-8 | Canine | Ventricle |
| Jacquemet et al.[95] | - | - | 138 | 30 | Canine | Ventricle |
| Sachse et al.[94] | -58 | $I_{kir*}$, $I_{Kv*}$, $I_b$ | - | 1-10 | Rat | Ventricle |
| Zlochiver et al.[96] | -15.9 | - | - | 1 | Neonatal rat | Ventricle |
| Kohl et al.[80] | -20mV | - | 0.01-0.03 | 1 | Rat | SAN |

***Table 3***. *Summary of previous computational studies of cardiac fibroblasts. Showing the RMP, the modelled ionic currents of the fibroblast, the gap junction conductance (Ggap), the number of fibroblasts and the animal cell type.*

Due to the difficulty of obtaining human electrophysiological data, the sources of data for these models are varied. Most come from animal[94,95] and/or ventricular studies[58], neither of which are not ideal for the investigation for atrial fibrosis and its role in AF genesis. Therefore, there is a strong need to utilise more recent

electrophysiology data in order to develop a more complex and representative electrophysiological model of the atrial fibroblast.

The aim of this work is to build a specific atrial fibroblast model based on the most comprehensive electrophysiological data. The remainder of this chapter described the creation of this model and the results obtained using it.

## 3.2. Methods

The framework for modelling the atrial fibroblast electrophysiology is based on a ventricular fibroblast model by MacCannell et al.[58] which is also used as a benchmark in this chapter. However, several novel ionic channel currents were added to this framework, which were based on the CRN formulation of the currents for human atrial myocytes and experimental data from atrial fibroblasts.

Data for the atrial fibroblast model was obtained from a study on fibroblast ionic currents in freshly isolated human atrial fibroblasts by Wu et al.[85]. By analysing the figures using the data extraction software Scanit$^{(R)}$, the relevant current-voltage (I-V) relationship data was extracted and then superimposed onto the respective simulated curves in Matlab$^{(R)}$. An optimal fit between the modelled ionic currents and experimental data was achieved by varying the current conductances. The results of this can be observed in Figure 15.

### 3.2.1. Modelling ionic currents

The model is based on the CRN formulation of the ionic channel currents in a human atrial myocyte and incorporates experimental data for the ionic currents recorded by Wu et al. from atrial fibroblast.[85] Three currents are measured by Wu et al. and are described as end-pulse current, 4-aminopyridine (4-AP) sensitive

current and S9941 sensitive current. In the same study the RMP of the isolated atrial fibroblasts was also measured and used to validate the model.

The 4-AP sensitive current was modelled as $I_{to,f}$, for which 4-AP is a selective blocker. Fitting this current to experimental data by Wu et al. involved a 90% reduction in the current conductance compared to the CRN model (Figure 15A), but no changes to the current kinetics was introduced.

The S9941 sensitive current was modelled as $I_{Kur,f}$, as S9941 is a blocker of ionic channels containing the subunit Kv1.5, which forms the channel conducting this current. Fitting this current to experimental data by Wu et al. involved a 40% reduction in the current conductance compared to the CRN model (Figure 15B).

The end pulse current was measured by Wu et al. as the total voltage sensitive current. We considered the remainder of this current after subtracting both $I_{to,f}$ and $I_{Kur,f}$ as a sum of a further two currents: a linear non-specific ionic channel current, $I_{ns,f}$, and the inward-rectifier potassium channel current, $I_{K1,f}$ (shown in Figure 15C). Both $I_{Kur,f}$ and $I_{ns,f}$ are major contributors to the fibroblast RMP. The separation of these two currents ensured that $I_{K1,f}$ reverses at the equilibrium Nernst potential for potassium, which is observed in electrophysiological recordings of this current in multiple cell types. The voltage and time dependences for these four currents are described by the following equations, based on the CRN formulation (note that index $_f$ denotes their relevance to fibroblasts):

$$I_{K1,f} = \frac{0.03(V_f+86.75)}{(1+exp(0.05(V_f+20)))} \quad (15)$$

$$I_{ns,f} = 0.018\, V_f \quad (16)$$

$$I_{to,f} = g_{to,f} * {o_{a,f}}^3 * o_{i,f} * \left(V_f - E_{K,f}\right); \quad (17)$$

$$I_{Kur,f} = g_{Kur,f} * {u_{a,f}}^3 * u_{i,f} * \left(V_f - E_{K,f}\right); \quad (18)$$

Here, $V_f$ is the membrane voltage of fibroblasts, where $o_{a,f,}$ $u_{a,f}$ and $o_{i,f,}$ $u_{i,f}$ are activation and inactivation gates respectively and $g_{Kur}$ and $g_{to}$ are conductances of the respective channels.

Other currents in the developed model are based on the MacCannell et al. formulation, specifically those not measured by Wu et al.[85] but assumed present in the fibroblast were based on experimental studies with other cardiac cells types. These are the sodium potassium exchanger ($I_{NaK}$) and the background sodium current ($I_{bNa}$). The entire fibroblast model is included in the appendix.

In the MacCannell et al. model and its derivatives, $I_{K1}$ and the time and voltage dependant current $I_{Kv}$ is simulated. This current was shown to be sensitive to 4-AP and S9941 in their experimental work[86] but modelled as a single current. It is based on the human atrial current $I_{Kur}$ and is given by the expression bellow:

$$I_{Kv} = g_{Kv} * r_{Kv} * s_{Kv} * \left(V_f - E_{K,f}\right); \quad (19)$$

where $r_{Kv}$ and $s_{Kv}$ are the activation and inactivation parameters respectively.

### 3.2.2. M-F coupling model

In order to simulate the coupling of fibroblasts to a myocyte we used a similar model to that developed by MacCannell et al. The myocyte model (detailed in Chapter 2) was the CRN atrial myocyte model. The fibroblast with a total membrane current $I_{tot,f}$ was coupled via the M-F gap junctional conductance ($G_{gap}$) to the

myocyte with the total membrane current $I_{tot}$. The equations for the M-F coupling model are as follows:

$$I_{tot,f} = \sum I_{ion,f} = I_{to,f} + I_{K1,f} + I_{Kur,f} + I_{ns,f} + I_{bNa,f} + I_{NaK,f} \quad (20)$$

$$\frac{dV_f}{dt} = -\frac{1}{C_{mf}}\left[I_{tot,f}(V_f, t) + G_{gap}(V_f - V_m)\right] \quad (21)$$

$$\frac{dV_m}{dt} = -\frac{1}{C_m}\left[I_{tot}(V_m, t) + \sum_{i=1}^{n} G_{gap}(V_m - V_f)\right] \quad (22)$$

Here subscripts *m* and *f* relate to a single myocyte and fibroblast and *n* to the number of fibroblasts coupled to one myocyte. $G_{gap}$ was set as 0.5nS[92] and *n* was varied between 0-6. Unless specified otherwise, a myocyte was coupled to 2 fibroblasts.

We also investigated how the M-F coupling model interacted with other physiological conditions associated with AF. These were ionic remodelling and regional heterogeneity (see Chapter 2)[38,42]. These parameters (specifically, ionic channel conductances changes due to the heterogeneity and remodelling) were additionally integrated into the CRN myocyte model.

### 3.2.3. Restitution measurement

All simulations and analyses of the dynamic effects of the single cell models were performed in Matlab(R) due to the advantage of easy visualisation. $APD_{90}$, ERP and excitation threshold, as well as their restitutions, were measured to characterise the electrophysiological properties of the models. These were all measured after a period of 40 beats in order to stabilise all variables in the model and reduce

alternans (periodic fluctuations in APD), which can be present in the CRN model at high frequencies. $APD_{90}$ was calculated by finding the period of time between the maximum upstroke and the AP repolarisation to 90% of the difference between the peak amplitude (APA) and the minimum membrane. The advantage of $APD_{90}$ (as opposed to $APD_{60}$) is that it encompasses phase 4 of the AP, in which M-F coupling has a greater effect. Excitation threshold was measured by incrementally varying the stimulus current in single cell until an AP was formed. This procedure was pre-paced at a range of frequencies allowing for a restitution curve to be plotted.

The tissue ERP was calculated in a quasi-1D tissue by applying a stimulating current at one end to initiate AP propagation to the other end. This was modelled as a long 3D slab of 50 x 7 x 7 cells with a space step of 0.3mm and a diffusion coefficient of $0.3mm^2ms^{-1}$. The stimulus of -2500 mA was applied in the first 10 layers of cells. This resulted in a 1D plane wave propagating along the slab. Zero-flux boundary conditions were implemented at all sides of the slab. Stimuli were applied at a given BCL, followed by a last stimulus applied at a variable S2 interval. The latter was increased until an AP was observed at the non-stimulated end of the cable. The minimum S2 interval for which AP was still able to propagate through the cable was taken as ERP. This simulation also allowed the calculation of the conduction velocity by calculate transmission times across the tissue. Both ERP and CV were measured at different BCL to produce the full restitution curves (see Results).

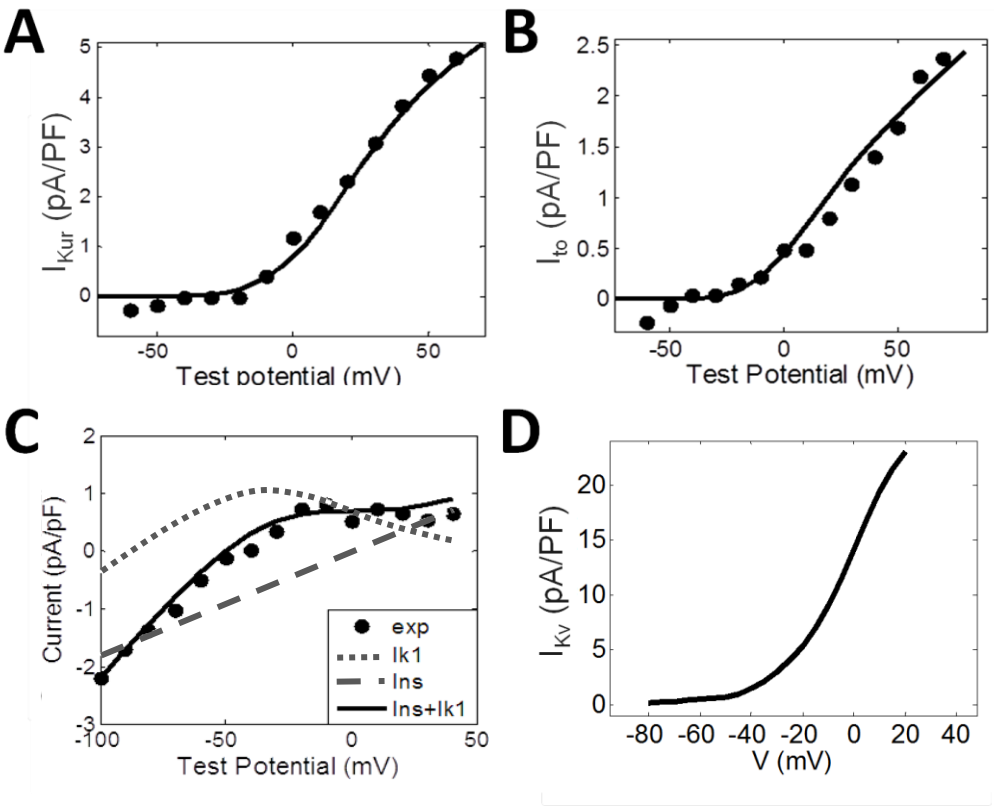


***Figure 15***. *Ionic channel currents of the atrial fibroblast model. A-C: The simulated current voltage (I-V) curves for the major ionic currents (solid lines) are shown along with the respective experimental data (dots). A. The ultra-rapid current, $I_{Kur}$. B. The transient outward current, $I_{to}$. C. The experimentally measured end-pulse current (black dots), with the simulated inward-rectifier and non-specific currents, $I_{K1}$ and $I_{ns}$, (grey lines) and the combined current $I_{K1} + I_{ns}$ (black line). D: $I_{Kv}$ simulated by the ventricular fibroblast model by MacCannell et al.; it represent the sum of $I_{Kur}$ and Ito. Note that the index 'f' used in equations (1)-(4) above is omitted here for simplicity.*

### 3.3. Results

In this section 3 main conditions are modelled and investigated. The CRN myocyte without M-F coupling (i) the atrial myocyte coupled to the novel atrial fibroblast model (ii) and the CRN atrial myocyte coupled to a ventricular fibroblast model (iii) as developed by MacCannell et al.

### 3.3.1 Single atrial fibroblast model

The fitting of ionic channel currents in the atrial fibroblast models to the respective patch clamp data can be seen in Figure 15A-C. I-V curves for both $I_{Kur}$ and $I_{to}$ in the model are in good agreement with the experimental data.

Figure 15C illustrates fitting of the combination of $I_{ns}$ and $I_{K1}$ in the model to the experimentally measured remainder end-pulse current, again with good agreement across the physiological voltage range. Figure 16 compares the current densities in the developed atrial fibroblast model, the CRN atrial myocyte model used to derive these currents, and the MacCannell et al. model for ventricular fibroblast.

After fitting the ionic currents to experimental data, the RMP in the resulting model for a single atrial fibroblast was -42.5mV, which was in close agreement with the respective experimental value of -42.8mV ±1.3 mV recorded from atrial fibroblasts[85]. This value is more positive than the RMP of -48 mV in MacCannell et al. ventricular fibroblast model. Note that both -42.5mV in the developed atrial fibroblast model and -48mV in the ventricular fibroblast model are within the experimental data range (Table 2), but -42.5mV closer corresponds to RMP in human atrial fibroblasts.

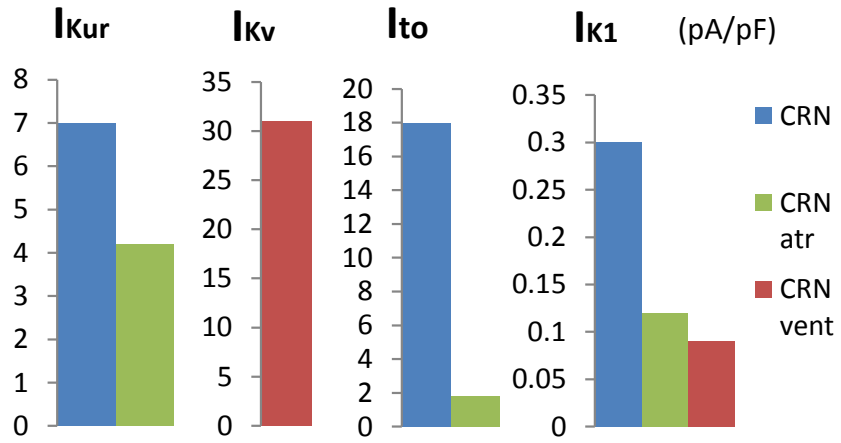


***Figure 16*** *Ionic current density in the single cell models. Different currents are compared between the uncoupled myocyte (blue), the atrial M-F model (green) and the MacCannell et al. (red) M-F model. All current densities are measured in pA/pF.*

### 3.3.2 Myocyte-fibroblast coupling model

Coupling to fibroblasts significantly affected electrophysiological properties of the myocyte. Figure 17A and B, illustrates APs in the control CRN model (i) ,coupled to the developed atrial fibroblast model (ii), and the CRN model for a myocyte coupled to the MacCannell et al. ventricular fibroblast model(iii). In these simulations, a myocyte was coupled to 2 fibroblasts. The M-F model (ii) produced prolonged repolarisation compared to the uncoupled control model (i), whereas the M-F ventricular model (iii) produces a more rapid repolarisation than in control. Hence, coupling to atrial (ii) and ventricular (iii) fibroblasts produces opposite effects on AP in the CRN atrial myocyte model (i). Figure 17C and D shows the respective membrane potential in atrial and ventricular fibroblasts for the M-F coupling models (ii) and (iii).

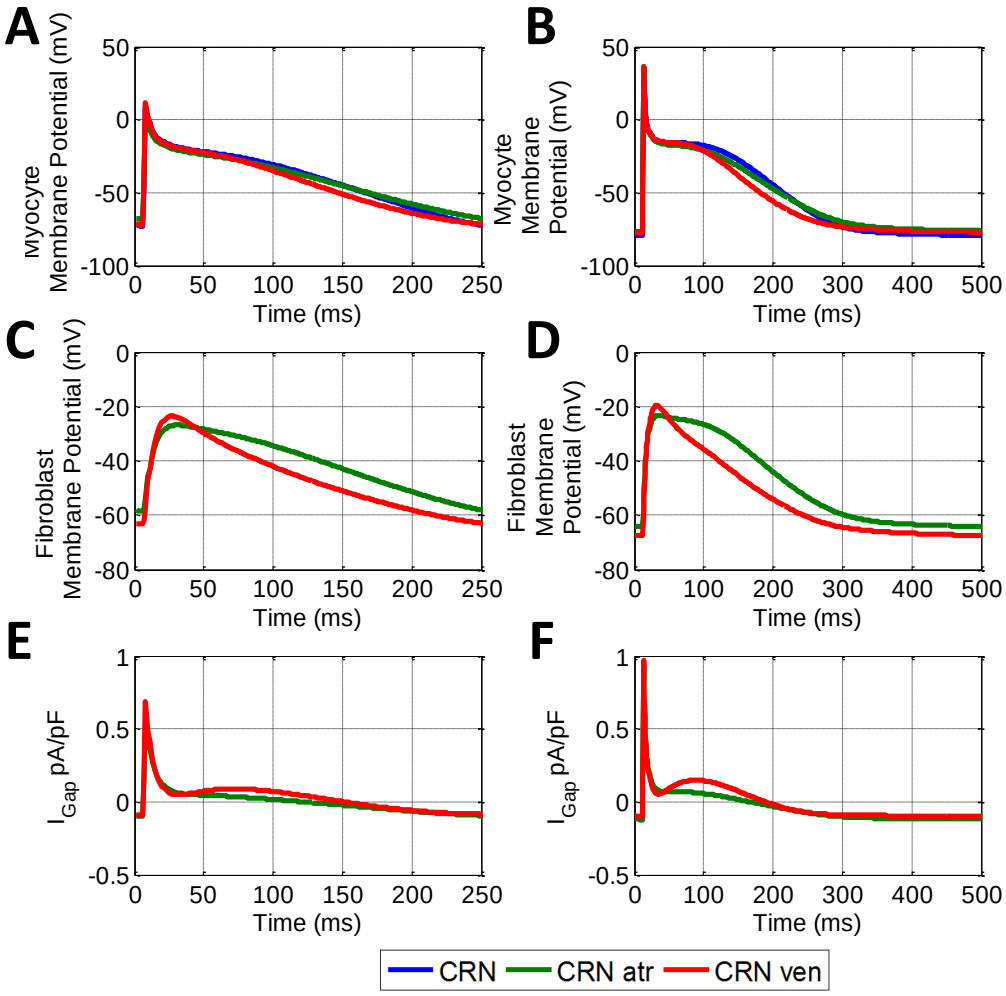


***Figure 17****. Effects of M-F coupling on AP in the atrial myocyte described by the CNR model. A and B shows the AP in atrial myocyte in various conditions; uncoupled CRN model (Blue) , CRN coupled with 2 human atrial fibroblasts (green) and CRN coupled with 2 ventricular fibroblasts (red).C and D show the fibroblast membrane potential for the coupled models and E and F show the M-F gap junction current ($I_{Gap}$). The left hand column (A, C and E) shows these conditions at a BCL of 250ms and the right (B, D and F) for a BCL of 500ms.*

Figure 18 compares AP characteristics, such as the peak voltage and RMP, in cases (i)-(iii). The M-F coupling models (ii) and (iii) had lower peak voltage than the control CRN model (i) at a BCL of 300ms (Figure 18A). However at a BCL of 500 and 1000ms the difference from control were less than 2mV.

The RMP (Figure 18B) was increased (became more positive) compared to control in both M-F coupling models (ii) and (iii). At a BCL of 500 ms, in the model (ii) with atrial fibroblast the RMP was -76.5mV (Figure 18B) and in the model (iii) with ventricular fibroblast the RMP was -77.5mV, compared to -79.8mV in the CRN model (i). RMP is particularly important during a period of fast pacing (Figure 18B) as it can influence the initiation of the next AP. The lowest RMP with atrial fibroblasts) is seen across all BCLs.

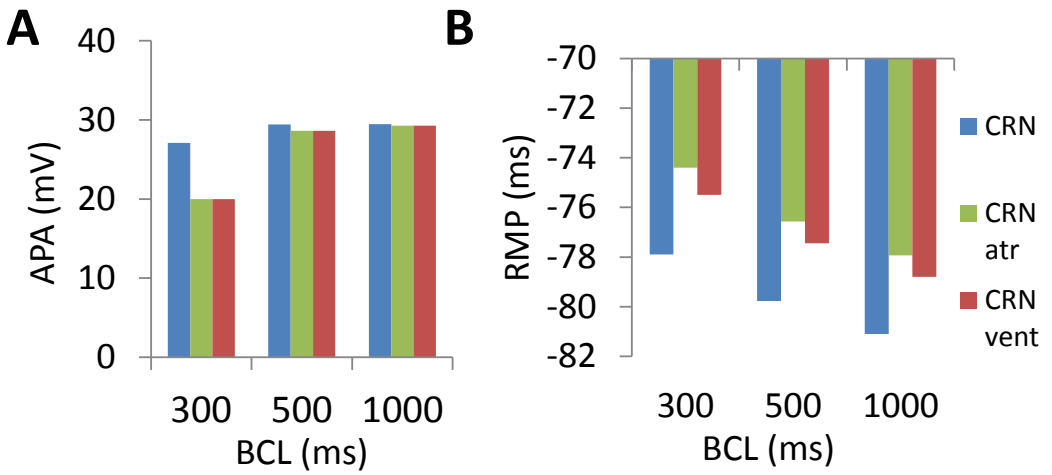


***Figure 18***. *AP Amplitude, APA, and RMP of the M-F coupling models. All plots use the colour code: blue= uncoupled CRN myocyte model, green= M-F coupling model with atrial fibroblasts and red= M-F coupling model with ventricular fibroblasts. A: APA at BCLs of 300, 500 and 1000ms, B: RMP at 300, 500 and 1000ms.*

The membrane potential in fibroblasts (Figure 17C and D) for the M-F coupling model was purely electrotonic due to the coupling with the myocyte and had substantially lower amplitude than that of the myocyte. The atrial fibroblast had a slower repolarisation and slightly lower amplitude than that of the coupled ventricular fibroblast. More importantly, it also had a higher resting potential (Figure 18B).

The dynamic effects of coupling a CRN myocyte with the developed atrial fibroblast model significantly changed the refractoriness of the myocyte. There was little difference in APD between the M-F coupling model with atrial fibroblasts (ii) and the control (i) except for at a high pacing rate, e.g. at a BCL of 200ms (Figure 19). In comparison, the M-F coupling model with ventricular fibroblasts (iii) reduced the APD throughout the range of BCLs, with a maximum reduction of 21ms. Effects of M-F coupling on APD became more pronounced in both models (ii) and (iii) as the number of fibroblasts coupled to each myocyte was increased from 2 to 4 and 6 (Figure 20).

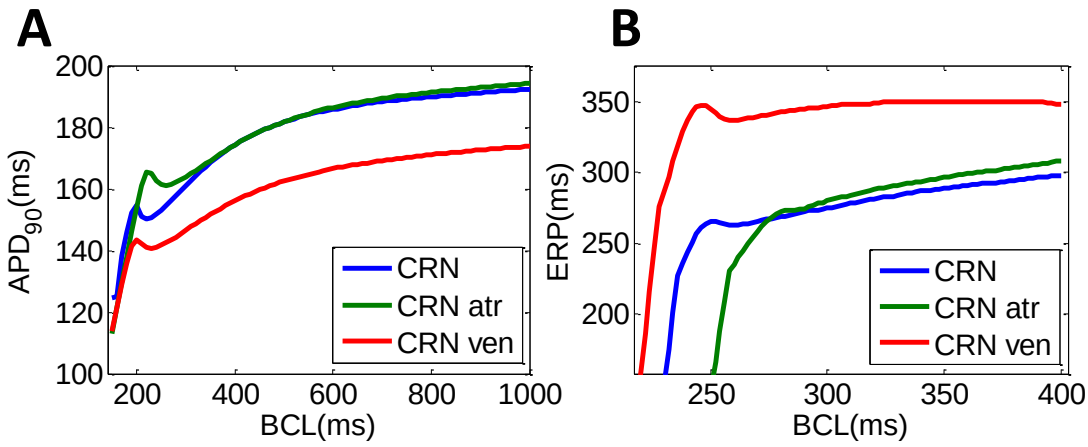


***Figure 19***. *The APD and ERP differences between the M-F coupling models. A: APD differences between M-F coupling models with the uncoupled CRN myocyte model (blue). The M-F coupling with atrial fibroblasts is shown in green and the M-F coupling with ventricular fibroblasts in red. B: ERP differences between the M-F coupling models and the uncoupled model are more pronounced.*

Effects of M-F coupling on ERP were more pronounced than those on APD in both M-F coupling models (ii) and (iii). ERP in the M-F coupling model with atrial fibroblasts (ii) was larger than that in control (i) by about 5-10ms at BCLs above 300ms, but dropped off rapidly at BCL was decreased below 275ms (Figure *19*B).

ERP in the M-F coupling model with ventricular fibroblasts (ii) was substantially larger than that in control (i) by about 50-100ms across the range of BCLs.

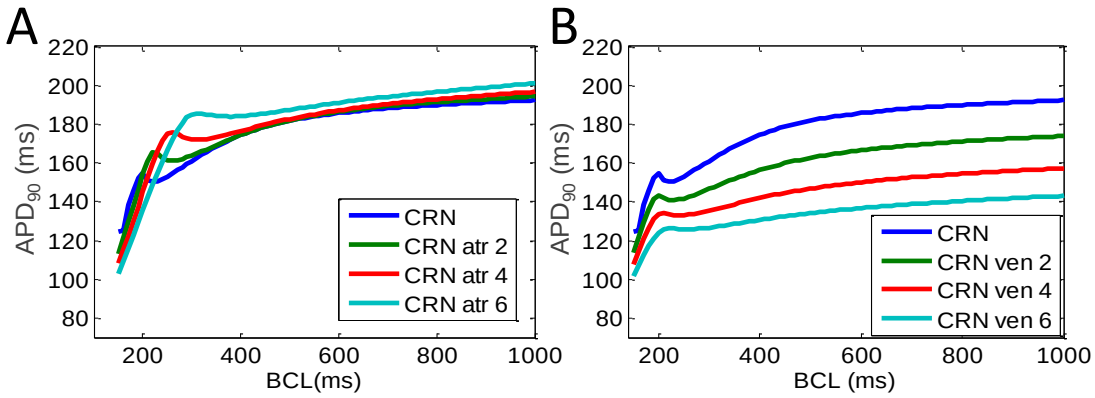


***Figure 20.*** *Effects on APD of the increased levels of M-F coupling. As the number of couple fibroblasts in increased up to 6, the M-F coupling model with atrial fibroblasts (A) shows an increase in APD, whereas the M-F coupling model with ventricular fibroblasts (b) shows a substantial decrease in APD. The colour code is as follows: blue= uncoupled CRN model, green= 2 fibroblasts, red=4 fibroblasts and cyan=6 fibroblasts.*

The excitation threshold for the stimulus current was also investigated (Figure 21) for the models. In the M-F coupling model (ii) with atrial fibroblasts, the threshold was -15.30 pA/pF at the BCL of 400 ms. It was significantly lower when compared to both the uncoupled myocyte model (i) (-18.30 mA/mS) and the M-F coupling model (iii) with ventricular fibroblasts (-16.70 mA/mS). Changes of the excitation threshold in models (ii) and (iii) compared to control CRN (i) correlated with the respective changes in the RMP: higher (more positive, but lower absolute value) RMP corresponded to the lower excitation threshold (compare Figure 17B and Figure 20). As the M-F coupling strength was increased (by increasing the number of fibroblasts coupled to a myocyte) the excitation threshold was reduced, as seen in Figure 21. This can also be explained by the higher RMP in the atrial fibroblast,

resulting in a stronger current flowing from the fibroblast into the myocyte during phase 4 of the AP.

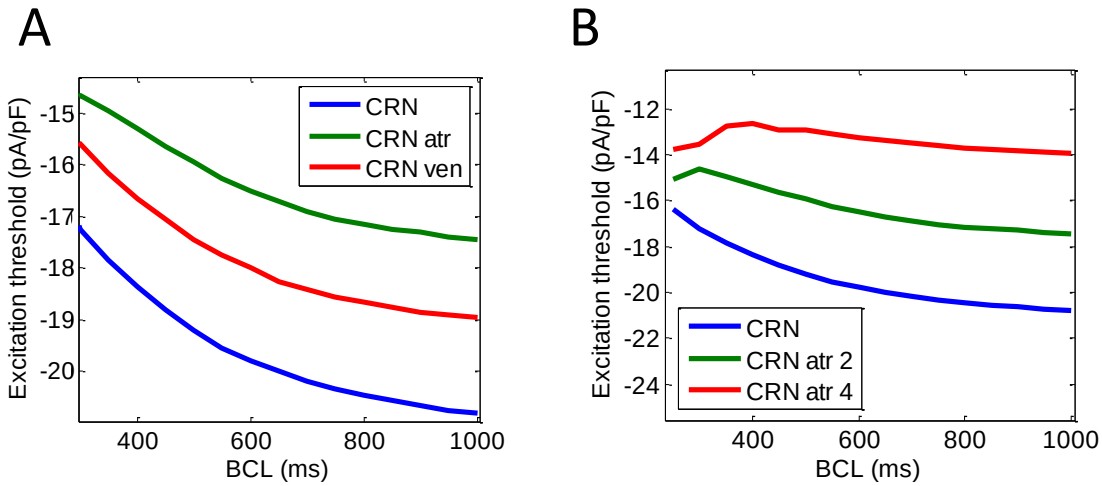


***Figure 21**. The excitation threshold for the M-F coupling models. A: the excitation threshold for the two M-F coupling models and the uncoupled CRN myocyte model (same colour code as Figure 19). B: the M-F coupling model with an increasing number of atrial fibroblasts (blue=uncoupled CRN model, green=2 fibroblasts, red=4 fibroblasts).*

### 3.3.3 Additional electrophysiological effects

The effects of the ionic remodelling, M-F coupling and M-F coupling combined with ionic remodelling, were investigated for comparison between the conditions (Figure 22A). APD in the CRN model is reduced by 40%, due solely to the ionic remodelling, with an additional 1.4% increase when combined with the proposed fibroblast model and a 1.4% decrease when combined with the MacCannell et al. ventricular fibroblast model. Thus, effects on M-F coupling on APD in the remodelled myocytes were incremental. ERP was similarly overwhelmed by ionic remodelling with M-F coupling only providing incremental changes.

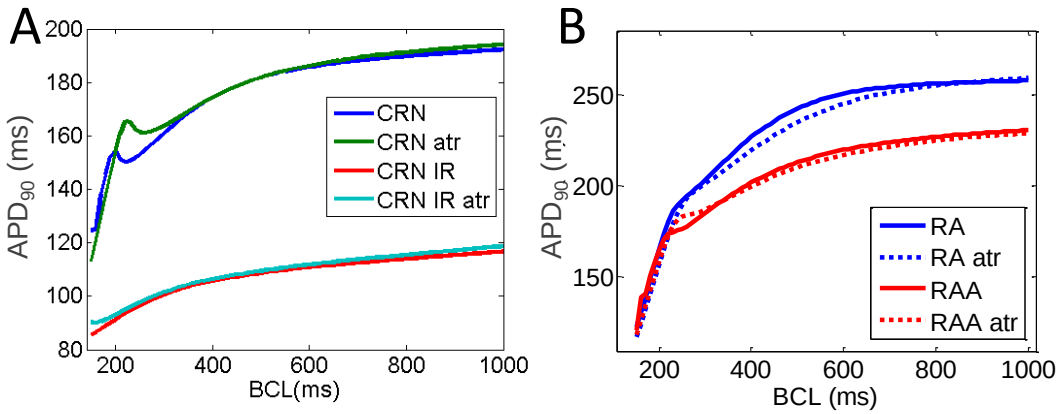


***Figure 22***. *Comparison of the effects of fibroblast coupling and ionic remodelling and heterogeneity. A: $APD_{90}$ differences for the developed M-F model (green), ionic remodelling (IR, red) and both combined (IR atr, cyan). B: $APD_{90}$ differences between different region, with and without M-F coupling. Blue shows right atrial tissue and RAA tissue, solid lines are the uncoupled CRN model and dashed show the atrial M-F coupled model.*

Utilising the regional heterogeneity developed by Colman et al.[39] the effects that the new fibroblast coupling model had on the regional ionic heterogeneity were analysed (Figure 22). The model had a negligible effect on heterogeneity in the right atrium.

Conduction velocity was investigated in 1D (Figure 23A), due to its contribution to arrhythmogenesis. Both M-F coupling models reduced the conduction velocity compared to the control but the ventricular M-F model had the greater effect. This can be explained by the longer ERP in the latter case (Figure 18B). The peak $I_{Na}$ was investigated, in order to find a mechanism for the differences in conduction velocity (Figure 23B).

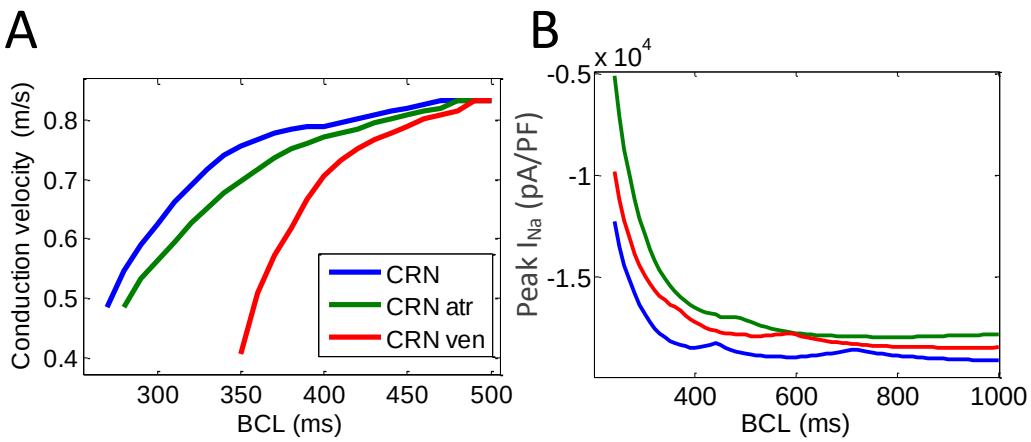


***Figure 23***. *Conduction velocity and maximum $I_{Na}$ for different M-F coupling models. A: shows the conduction velocity restitution, and B shows the restitution of the peak sodium current for the various coupling conditions. Coupling with the ventricular fibroblast model (red) resulted in a greater reduction in conduction velocity than that with the atrial fibroblast model (green), as compared to the uncoupled CRN myocyte model (blue).*

The M-F coupling models had reduced current magnitudes compared to the uncoupled CRN model, with the smallest $I_{Na}$ seen due to coupling with atrial fibroblasts at high pacing rates. This can be explained by the more positive RMP in atrial fibroblasts (Figure 17B), resulting in a stronger electrotonic M-F current, $I_{Gap}$ (Figure 17E and F) and partial inactivation of $I_{Na}$. Shorter ERP and higher CV in this case (compared to the M-F coupling with ventricular fibroblast) may be explained by a better balance between the reduction of $I_{Na}$ and increase of $I_{Gap}$ (see below).

### 3.4. Discussion

A novel model was developed for the atrial fibroblast, which is more relevant to atrial electrophysiology than the existing ventricular fibroblast models and gives insight into the arrhythmogenic effects of M-F coupling in the atria. The model simulations illustrate the effects of M-F coupling on atrial electrical properties are

more subtle than the ventricular fibroblast model. M-F coupling increases the RMP of the myocyte, which effectively reduces the excitation threshold. This behaviour can be responsible for regional conduction block and may contribute to atrial arrhythmogenesis, for example by facilitating re-entrant wave propagation. Therefore, the model of atrial fibroblast and M-F coupling provides a valuable tool for studying arrhythmogenic mechanisms for AF, and the models will be integrated into a 3D human atrial model in the further chapters of this study.

### 3.4.1. Effects of the M-F coupling

Previous studies have shown that changes in RMP of the fibroblast have significant effects on the electrophysiological properties of the myocyte coupled to it[56,92,95]. Models that present a more negative fibroblast RMP, such as MacCannell et al., require high levels of M-F coupling and gap junction conductance (up to 30 fibroblasts and 138nS)[95], which is far higher than has been recorded in vitro.

During the early phases of AP, the fibroblast in the M-F model acts as a current sink effectively reducing the upstroke of the myocyte, with the APA being reduced by 5mV in the atrial fibroblast model (Figure 19A). This behaviour has been shown in other studies [56,92,93] but with larger coupling conductances. The reduction in APA could slow down the propagation in the tissue due to the reduced current transferred to neighbouring cells. During the later phases of the AP, the fibroblast in the M-F model acts as a current source, prolonging the repolarisation phase and increasing the ERP (Figure 18B). This is a similar finding to that by Maleckar et al. and Jacquemet et al [92,93], both studies used a modified MacCannell et al. model

with a higher fibroblast RMP (-31.4mV) based on data at the upper limit of the experimentally reported physiological range[81,88].

The excitation threshold decrease in the model of a myocyte coupled to fibroblasts is due to the increase in the myocyte RMP (caused by inflowing $I_{Gap}$) because of the relatively higher RMP of the fibroblasts. This can be observed in Figure 21B: which demonstrates that when the number of coupled fibroblasts is increased the excitation threshold is reduced.

During the RMP phase, fibroblasts act as a current source for the myocyte, which may also contribute to the reduction in APA and CV due to a partial inactivation of $I_{Na}$ (Figure 23B) Differences between CV, ERP and excitation threshold between the M-F coupling models with ventricular and atrial fibroblasts may be explained by a rate-dependent balance between the increase of $I_{Gap}$ due to the M-F differences in RMP and the resultant decrease of $I_{Na}$.

Fibrosis has varying distributions within tissue for different disease phenotypes. One of these phenotypes is regional fibrosis known as patchy fibrosis. In this condition there is an observable increase in fibrosis density confined to specific locations throughout the organ. In these regions, changes in ERP and CV heterogeneity due to increased M-F coupling could lead to wave break and initiation of AF. Note that structural discontinuity of the tissue caused by fibrosis can also cause a stable rotor to break down into multiple wavelets. This is a behaviour more akin to AF; which will be discussed in further chapters.

### 3.4.2. Comparison between atrial and ventricular fibroblast models

The MacCannell et al. model of ventricular fibroblast and its variants is the most detailed existing fibroblast model, which is why it has been used it as a benchmark for the atrial model. M-F coupling parameters in the atrial model were set at lower level (0.5pS) than in the MacCannell et al. study[93], which corresponds better to experimental observations of a small number and extent of M-F couplings.

The RMP of an uncoupled atrial fibroblast in the model was -42mV, which was more positive than that in the MacCannell et al. ventricular fibroblast model (-47mV) and other ventricular models[93–95]. This is more representative of atrial physiology (Table 2)[93]. The atrial M-F coupling model also produced lower excitation thresholds and lower ERP, and as a result higher CV, than the MacCannell et al. model. Substantially shorter ERP and higher CV in the atrial M-F model may be explained by a better balance between the reduction of $I_{Na}$ and increase of $I_{Gap}$ (Figure 23). Using the atrial fibroblast model instead of the existing ventricular fibroblast model in 3D human atrial modelling could lead to vastly different behaviour, which is discussed in chapter.4.

### 3.4.3. Effects of ionic remodelling and heterogeneity

Ionic remodelling is strongly linked with AF progression and has been observed in both animal and human studies of AF. This type of remodelling leads to a large reduction of APD and ERP, which has previously been modelled in great detail and has been found to be arrhythmogenic.[42] When M-F coupling was combined with ionic remodelling, the additional effects on the APD and ERP in a single myocyte were incremental. The results show that compared to ionic remodelling, M-F

coupling has an insignificant effect suggesting that diffuse fibrosis may not be a mechanism for AF maintenance. Fibrosis can be induced rapidly as a pathology of other disorders (such as heart failure) or incrementally with age. In combination with the structural effects of fibrosis, may provide substrate for AF initiation. This will be further investigated in Chapter 5.

Electrophysiological heterogeneity of the atria has been linked to the AF genesis, as it can lead to wave breakdown and complex wave dynamics[38]. M-F coupling in the atrial model did not lead to significantly increased heterogeneity in the right atria. However, effects on atrial heterogeneity associated with patchy fibrosis can be more substantial (Chapter 5).

### 3.4.4. Limitations

The major limitation of this work is a lack of experimental validation for the electrophysiological effects of fibrosis at the cell level, such as changes in APD and ERP. However, the same lack of data highlights the importance of modelling and simulation in order to better understand the problem. Further experimental measurements in-vivo are required for the validation of the M-F coupling effects observed in the models.

### 3.4.5. Conclusion

In conclusion, the M-F coupling model with atrial fibroblasts had more modest electrophysiological effects on APD and ERP than ventricular fibroblast models. However, it presented different arrhythmogenic properties, primarily through the relatively high RMP in atrial fibroblasts, and as a result, reduced myocyte excitability and conduction velocity in atrial tissue. The utilization of more

comprehensive experimental data for the novel atrial fibroblast model, compared to the existing models for ventricular fibroblasts, make it more representative of atrial electrophysiology and better suited for the studies of M-F coupling in the atria.

# 4. 3D human atrial model

## 4.1. Introduction

AF is a complex condition that requires better understanding, from cellular to whole organ level. This is evident from the difficulty of treating the disorder clinically after decades of extensive research. Both drug therapy and catheter ablation have low long-term effectiveness, which may be due to the lack of mechanistic understanding of the treatment beyond the cellular electrophysiology level and the nature of ablated tissue substrate.

### 4.1.1. Atrial structural effects

Various structural factors that may affect AF arise from the complexity of atrial geometry; such as shape, wall thickness and curvature, complex fibre arrangement, AF-induced remodelling and the development of heterogeneous fibrosis. They have all been shown[38,97–99] to influence the propagation of excitation waves through the atria. The individual effects of these factors on arrhythmogenesis are hard to explicitly quantify and they may act cumulatively.

Atrial shape is an indicator for recurrence of post ablation AF[100] and may have functional effects that promote AF. This may be a result of the curvature of the atrial walls, which can be highly convoluted, especially around the PVs and within the atrial appendages. It has been shown in biophysical simulations that wavefront curvature can effect conduction velocity and promote vortex shedding and initiate re-entrant waves.[101] Moreover, the surface curvature can result in the drift of re-entrant rotors, and hence play a role in their ultimate location in the atria[97]. The

knowledge of such locations is important during ablation that targets the rotors sustaining AF. Changes in the atrial wall thickness have also been shown to generate re-entry and subsequent rotor drifts.[102] The potential mechanism of these phenomena is source-sink mismatch due to irregular geometrical features, such as wall thickness gradients.[40,103]

The myocardium, like all muscle is comprised of fibres that allow for efficient transmission of electrical signals and to aid tissue contraction. The consequence of the tissues electrophysiological properties is anisotropic conduction. Propagation along the fibre is accelerated by the predominantly longitudinal coupling of the cells. The majority of gap junctions are localised at the distal ends of elongated atrial myocytes. Fast conduction is particularly important in larger bundles such as the CT and BB, which carry the electrical excitation waves from the SAN to the ventricles and the LA, respectively. The overall structure of fibres throughout the organ determine the conduction pattern for the waves[99] and therefore can drastically influences arrhythmogenesis.[51,104]

Further to complex and variable fibre arrangements throughout the atria, atrial tissue is transmurally inhomogeneous and can possess distinct, layers of tissue. This is most notable in the RA,[105] where the large fibrous pectinate muscles have a distinct difference in fibre orientation and structure to that of the adjacent smother myocardium. A major difficulty in studying atrial fibre structure is the thinness of the atrial wall which makes conventional imaging methods difficult (Chapter 6). A recent successful reconstruction of the fibre orientation in ex-vivo canine atria was based on the application of a novel micro-CT technique[106]. However there are

significant physiological differences between species making this dataset not directly applicable for human atrial modelling. Recent human models have used rule-based fibre orientation based on ex-vivo knowledge (discussed in this chapter).

On the functional level, the local atrial geometry, fibre orientation and source-to-sink mismatches all translate into the conduction velocity (CV) of electrical waves. Changes in CV and CV heterogeneities have been linked to arrhythmogenesis.[107–109,110]

### 4.1.2. Structural effects of fibrosis

As discussed in Chapter.2, fibrosis has substantial structural (through interstitial depositions of collagen) and electrophysiological (through M-F coupling) effects on atrial tissue. However, structural remodelling due to depositions of collagen itself also affects the tissues electrophysiological properties, such as the conduction velocity and anisotropy. It has been shown that increased fibrosis levels are associated with slower conduction in atrial tissue[111,112]. A possible contribution to this is the increasing separation of fibres and the down-regulation of Cx43 associated with fibrosis[113]. Fibrosis also has a profound effect on the anisotropy of the tissue, due to the predominantly lateral collagen depositions in interstitial fibrosis. Thus, anisotropy is increased with fibrosis which has been measured in tissue (see Table *4*, page 83)[81,114]. Additionally, tissue anisotropy may be increased by compensatory gap junction remodelling, which results in the lateralisation of Cx40 and Cx43 expression in response to the reduced lateral conduction caused by adjacent fibrosis deposition[98].

| Modelling Studies | Anisotropy Ratios Velocity $CV_L/ CV_T$ | Diffusion $D_L/D_T$ | Condition | Source |
|---|---|---|---|---|
| Aslanidi et al. [38] | ~1.9 | 10 | Sinus Rhythm | Human |
| Tobon et al. [115] | - | 1- 9 | Sinus Rhythm | Human (LA - CT) |
| Seeman et al. [116] | - | 1-9 | Sinus Rhythm | Human (LA - CT) |
| Krueger et al. [117] | - | 1-23.25 | Sinus Rhythm | Human (LA - PM) |
| Harrild et al. [118] | - | 7.5 | Sinus Rhythm | Human |

| Experimental studies | Anisotropy Ratios Velocity $CV_L/ CV_T$ | Diffusion $D_L/D_T$ | Condition | Source |
|---|---|---|---|---|
| Yamamoto et al.[119] | 1.4 | - | Sinus Rhythm | Rabbit (SAN) |
| Liu et al. [120] | 1.95 | - | Atrial Flutter | Human |
| Hansson et al.[121] | 1.14 - 1.8 | - | Sinus Rhythm | Human (CT) |
| Kleber et al. [122] | 2.1 , 10 | - | Sinus Rhythm | Human (RA,CT) |
| Koura et al. [123] | 1 - 1.42 | - | Aging | Dog (young - old) |
| Verheule et al. [124] | 1.8 - 4.5 | - | AF and Fibrosis | Goat |
| Krul et al. [114] | 1.05–13.4 | - | AF | Human (LAA) |
| Angel et al. [125] | 1.47 - 1.72 | - | AF | Goat |

***Table 4****. Anisotropy ratios measured in experiments and used in existing models.*

### 4.1.3. Investigating cardiac electrophysiology

Clinical electrophysiology studies, such as body surface mapping and catheter based endocardial activation mapping cannot account for the unique structural factors associated with the atria for an individual patient, without accurate registration

with a pre-scanned detailed 3D image. Although this is possible in AF patients, registration of these images is difficult to implement. Both clinical mapping and current imaging methods have too low resolution to provide detailed information and elucidate any mechanistic links between the structure and function in AF. Computation modelling has been applied to dissect 3D electrophysiological dynamics in situations when clinical and experimental methods fail to provide detailed insights.

Early 3D models relied on simplified geometries[126] or small-scale geometries (like the pectinate muscles[104]) but as computational power has increased; models have become more detailed and focused toward patient specificity. The older models showed the importance of increased biophysiological detail, as more complex behaviours could be investigated. Recent atrial models focused on enhancing biophysical details such as: patient specific geometries, fibre orientation[115,117,127], fibrosis[98] and regional electrophysiological heterogeneity[69]. There is a need for integration of all of these factors into a comprehensive modelling framework to investigate the amalgamated effects.

The aim of this work is to incorporate the atrial model for M-F coupling with a 3D human atrial model that accounts for details of atrial structure, regional heterogeneity and anisotropy, to investigate the arising arrhythmogenic effects. The next section describes how the biophysically detailed 3D atrial model was created. The rest of this chapter will focus on simulations of effects of uniform diffuse fibrosis in the 3D atria. The next chapter will apply similar models to explore the respective effects of image-based patchy fibrosis.

## 4.2. Methods

### 4.2.1. Atrial geometry and fibre orientation

To provide the anatomical structure of the atria for simulations, a 3D volumetric geometry is required. The "Visible Human Project" is a collection of anatomical datasets created by the US National Library of Medicine. Ex-vivo images were created by cryo-sectioning an entire cadaver; photographs of each section were taken and digitised.

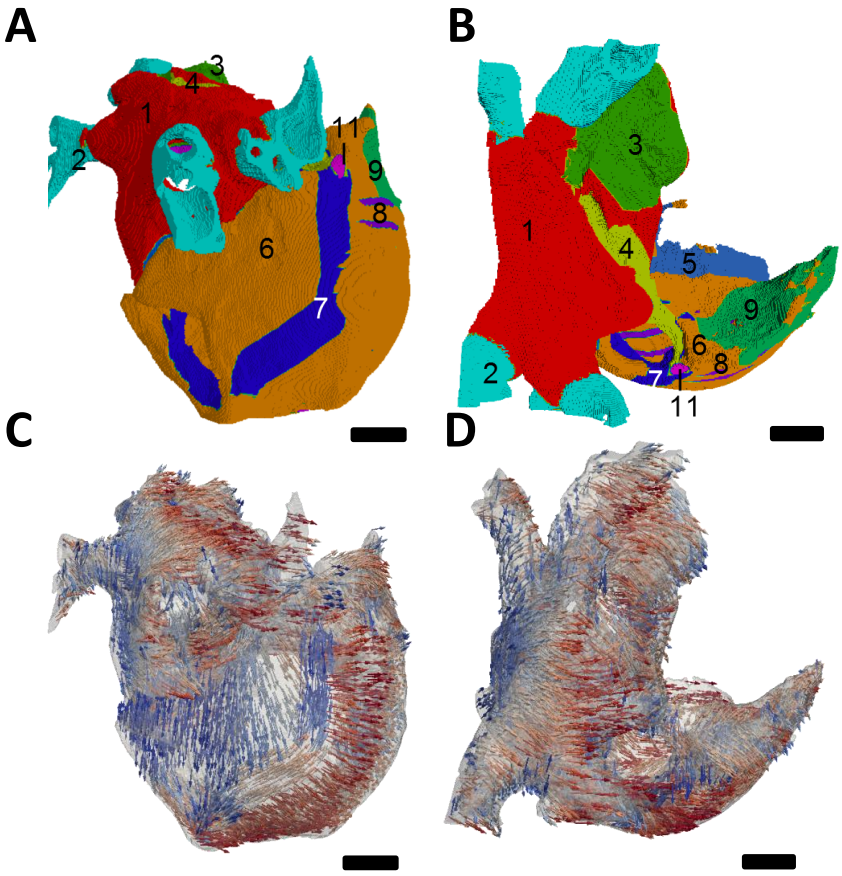


***Figure 24***. *Atrial geometry model based on the Visible Female dataset. A and B show the segmented regions of the atria, and C and D show fibre orientations; A and C are posterior views whereas B and D are transverse views. The segmented and labelled anatomically distinctive regions are, 1=LA, 2=PV, 3=LAA, 4=BB, 5=AV valve, 6=RA, 7=CT, 8=PM, 9=RAA, 10=AS (not shown) and 11=SAN. The colours in panels C and D illustrate the magnitude of the X axis component of the fibre orientation vector. The dataset has a 0.33mm resolution*

Regions of interest, such as the 3D atria, were later segmented and reconstructed (Figure 24A and B). The specific 3D atrial geometry used in the present study was from the "Visible Human Female" dataset. The segmented atrial geometry was developed by a collaborating group at the Karlsruhe Institute of Technology[5] and was used as the geometric basis for the biophysical model.

Although this dataset cannot be said to be patient specific, it was the most detailed human atrial dataset available when building the model. The fibres were developed using an algorithmic approach to create a vector field of aligned fibres based upon landmarks observed in ex-vivo anatomical studies of human atria[117].

Some post processing was required to efficiently integrate the fibre dataset into the model. Since the rule-based fibre orientation was introduced region-by-region, the original dataset had discontinuities at borders between such regions. These discontinuities resulted in numerical instabilities during simulations. In these areas a smoothing filter was applied. The filter was a 5 voxel neighbourhood mean filter masked by the 3D geometry.

### 4.2.2. 3D whole atria model

The single cell models used in this work, discussed in chapters 2 and 3, were incorporated into a framework that included atrial geometric shape, fibre orientation and segmentation of electrophysiologically distinctive regions. Regional electrophysiology models described in Chapter 2 were allocated to the relevant segmented region (Figure 24A and B).

The mathematical model (equation 10) used to simulate 3D atria is described in section.2.4.2. The model was solved numerically using the explicit forward method, with the dataset resolution of 0.33mm voxels used as the spatial step of numerical integration and a time step of 0.005ms. Although the spatial step was determined by the geometry dataset, both the space and time steps were varied to check to a basic convergence of the results. During simulations described in this section, components of the diffusion tensor (***D***) were varied. Thus, by reducing the longitudinal and transverse diffusion coefficients (see below), AF-induced tissue remodelling and some aspects of fibrotic conditions could be simulated.

AF was initiated by fast pacing in the 3D atria model.[42] To reduce computational time, initial conditions for all variables were obtained by simulating steadily paced single cell models prior to the 3D atria simulation. The single cell model for each region was paced 30 times at a given BCL, and the values for all variables were saved to a .txt file, to be used as an input by the 3D atrial model. Finally, the 3D model was paced between 3-10 times (dependent on the conditions) at the same BCL to initiate AF.

Re-entry was initiated in the model through fast pacing in the RAA, allowing for the wave to propagate perpendicularly to the cristae terminalis to maximise the chance of wave block. This may not be physiologically accurate as ectopic beats most commonly originate from the PVs[128]. However RA ectopic foci have been observed in a significant number of patients, as well as in-vivo experiments[129]. This method of AF initiation has been applied before in computational atrial models.[38,39]

The model uses the 3D fibre vector array (Figure 24C and D) to calculate the diffusion tensor to each voxel dependant on the orientation of the fibre.[130] This calculation also requires the longitudinal and transverse diffusion coefficients, $D_L$ and $D_T$, where $D_L$ was constant at 0.3 $mm^2/ms$ and $D_T$ was varied as described below.

The complex geometric shape of the atria makes applying boundary conditions non-trivial. A boundary layer surrounding the outer surfaces (both epicardial and endocardial) is created based on calculating the surface normals for each voxel and applying the Neumann zero-flux boundary conditions along the normals[35]. This ensures that zero flux is maintained between the atrial surface and the respective boundary layer.

### 4.2.3. Simulated Conditions

The model settings were varied to simulate different conditions linked to fibrosis and AF (Table 5). Three levels of structural remodelling were developed to simulate different types of fibrosis. (1) Control, simulated with no structural remodelling-associated changes, where diffusion coefficients and anisotropy parameters simulate 'healthy' atrial tissue. (2) Diffuse fibrosis, with uniformly decreased diffusion coefficients simulating decreased levels of intercellular coupling associated with AF. (3) Interstitial fibrosis, simulated with increased anisotropy associated with high level of collagenous infiltration in long-term AF. In addition to these three conditions, variations of electrophysiological parameters associated with AF were also investigated; M-F coupling (both with atrial and ventricular fibroblasts) and ionic remodelling.

Normal structural conditions were validated by comparing activation times simulated in the 3D atria model during sinus rhythm (SR), with the respective clinical measurements (Table 5 and Figure 25). Activation times were measured at various anatomically distinctive locations in both atria and were found to be within clinically reported data ranges. This provided a validation for the choice of $D_L$ = 0.3 $mm^2/ms$, as well as the variation of anisotropy ratio, $D_L/D_T$, from 10:1 to 16:1.

| **Diffusion coefficient ($D_L$)** ( $mm^2\,ms^{-1}$) | 0.3 | 0.3 | 0.12 | 0.12 | Clinical data by Lemery et al. [131] |
|---|---|---|---|---|---|
| **Anisotropy ratio ($D_L/D_T$)** | 10:1 | 16:1 | 10:1 | 16:1 | |
| **Arrival times (ms)** | | | | | |
| **1st SVC** | <10 | <10 | <10 | <10 | 26 ± 22 |
| **1st RUPV** | 40 | 50 | 80 | 80 | 75 ± 24 |
| **1st IVC** | 60 | 70 | 110 | 120 | 88 ± 33 |
| **Latest IVC** | 80 | 90 | 150 | 160 | - |
| **Latest RA** | 90 | 100 | 180 | 190 | 93 ± 17 |
| **1st LIPV** | 80 | 90 | 150 | 160 | 101 ± 23 |
| **Latest LA** | 100 | 110 | 190 | 200 | 116 ± 18 |

***Table 5****. Arrival times in the 3D atrial model, compared to clinical findings by Lemery et al.* [131]

For simulations of the diffuse fibrosis condition, a 60% reduction in the diffusion coefficient $D_L$ was applied, while the anisotropy ratio was maintained at 10:1. For simulations of the more severe interstitial fibrosis condition, an additional increase of the anisotropy ratio from 10:1 to 16:1 was applied.

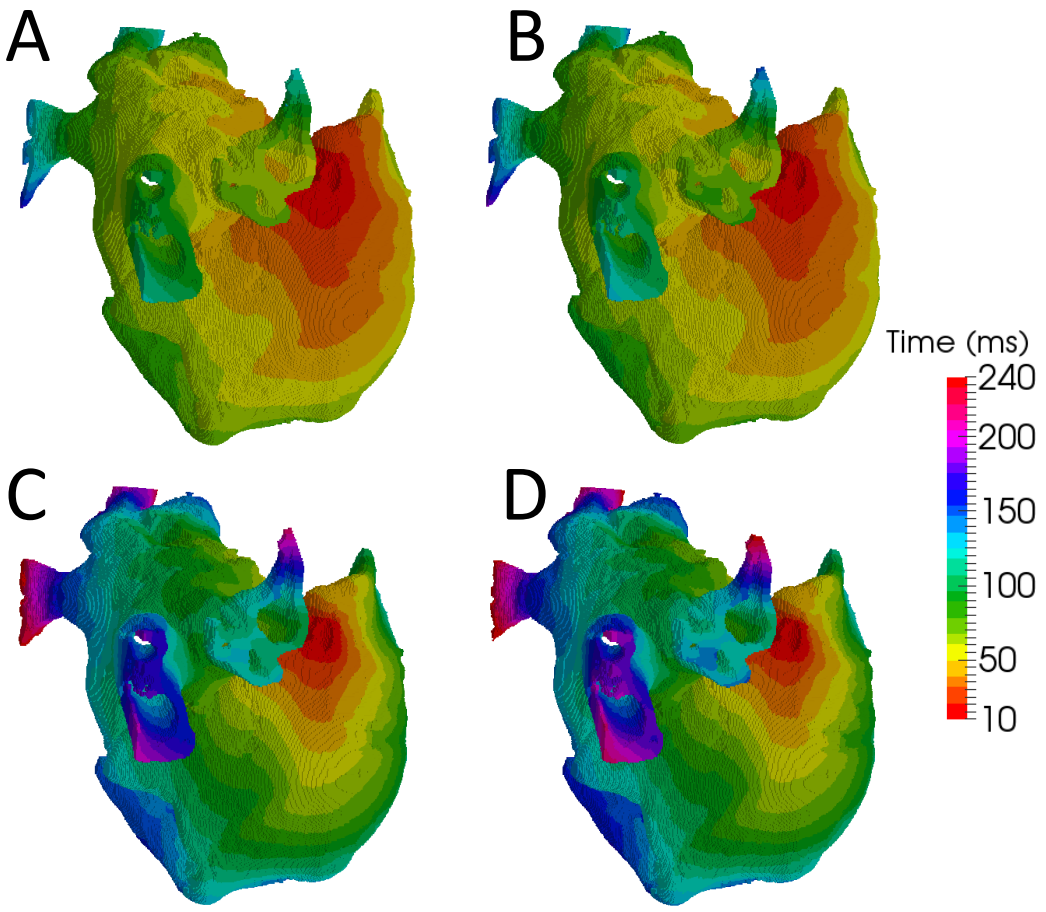


***Figure 25*** *Sinus rhythm activation maps simulated with the 3D atrial models for four different conditions. Left panels (A and C) show the low anisotropy ($D_L/D_T$ =10:1) model and the right (B and D) show high anisotropy ($D_L/D_T$ =16:1). A and B show control conditions with standard diffusion coefficient ($D_L$=0.3 $mm^2/ms$) and C and D show fibrotic conditions with the reduced diffusion coefficient ($D_L$=0.12 $mm^2/ms$). Region-specific activation times for the four conditions are compared to the respective experimental data in Table 5.*

In all structural remodelling conditions additional effects of M-F coupling, using either atrial or ventricular fibroblasts, were investigated. As with the single cell modelling presented in Chapter.3, both regional heterogeneity and ionic remodelling were also considered.

### 4.2.4. Visualisation of results

The 3D propagation results are displayed either as snapshots of voltage iso-contours at successive moments of time or as full activation maps over a period of time (which is 250 ms, unless otherwise stated). The former is displayed using a non-linear rainbow colour scheme for the voltage iso-values ranging from -60 to +30mV. The snapshots were selected at different intervals of time to clearly show different behaviours. This was necessary because propagation phenomena, such as wave block or re-entry, rarely occurred at the same moments of time between simulated conditions. For the activation maps, the activation time is measured as the earliest time at which the voltage exceeds the threshold value of -40mV, the resulting activation maps were displayed using a linear rainbow colour scheme.

## 4.3. Results

### 4.3.1 Sinus Rhythm Activations

The atrial activation sequences simulated with the 3D model during SR stimulations at BCL of 300ms are shown in Figure 25. In simulations with a 'healthy' anisotropy ratio of 10:1 (Figure 25A and C), the wavefront was marginally more regular and the longitudinal activation along the CT was 10ms faster than in simulations with higher anisotropy of 16:1 (Figure 25B and D). Conduction velocity field in all possible 3D directions was difficult to accurately measure due to wall curvature in the 3D atria.

| Simulated condition | Type of re-entrant behaviour | Duration of re-entry (ms) |
|---|---|---|
| **No structural remodelling** | | |
| Control | Unstable re-entry | 1800 |
| M-F coupling (atrial fibroblast) | Unstable re-entry | 3480 |
| **Diffuse fibrosis** | | |
| Control | Unstable re-entry | 3400 |
| M-F coupling (atrial fibroblast) | Unstable re-entry | 2690 |
| M-F coupling (ventricular fibroblast) | Unstable re-entry | 11720 |
| Ionic remodelling | Stable rotor | Sustained |
| **Interstitial fibrosis** | | |
| Control | Re-entry followed by wave breakdown | Sustained |
| M-F coupling (atrial fibroblast) | Re-entry followed by wave breakdown | Sustained |

***Table 6****. Re-entry type and duration of 3D simulations. Re-entrant behaviour was considered sustained (similar to sustained AF) if it lasted for the entire duration of the simulation, which was 12 seconds.*

The higher anisotropy ratio of 16:1 enabled a better agreement of the simulation results with the clinical data by Lemery et al. (Table 5). This can be explained by the fact that the data was obtained from AF patients (although in sinus rhythm), and hence their atria can be better characterised by an 'unhealthy' set of parameters. Note that even in simulations with faster pacing rates (BCL of 260ms, which is closer to rates observed in AF), little difference was observed in wave pattern or

morphology between high and low anisotropy (not shown), with only small reductions (10-30ms) in activation times.

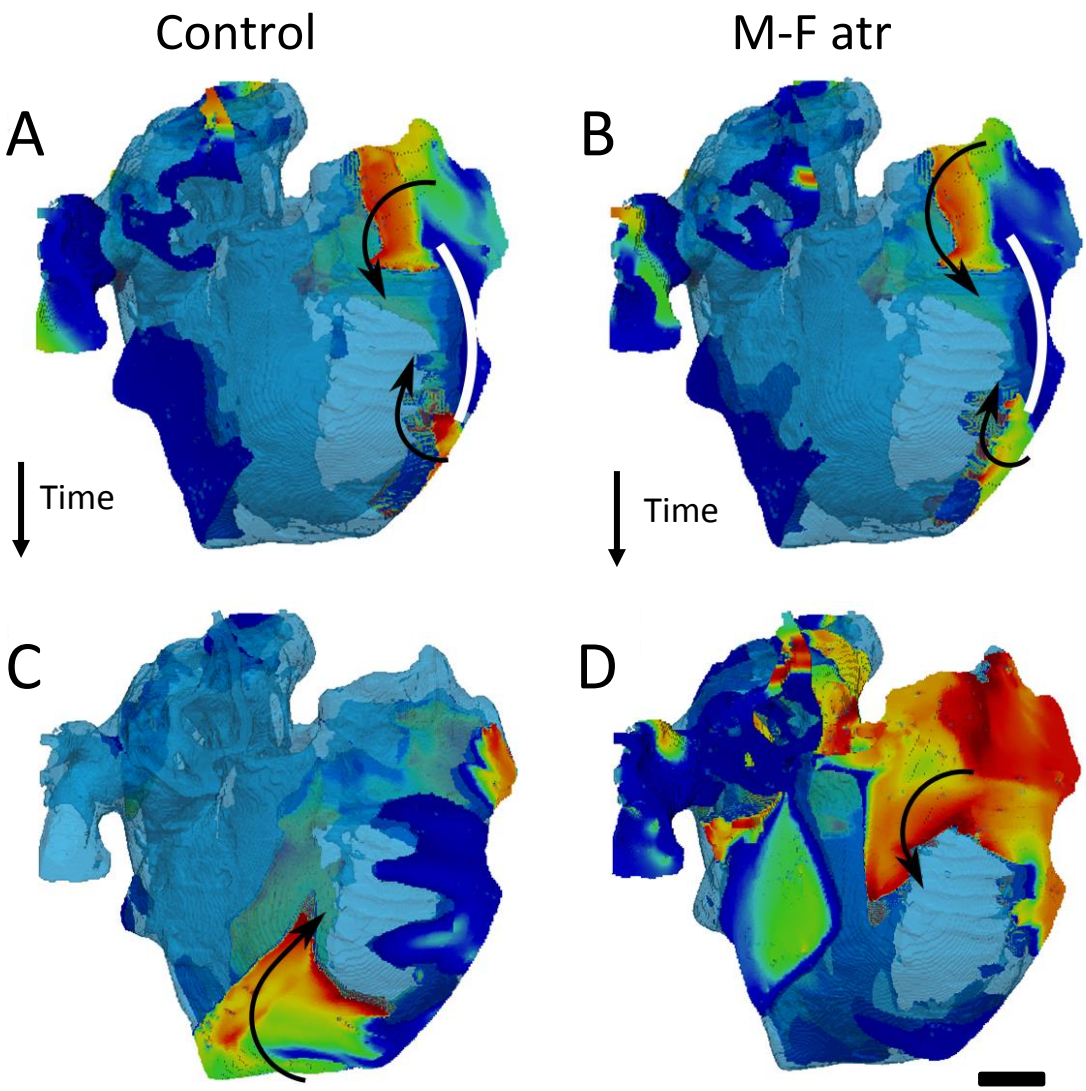


***Figure 26***. *Simulations of the 3D atria without structural remodelling, showing wave block and re-entry. A and C show two successive voltage snapshots in control (no M-F coupling), whereas B and D show the snapshots for the condition of M-F coupling (atrial fibroblast model) discussed in Chapter.3. Wave-block lines are indicated by the white line in A and B; wave direction is indicated by the black arrows. The time differences between A-C and B-D are not equal; the figures were chosen to best illustrate the re-entrant behaviour. The re-entry in these simulations was unstable and self-terminating.*

Reducing the diffusion coefficient $D_L$ (Figure 25C and D) for the diffuse fibrosis condition has a significant effect on the wavefront propagation. The total atrial

activation time was reduced by 50-70ms (referring to the latest activations in the RA and LA in Table 6). This substantial activation time reduction was in addition to the smaller reduction (10ms) due to high anisotropy (Figure 25D). Hence, the interstitial fibrosis condition, which combined decreased $D_L$ and increased anisotropy, was characterised by longest activation times (190-200ms) (Table 5).

### 4.3.2 Re-entrant Activations

Fast pacing in the anterior RA at a BCL of 235-260ms (dependant on conditions) resulted in a conduction block leading to wave breaks and re-entry in all simulated conditions (Figure 26, Figure 29 and Table 6). The conditions included both the structural changes, considered above (increased anisotropy and decreased diffusive coupling, associated with interstitial and diffuse fibrosis during AF) and the electrophysiological conditions described in Chapter 3 (control, M-F coupling using either atrial or ventricular fibroblast models or ionic remodelling).

Figure 26 shows 'healthy' tissue with no structural remodelling and M-F coupling effects. Figure 27 illustrates the effects of diffuse fibrosis with and without ionic remodelling and Figure 28 demonstrates the effects of diffuse fibrosis and M-F coupling of atrial and ventricular fibroblasts. Figure 29 shows the effects of interstitial fibrosis and M-F coupling. Table 6 summarises the behaviours of these simulations.

The precise location and timing of the wave-block varied depending on the condition considered and pacing rate used, but was always clearly observed between the CT and the pacing site. This is clearly seen in Figure 26 and Figure 29.

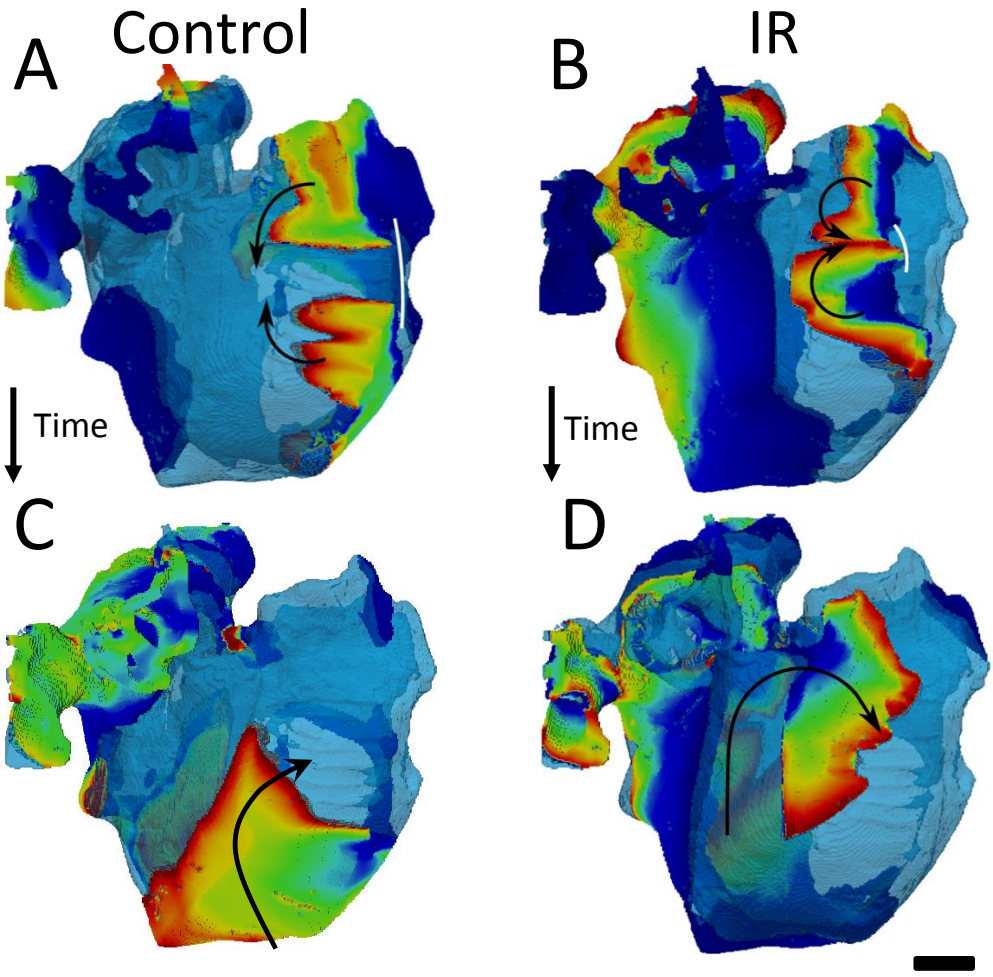


***Figure 27**. Simulations of the 3D atria model with fibrosis related structural remodelling and ionic remodelling (IR). This includes normal anisotropy and diffusion coefficient reduction. Panels A and C indicate control simulations with no electrophysiological alterations and the right (B and D) show those with ionic remodelling. The top row (A and B) show incidence of wave block (white lines) in the simulations and C and D show re-entry formation. Wave direction is indicated by the black arrows. The unstable wave seen in Figure 27A and C (A and C here) was not seen with ionic remodelling, rather a stable rotor was present (D).*

The extent of the wave block also greatly varied between conditions, for example as shown in Figure 27A and B for diffuse fibrosis with and without additional ionic remodelling. Not all wave-blocks developed into re-entry, however those that did-

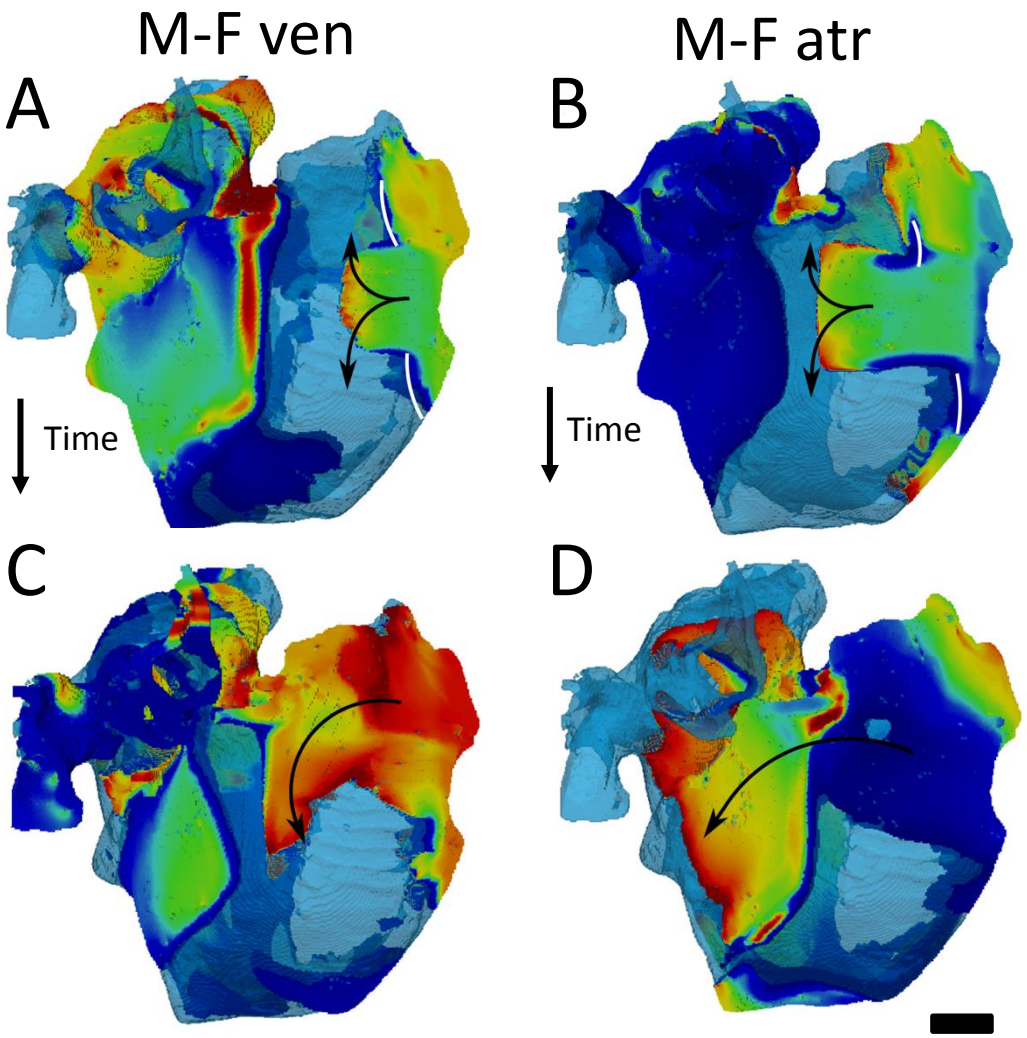


***Figure 28***. *Simulations of the 3D atria model with fibrosis related structural remodelling and M-F coupling. This includes normal anisotropy and diffusion coefficient reduction. Panels A and C indicate simulations with the developed atrial M-F coupling model and the right (B and D) show those with the MacCannell et al. ventricular fibroblast model. The top row (A and B) show incidence of wave block (white lines) in the simulations and C and D show re-entry formation. Wave direction is indicated by the black arrows. These simulations also showed unstable self-terminating re-entry. The nature of this behaviour was similar (although not visually identical) to that seen in Figure 27.*

initially formed two re-entrant waves (for example Figure 27A and B) persistent for a short duration of less than 3 periods. After this, one terminated and the other continued to propagate (for example Figure 27C and D). Self-termination of one from a pair of rotors can be explained by the asymmetry of conduction.

The re-entrant dynamics in both cases of no structural remodelling and diffuse fibrosis was characterised by a single self-terminating wave. This travelled through the atria with no apparent pattern or rotor focal point. The instability of this behaviour due to the long wavelength (when compared to ionic remodelling) meant that the wave would eventually travel to an area where re-entry was not possible, such as tissue near valve isthmuses or large vessels, and would self-terminate.

The duration of re-entry (Table 6) was also varied between different conditions. In all conditions with no structural remodelling (shown in Figure 26) and diffuse fibrosis (Figure 27C and Figure 28C and D) re-entry was self-terminating. The duration of re-entry before its self-termination was generally longer with diffuse fibrosis and M-F coupling (particularly with the ventricular fibroblast model) (Table 6). Only in conditions of ionic remodelling in addition to diffuse fibrosis (Figure 27B and D) was a stable rotor generated and sustained for the entire duration of simulation. In conditions of high anisotropy associated with interstitial fibrosis (Figure 29), stable rotors and secondary multiple wavelets persisted after 20s of simulation similar to sustained AF.

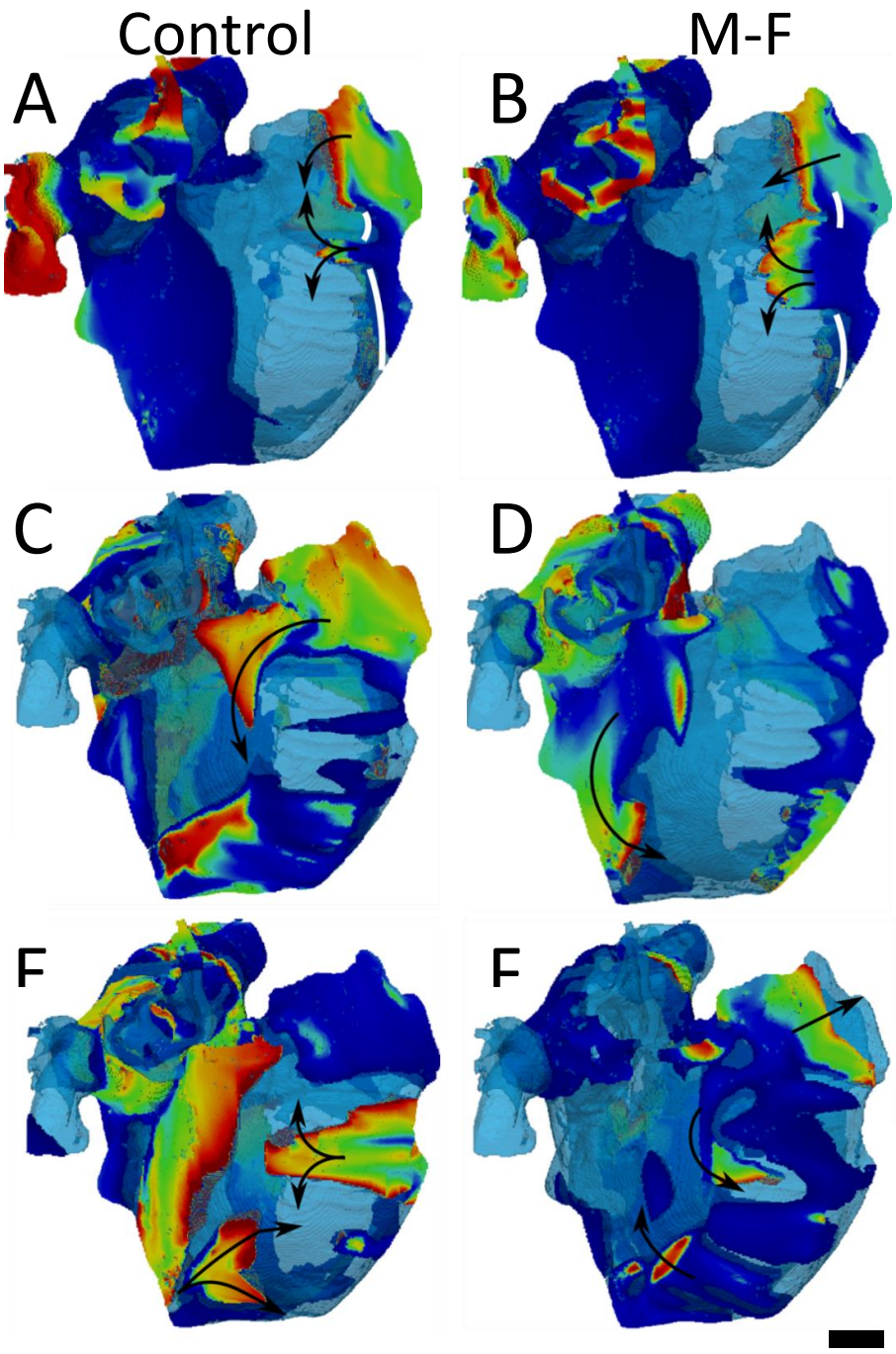


***Figure 29***. *Simulations of the 3D atria model with structural remodelling linked with AF-induced interstitial fibrosis. The latter includes both increased anisotropy and reduced diffusion coefficient. Left panels (A, C and E) show successive voltage snapshots in control (no M-F coupling) and the right panels (B,D and F) show the snapshots for the condition of M-F coupling (atrial fibroblast model). A and B show the initial wave blocks (white lines), and C and D show the re-entrant behaviour (long black arrows). E and F show multiple, independent wavelets indicated by the short black arrows.*

Re-entrant behaviour was induced by rapid pacing in all conditions but with different pacing frequencies, which reflect different ERPs in those conditions (Chapter 3). Different re-entrant dynamics observed were also linked with the variations of ERP, as well as CV, between those conditions (see details in Discussion). In most simulations with low anisotropy, only a single short-duration re-entrant wave was present (Figure 30B), with the only exception of ionic remodelling. Longer duration of re-entry between these conditions (Table 6) correlated with either shorter ERP (due to M-F coupling) or lower CV (due to diffuse fibrosis), both leading to a shorter wavelength. Ionic remodelling resulted in the shortest wavelength, and hence produced a stable rotor (Figure 30A). The mechanism for self-termination appeared to be the increased wavelength and larger extent of rotor meandering of the CRN compared to the ionic remodelled version. In these cases, the rotor easily reaches an edge or structural boundary and terminates due to the majority of atrial tissue being insufficiently repolarised.

Another pattern was observed in high anisotropy conditions linked with interstitial fibrosis. A dominant rotor was initiated due to the overall reduction of wavelength which broke down into a series of secondary wavelets (Figure 30C), with a general pattern of multiple wavelets propagating chaotically and independently, which is typical of clinical AF. Each wavelet lasted 50-200ms before being intersected by another wave. The complexity was not uniform as the number of waves varied throughout the simulation. In these simulations there was no evidence of a stable rotor. Diffuse fibrosis resulted in activation patterns with an intermediate level of complexity characterised by transient re-entry (Figure 30B)

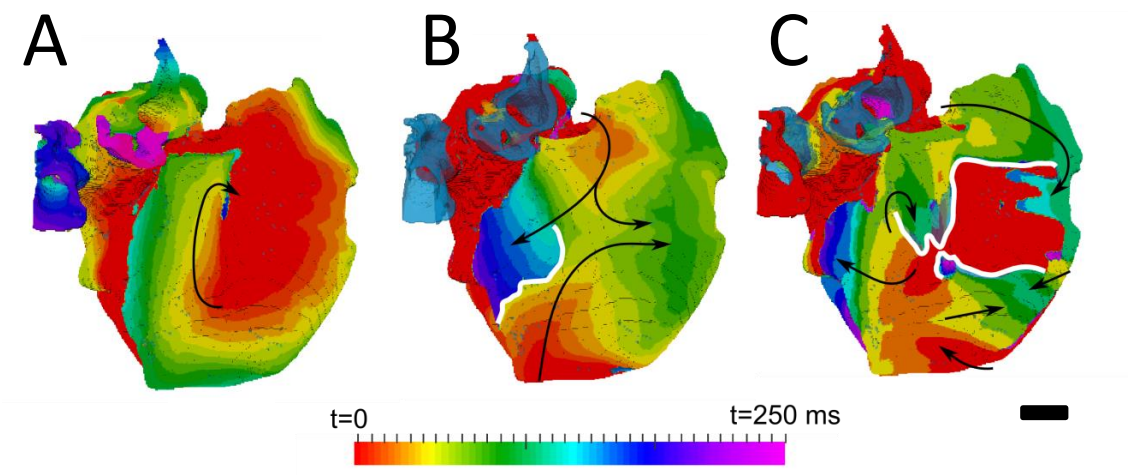


***Figure 30***. *Activation maps in the 3D atria model for typical patterns of observed re-entrant behaviours. A, shows a stable rotor, seen in the conditions with ionic remodelling. B, illustrates an unstable re-entrant wave in the conditions with diffuse fibrosis and C shows wave-breakdown in the conditions with interstitial fibrosis. Wave propagation directions are shown by the black arrows and wave-blocks are shown by the white lines. In B and C, the left atrium is fully activated at the initial moment of time t=0 and the PVs are repolarised and not activated (and hence, seen in the transparent blue colour corresponding to the tissue geometry) within the time range of these activation times.*

## 4.4. Discussion

The complexity of atrial structure and function, and their remodelling during AF, results in complex electrophysiological dynamics which cannot be adequately described by ex-vivo cell-to-tissue level studies or voltage mapping in patients, largely due to the unknown structure-function relationships. The 3D atria modelling enables the linking of atrial structure and function and allows the exploration of cell-to-organ AF mechanisms in-silico. Simulations of a novel 3D human atria model presented in this chapter show a range of re-entrant behaviours caused by various pathophysiological conditions associated with AF-induced fibrotic remodelling.

### 4.4.1. Validation of diffusion coefficients

Initially, the model was validated against clinical atrial activation data obtained in sinus rhythm. The simulated SR activation maps showed the archetypal elongation of the wavefront extending along the CT, which has been observed in-vivo.[132] The arrival times were comparable to clinical measurement by Lemery et al.[131] (see Table 5, page 89), with the exception of the first SVC activation. This was due to the segmentation of the SAN being too high on the CT (Figure 24)[69] in this particular geometry. The close match between activation times simulated and those found clinically validates the choice of parameters (diffusion coefficients) in the models. We also considered activations emanating from the entire SAN simultaneously, whereas in reality this process is not instantaneous and propagation inside the SAN is relatively slow. Besides, due to variation in atrial size and shape there is an inherent variation in activation times. Nevertheless, the simulation results are within the range of variability of the clinical data, with the best agreement found for the case of 16:1 anisotropy (Table 5).

### 4.4.2. 3D atrial simulations

Simulations of the 3D atrial model with no structural remodelling, i.e. without increased anisotropy and normal diffusion coefficients, produced unstable re-entry for a short duration. This was due to the fact that both ERP and CV in these conditions were relatively high (Chapter 3), resulting in a long wavelength comparable to the size of the atria. This behaviour was repeated in diffuse fibrosis simulations where the diffusion coefficients were decreased, but with re-entry duration increased as a result of decreased CV.

Curiously, the combination of atrial M-F coupling with diffuse fibrosis (diffusion coefficient reduction) resulted in slightly decreased AF duration in the 3D atria model, in contrast to other conditions associated with fibrosis. This may be due to the biphasic relationship between the ERP restitution curves with/without the M-F coupling (Chapter 3, Figure 19). The respective combination of diffuse fibrosis with M-F coupling using the ventricular fibroblast model resulted in a much longer duration of re-entry. This could be due to the reduction in wavelength associated with this model shown in Chapter 3. This is evidenced by a larger excitable gap (between a re-entering wave and the preceding one) seen in the case of coupling with ventricular fibroblasts (Figure 24E) as compared to that with atrial fibroblasts (Figure 24C). These results also point the sensitivity of 3D atrial behaviour to the choice of a fibroblast model. The atrial fibroblast model developed in this study, based on more comprehensive data is more representative of atrial electrophysiology.

In future studies with larger numbers of subjects, the expected outcome would be a typical rotor stabilisation in the border zone. This is primarily due to the reduction of conduction velocity in these regions and the stabilising effect on rotor dynamics.

### 4.4.3. Ionic remodelling

Another outstanding observation was related to ionic remodelling, which predictably produced stable re-entry due to the much shorter wavelength (see Figure 30). Although the duration of this simulation was longer (Table 6) it failed to break down and only produced stable rotors. This may indicate that ionic remodelling and fibrosis distribution have different roles in AF progression. Fibrosis

due to AF requires sustained AF episodes for several months before noticeable collagen deposition is observed. This suggests that fibrosis may have more impact in the later stages of AF progression.

### 4.4.4. Interstitial fibrosis

Increased anisotropy was investigated as a property of interstitial fibrosis. During SR simulations little difference was observed between different levels of anisotropy, aside from slight conduction slowing during fast pacing. This suggests that under normal conditions higher anisotropy may not have a substantial effect on the 3D atrial dynamics. This is in contrast to behaviours during fast pacing and resultant AF, where conduction block and wave breakdown is more prevalent in higher anisotropy conditions. This was the only condition where the 3D atria model produced a sustained re-entry and AF-like patterns. The latter were present as a single re-entrant wave followed by breakdown into multiple re-entrant wavelets. Overall, the 3D wave dynamics changes due to increased anisotropy were more significant than the effects of M-F coupling or wavelength reduction due to ionic remodelling. This may suggest that the structural effects of fibrosis, which develop later in AF progression, may play an important role in AF stabilisation rather than initiation.

### 4.4.5. Conclusions

In conclusion, the model showed that anisotropy linked with AF-induced interstitial fibrosis was the primary cause for wave breakdown, which best represents AF behaviour. Diffuse fibrosis resulting in reduced electrotonic coupling between atrial myocytes, as well as M-F coupling with atrial fibroblast, played a significant but less

prominent role than increase anisotropy. However, stabilisation of sustained activity in specific atrial locations, which is a theoretical mechanism of AF[133,134], was not observed in any of the multiple conditions considered in this chapter. Such a stabilisation has been increasingly linked with the presence of heterogeneous fibrosis distributions in the atria. In the next chapter, patient-specific areas of patchy fibrosis are mapped onto the atria model to investigate a possibility of rotor stabilisation in such areas.

# 5. Patient-specific fibrosis modelling

## 5.1. Introduction

Patchy, or compact fibrosis has long been suggested as a mechanism for arrhythmogenesis. Structural and functional tissue heterogeneities associated with fibrosis have generally been linked to arrhythmogenesis[135]. Furthermore, histological studies have shown fibrosis distributions to be non-uniform in the atria[136] and ventricles[137]. These distributions can be presented as large collagen deposits within the functional myocardium. In addition to impairing the myocardium contractility, fibrotic tissue is electrically unexcitable. Hence, interstitial depositions of fibrosis can slow down or block the propagation of electrical excitation waves, creating conditions for the generation and sustenance of re-entrant propagation. In ventricular tissue, heterogeneous non-functional myocardium caused by infarction has been shown to be directly pro-arrhythmogenic[50]. However, the effects of patchy fibrosis in the context of AF have not yet been studied in detail, which may be due to the difficulty of linking structural (e.g., via histology) fibrosis data and measured heterogeneous electrical activity.

Recently, atrial fibrosis has emerged as one of the most promising clinical markers for AF, which strongly correlates with improved treatment effectiness[138]. It has also been shown that atrial fibrosis is higher in AF patients compared to healthy subjects and correlates positively with AF recurrence[139] after ablation. Furthermore, direct ablation of fibrotic areas identified from late-gadolinium enhanced MRI[8,140] or electro-anatomical mapping[9] can significantly improve the therapy success rates.

This suggests that patient-specific distributions of atrial fibrosis may directly or indirectly determine the dynamics of electrical drivers sustaining AF. Better knowledge of the location of fibrotic areas has a potential to increase the knowledge of AF genesis and provide important assistance for catheter ablation therapy.

This chapter explores missing links between patchy fibrosis and AF using patient-specific models of the 3D human atria. It also aims to highlight potential sensitivity to methodology used during the quantification of atrial fibrosis. For the duration of this work, 'patchy' fibrosis will refer to regions of inhomogeneous fibrosis, which range from low-level diffuse fibrosis to dense fibrosis (also known as compact, scar or patchy).

### 5.1.1. Patchy fibrosis

Atrial fibrosis increases with age and disease, due to structural remodelling of the atrial tissue. The mechanism can be either myocardial cell death, increased deposition of collagen or reduction in collagen degradation. As the condition persists, collagen deposits become larger and more concentrated and can develop into dense patchy fibrosis.

The areas of patchy fibrosis have been associated with AF arrythmogenisis[52] and have been linked specifically to complex fractionated atrial electrograms (CFAE)[141,49]. CFAEs recorded in AF patients are characteristic of high frequency activation and slow conduction associated with AF. CFAEs may reflect the complexity of the tissue substrate for persistent AF[142]. Thus, patchy fibrosis has been linked with slower and more continuous CFAEs[141]; clinically such CFAEs are

commonly used to predict favourable ablation sites in AF patients[143,144]. However, mechanistic links between highly variable electrogram morphologies and outcomes of CFAE-guided ablation procedures are unclear[142,143].

### 5.1.2. Border zones

The effects of heterogeneous border zones (BZ) linked with compact fibrosis in the ventricles are well documented[137]. Structural and electric remodelling in the ventricular infarct BZ after myocardial infarction has been shown to give rise to slow conduction, unidirectional block and re-entry. Remodelling factors include isolated strands of functional myocardium surrounded by dense fibrosis that provide conduction pathways within the infarct BZ[50] and decreased lateral connections between myocytes due to altered gap junction distributions[145]. Both these factors reduce conduction velocity during infarct healing. Image-based computer modelling has provided a powerful tool for investigating the mechanistic links between such structural anisotropy and electric activity in ventricular infarct BZ[146].

Recent studies[141] have observed that areas adjacent to dense fibrosis in the atria have also shown high levels of arrhythmogenic activity. These myocardial areas, whilst still fibrotic, are not damaged sufficiently to fully inhibit wave propagation and have a high correlation to CFAEs[141]. Such regions commonly surround dense fibrotic areas which have been shown to have low levels of electrical activity. A cause for this may be that they allow for re-entrant behaviour within the borders zone creating a circus movement around the dense fibrosis. These regions, characterised by both structural remodelling and abnormal electrical activity, are

similar to ventricular infarct BZ. Therefore, such regions of patchy fibrosis that have dense-to-diffuse fibrosis gradients are increasingly being referred to as "border zones" and linked with arrhythmogenic effects in the atria.

### 5.1.3. Imaging of fibrosis

Fibrosis is difficult to image using conventional clinical methods due to the limited resolution of imaging techniques approved for patients. Animal studies[147–150] use ex-vivo histological dissection followed by collagen staining to quantify fibrosis. Some human studies have utilised post-mortem hearts[151] or biopsy data[136] from patients to histologically compare atrial regions with varied electrical activity. These methods are largely unsuitable for patients due to the invasiveness of the procedure. Furthermore, they are limited in coverage of the atria and only allow for small windows of observation on the atrial wall.

While fibrosis can be clearly detected using histological staining, in-vivo imaging has inferior resolution, but is non-invasive and can cover the whole atria. An MRI-based method, LGE MRI, was originally developed to image myocardial infarction and focal scar but has emerged in the past 5 years as a means to quantify atrial fibrosis in-vivo. LGE relies on the injection of a Gd-based intravenous contrast agent, which alters the MR properties of the tissue where it is absorbed, reducing the tissue's longitudinal relaxation time constant, T1. As Gd cannot enter healthy cells and the extracellular volume (ECV) is increased in fibrotic areas, Gd compounds tend to accumulate in regions where there is fibrosis. This allows the identification of fibrotic areas as atrial regions are brighter than healthy myocardial tissue in T1-weighted MR images. The use of LGE MRI to detect atrial fibrosis in AF has been

pioneered by a the CARMA group in the University of Utah[152], and applied to assist in ablation procedures[8,139].

LGE MRI gives the best clinical option for atrial wall composition analysis due to the low invasiveness and it is routinely performed on patients prior to the ablation procedure, to provide navigation images. The technique has been criticised, and it is notoriously difficult to get reproducible results on fibrosis segmentation from LGE MR images.[153] The method is also limited to use on pre-ablation patients,[140] as the intensity of the ablation lesions in the image can overwhelm any atrial fibrosis due to disease. However this method offers us the only opportunity to study spatial distributions of fibrosis in the atria as well as easy access to patient data due to procedural non-invasiveness.

## 5.2. Methods

The following section outlines the changes made to the 3D atrial model (Chapter 4) to incorporate patient-specific distributions of patchy fibrosis and simulate its effects. It also includes the image processing pipeline that converts patient MRI data to useable datasets for the model.

### 5.2.1. Late gadolinium enhanced MRI

The images used in this study were obtained from 3 permanent AF patients recommended for routine, first time pre-ablation imaging. The data was randomised to ensure patient privacy. The scanner used was a Philips 3T MRI scanner and the images were obtained at 1.4x1.4x4mm$^3$ resolution and saved in DICOM format. Two MRI modalities were used; early Gd angiographic imaging (Figure 31D) and LGE MRI (Figure 31A-C). The angiography images were used for an

improved segmentation of LGE MRI data (see below). These were taken in the same cardiac phase.

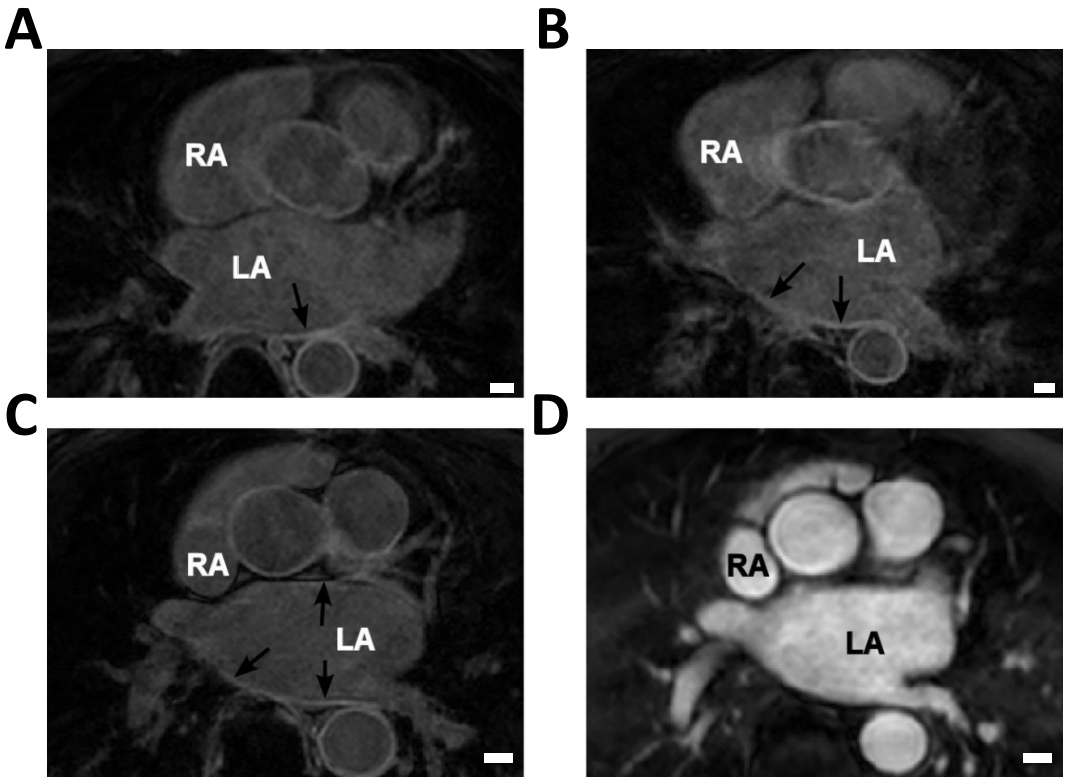


***Figure 31***. *Patient-specific LGE MRI datasets. A-C show late Gd enhanced MRI slices through the atria (two atria are labelled in white) with areas of high intensity linked to fibrosis indicated by the black arrows. D shows a Gd angiographic image with high-intensity blood volume, which is used in the segmentation of the endocardial surface. C and D are from the same patient scan in the same coronal slice. The images were 3D MR scans acquired on a 1.5T MR scanner. The white scale bar is 10mm.*

### 5.2.2. Image Processing Pipeline

Initially, 3D distributions of atrial fibrosis were reconstructed using manual region based segmentation, to be later registered with the Visible Human atrial dataset. The accuracy of this method was limited and time consuming, as both location and size of the fibrotic regions are subject to operator error.

For the fibrosis segmentation method to be more repeatable, an image processing pipeline was developed to reconstruct and register the LGE data with the 3D atria (Figure 32). The Pipeline utilises fibrosis segmentation tools developed by the CARMA group at the University of Utah as plugins to 3D Slicer$^{TM}$. This enables two different forms of fibrosis segmentation, either a binary dense patchy fibrosis or as continuous fibrosis as a function of image intensity. These methods are compared during this chapter.

The extraction of fibrosis data from MR images requires thresholding of the intensity of the atrial wall. Obtaining the atrial wall in MRI data is non-trivial[70] and detailed segmentation can only be done manually due to low resolution and SNR. This process is extremely time consuming and may still provide discrepancies between segmenters. This will be further discussed in the following chapter. Fortunately, the LGE MR images are acquired in the same session and at the same cardiac phase to an angiography image that is used as a navigation image for planning ablation procedures. The angiographic MRI images (Figure 31D) the blood pool which has a high intensity due to the contrast agent (Gd) and allows for accurate semi-automatic segmentation of the endocardial surface. This is achieved using a region growing algorithm within ITK-snap, which utilises seed points that iteratively dilate. The growth is limited by image intensity gradients. The segmented endocardial surface can then be dilated to provide an epicardial surface. In some cases it required manual rectification in highly convoluted areas. The dilation is usually between 3-5mm, which corresponds to the variable atrial wall thickness.

The endocardial volume is then subtracted from the dilated epicardial volume creating a 3D wall mask.[70]

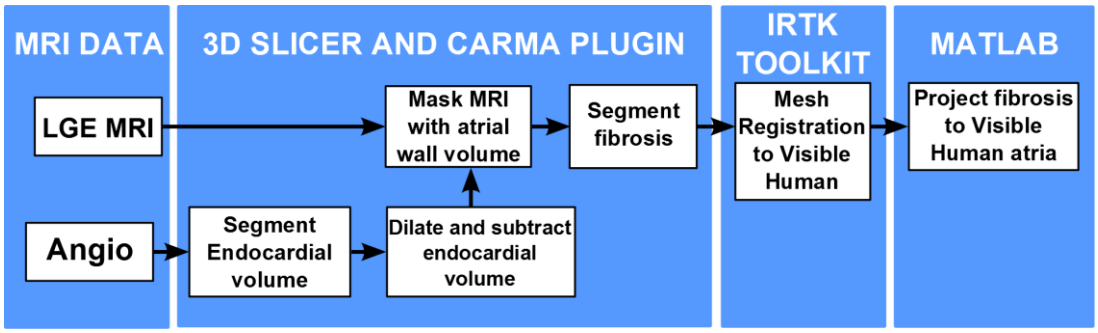


***Figure 32**. Diagram of the image processing pipeline used to obtain 3D distributions of atrial fibrosis and integrated them into 3D atrial models. It is broken down into blocks (in blue) showing the programs used.*

Utilising tools developed by the CARMA group, available as a 3D Slicer plugin (http://www.slicer.org/slicerWiki/index.php/Documentation/4.5/Modules/ScarVisualization), provides 2 different methods for fibrosis segmentation. The first, named "*automatic scar segmentation*", uses a K-means clustering algorithm. This produces a binary fibrosis model in the masked region, identifying the densest fibrosis areas. The second method collects the MR intensity data from the masked image applying no threshold or segmentation. Both methods project the data onto a surface mesh of the endocardium.

This 3D atrial mesh is then registered to a respective 3D mesh of the Visible Human Female atria using the IRTK-toolkit (https://biomedia.doc.ic.ac.uk/software/irtk/) using a non-linear deformation. The registered 3D atrial mesh is projected onto the Visible Human atrial dataset using a "nearest neighbour" algorithm. Fibrosis datasets obtained using the 'threshold' tool are segmented by LGE MRI threshold,

with the threshold values being defined on the range of the image intensity in the masked image.

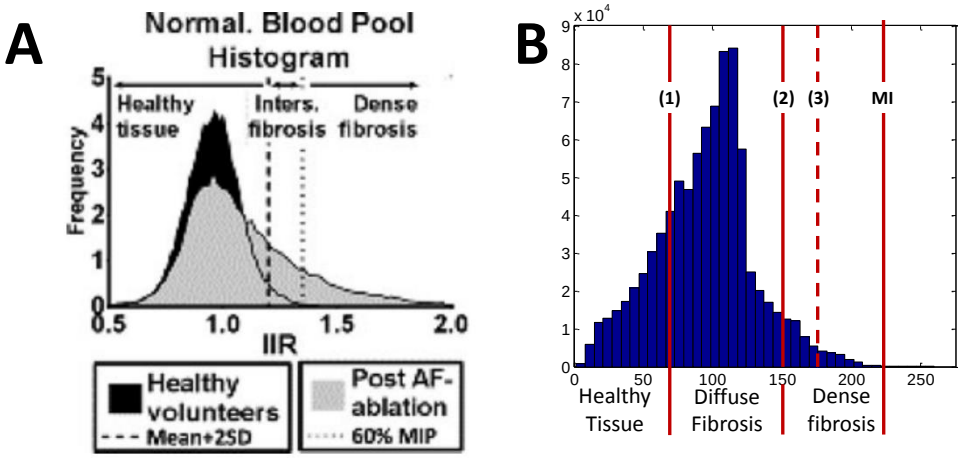


***Figure 33**. LGE MRI histograms. A shows a comparison between healthy volunteers (black shading) and fibrotic (grey shading) tissue, from Benito et al.,[154] note that this includes the blood pool. The fibrosis histogram clearly shows the skew associated with fibrosis. B shows a masked histogram, i.e. only the intensity of the voxels within the masked atrial wall region. The red lines show a range for fibrosis level segmentation. (1) is the lower limit of the diffuse fibrosis (levels 1-3) and 2 shows the lower limit for the dense fibrosis regions (levels 4 and 5). The dashed red line (3) shows the lower limit of the densest (level 5) fibrosis region. The red line denoted MI shows the maximum intensity from which the fibrosis regions were calculated.*

It has been theorised that the myocardium and fibrosis in the atria could produce distinct MR intensity peaks. In reality there is significant overlap and they are indistinguishable in atrial MRI. Also there is a large variation in the intensity histograms between scans and therefore tissue cannot be explicitly quantified by intensity value. It is due to this that the range of intensity threshold values was determined uniquely for each patient. To estimate the fibrosis peak, an encompassing range of intensity values must be found. This was calculated individually for each patient using the maximum intensity (MI) as the upper limit (Figure 33B). The latter was the last significant intensity value, which was the last

histogram bin with a population greater than 1% of the maximum population (in a histogram with 50 bins over a range of 255).

This enabled the removal of outliers, as some of the intensity histograms had a large range of high intensity values with very low voxel populations (<1%). The range was divided into 7, with the lowest 2/7th being allocated to healthy tissue and each fibrosis levels 1-5 as the following 1/7th of the range (moving towards the higher values). Due to the reduced populations in the densest fibrosis level (5), the last 1/7th of the range was expanded by 20% (moving towards the lower values). This provided the significant regions of dense fibrosis that can be observed in the MRI images.

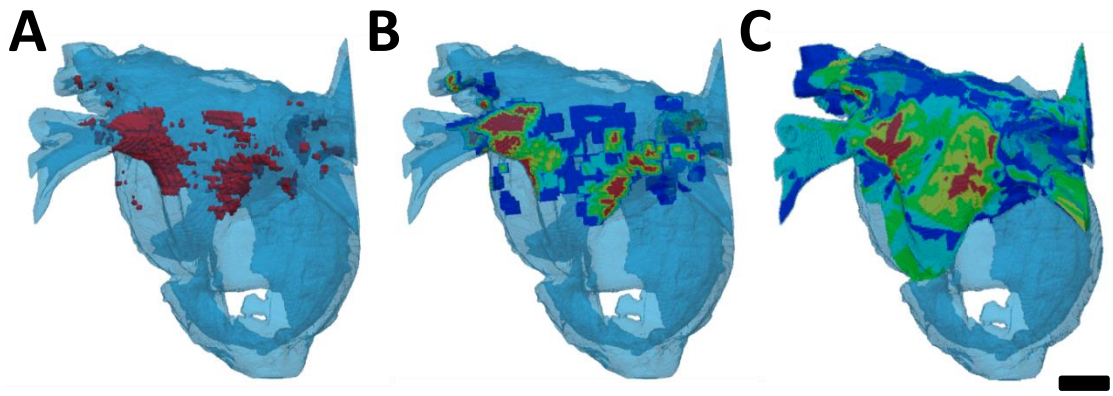


***Figure 34**. Reconstructed left atrium fibrosis distributions mapped onto the 3D human atrial model. Three methods are applied to the same patient dataset. A shows a fibrosis distribution created from 2D projection of the reconstructed 3D mesh to the Visible Female 3D atrial volume. B shows a synthetic fibrosis gradient generated from the fibrosis distribution shown in A. C shows a full patient-specific fibrosis distribution with the gradient generated from thresholding the LGE MRI intensity.*

To investigate the role of threshold variation, two alternative segmentations were created for each LGE MRI dataset, one with a high and another with a low threshold. This was created by shifting (10 units of LGE MRI intensity) the threshold (Figure 37).

The segmented fibrosis regions were considered to be transmurally uniform in the 3D atrial model. The developed image processing pipeline has the potential to accommodate non-uniform fibrosis throughout the wall, but this was not implemented due to the small thickness and the coarse image resolution. However, should the resolution limitations be improved in future imaging modalities, then the model could be applied with more accuracy.

### 5.2.3. Fibrosis border zones

Simulations of the border zones that reflect dense-to-diffuse fibrosis gradients were carried out in 2D atrial tissue (Figure 38) and in 3D atria (Figure 33C). In 2D tissue, 5 concentric contours of increasingly mild fibrosis were created around a central dense fibrotic region. The contour number was then used as an index for applying fibrotic properties (see below).

In the 3D atria 2 methods of BZ creation were applied. A synthetic BZ composed of 5 concentric areas each 1-2 voxels thick was created, surrounding the binary fibrosis segmentation. These were created with a moving 3x3x3 ball filter for each level (Figure 33B). For each voxel of fibrosis, the surrounding voxels in the filter (that were not already occupied with fibrosis) were denoted as the next fibrosis level. To change the thickness of the levels a larger filter is applied.

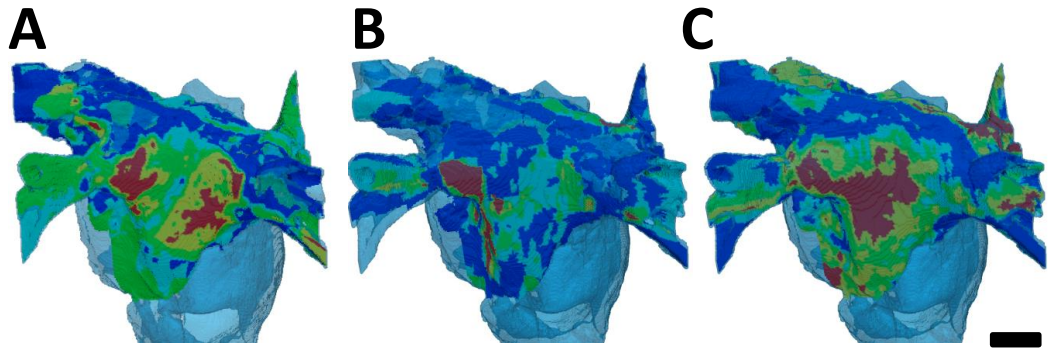


***Figure 35***. *Reconstruction of fibrosis by intensity threshold method from 3 patients. Variation in distribution can clearly be seen between patients A-C. A and C show cases with lower thresholds (see Figure 37) and B shows a case with a high level threshold.*

The second method is reliant on MRI image intensity to create the 5 fibrosis levels (Figure 34C). In most cases these had good concentricity around the densest central regions, but were overall, considerably less uniformly than the synthetic BZ.

### 5.2.4. Computational 3D atria model

The 3D atria model used was discussed in Chapter.4. It integrates human atrial geometry, fibre orientation, region-specific electrophysiology, ionic remodelling and a novel electrophysiologically detailed model for an atrial fibroblast and M-F coupling. In this section, the model included 5 distinctive fibrosis levels, indexed 1-5 depending on the distance from the central dense fibrotic region (Figure 34B) or LGE MRI intensity (Figure 34C). Index 0 represents no fibrosis, and regions with indices 1-5 are modelled as increasingly severe diffuse-to-dense fibrosis: specifically, as indices 0-5 corresponded to progressively increasing M-F coupling (0-5 fibroblasts per myocyte) and decreasing diffusive coupling between myocytes (100%-20% of the diffusion coefficients).

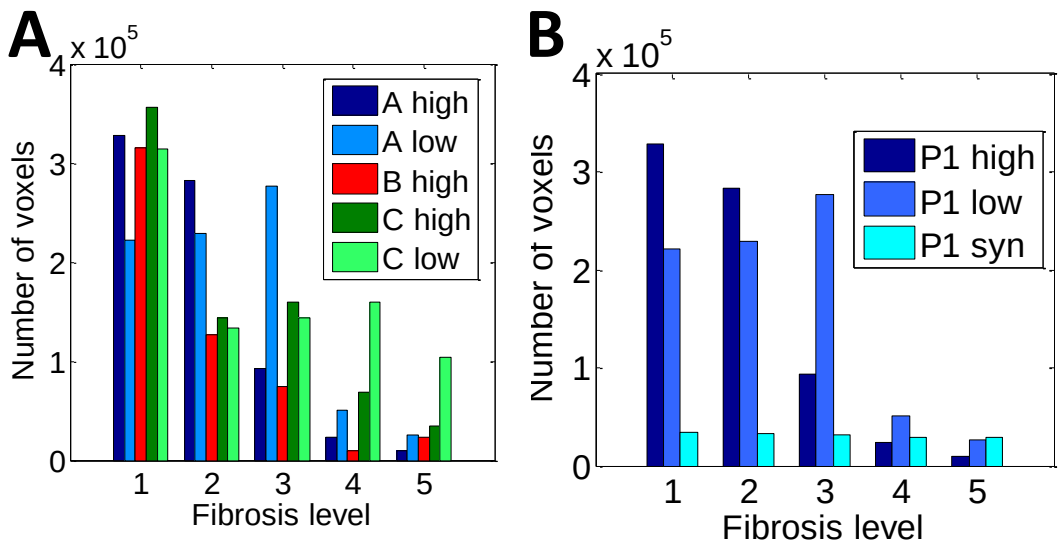


***Figure 36**. Fibrosis distributions in different datasets. A shows differences in the fibrosis distribution between 3 patients and between varying intensity thresholds, and B shows the variation between segmentation techniques in one patient. The suffixes high and low refer to the relative threshold and syn to the synthetic BZ.*

The conditions used for the whole 3D atria in all simulations were high anisotropy and ionic remodelling (Chapter 4). AF was initiated by fast LAA pacing in each of 3 "persistent AF" atrial models with patient-specific distributions of fibrosis.

## 5.3. Results

### 5.3.1 Left atrial fibrosis distributions

The segmentations of LGE MR Images yielded different fibrosis distributions in 3 AF patients. The fibrosis distributions observed varied in the extent and severity, as can be seen in Figure 36 and Figure 37. All datasets showed areas of more severe, dense fibrosis (based on increased LGE MRI intensity) in the posterior LA (Figure 35), which is a common ablation target.

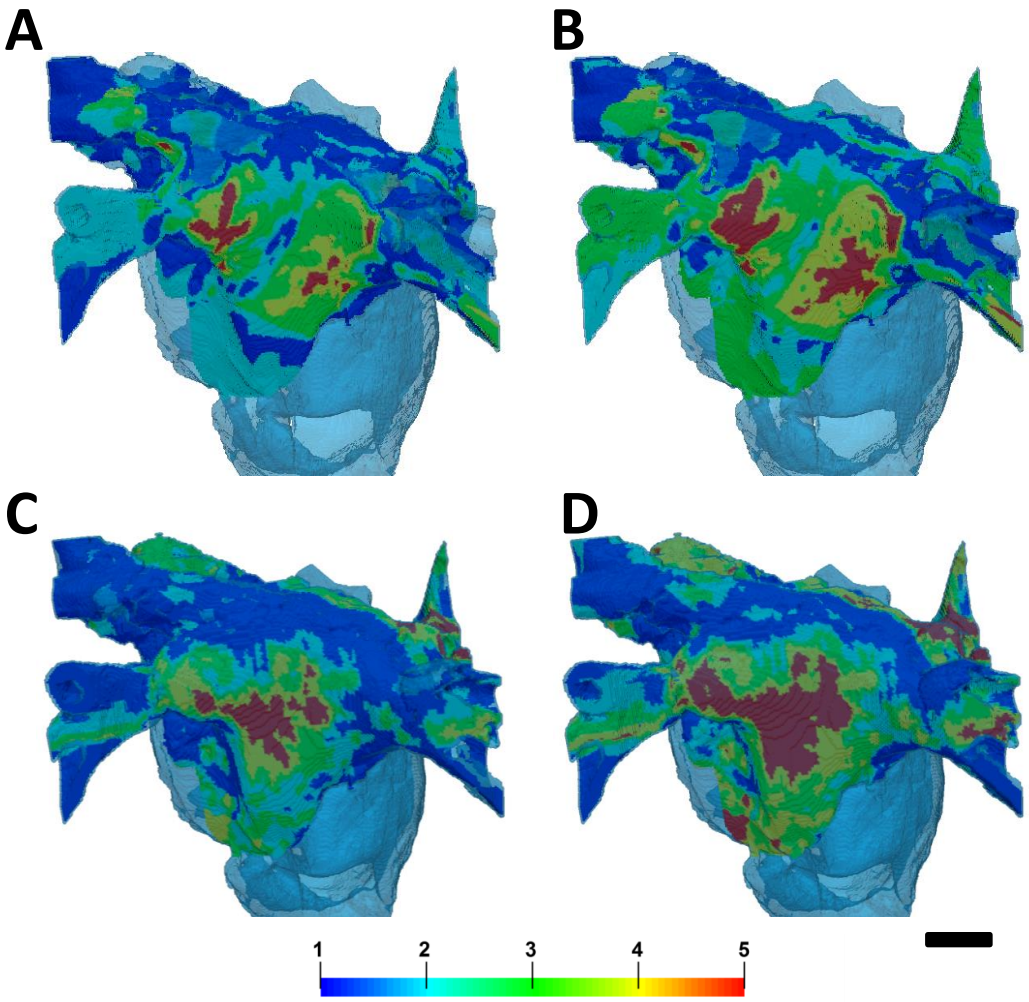


***Figure 37***. *Atrial fibrosis distributions of 2 patients based on LGE MRI datasets with variation of the intensity threshold. The levels 1-5 describe fibrosis severity based on LGE MRI intensity. A and C show the fibrosis distributions for high threshold segmentation. B and D show the low threshold segmentation datasets.*

The relative quantised distributions of fibrosis in the thresholded datasets showed a higher distribution in the lower fibrosis levels (Figure 36). Significantly lower amounts of fibrosis were observed in the higher levels (4-5) despite a shifted bias for level 5 fibrosis. In these datasets good connectivity of fibrotic regions was observed, (i.e. no isolated small islets fibrosis) and the fibrosis levels are presented concentrically (Figure 35). In contrast, the synthetic boundary showed a more

even distribution of fibrosis between the fibrosis levels and overall a much lower intensity.

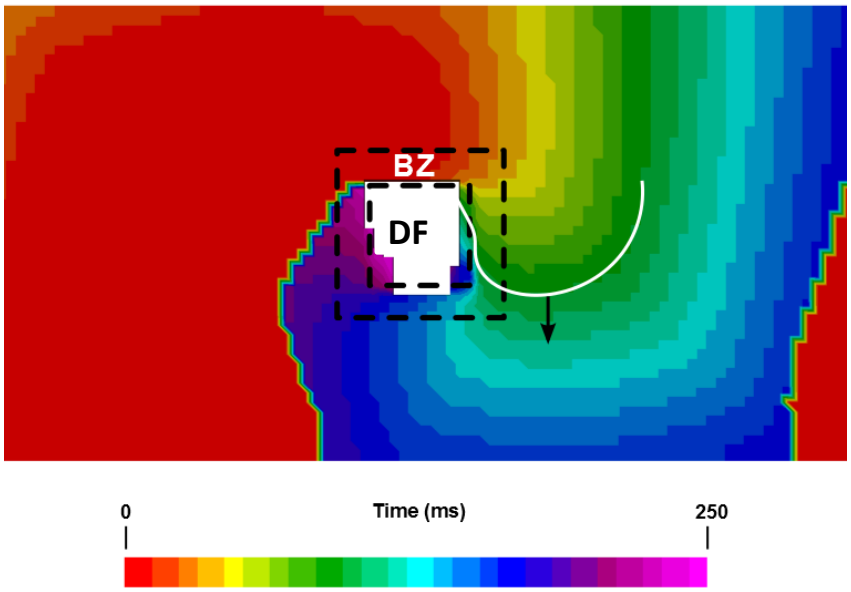


***Figure 38**. 2D simulation of atrial tissue with patchy fibrosis border zone. Activation times during one period of a re-entrant wave rotation around a fibrotic region are colour-coded using a rainbow palette. The dashed black lines show the inner and outer limits of the border-zone. The area labelled DF is dense fibrosis and signifies the area where fibrotic conditions are maximised with an 80% reduction in diffusion coefficient and 5 coupled fibroblasts. The white area shows inactivated tissue within the patchy fibrosis region. The white line indicate a wavefront at 100ms the black arrow indicates wave propagation direction.*

### 5.3.2 Simulations of fibrotic atria tissue

In 2D tissue simulations, wave pinning to the patchy fibrosis border-zone was observed. In less than 500ms after its initiation by cross field protocol, the re-entrant spiral wave became pinned to the region of fibrosis within atrial tissue. The dense-to-patchy fibrosis gradient enabled slow conduction around the border (where the diffusive coupling was reduced), resulting in persistent re-entry around the region. During the spiral wave re-entry, the dense fibrotic core of the fibrotic

region was incompletely activated (Figure 38). This is due to slowing down of the wave conduction in deeper regions of the fibrotic region, with CV effectively dropping to zero in regions indexed 4-5. Without re-entry, the whole tissue including the dense fibrosis region was activated by a propagating plane wave.

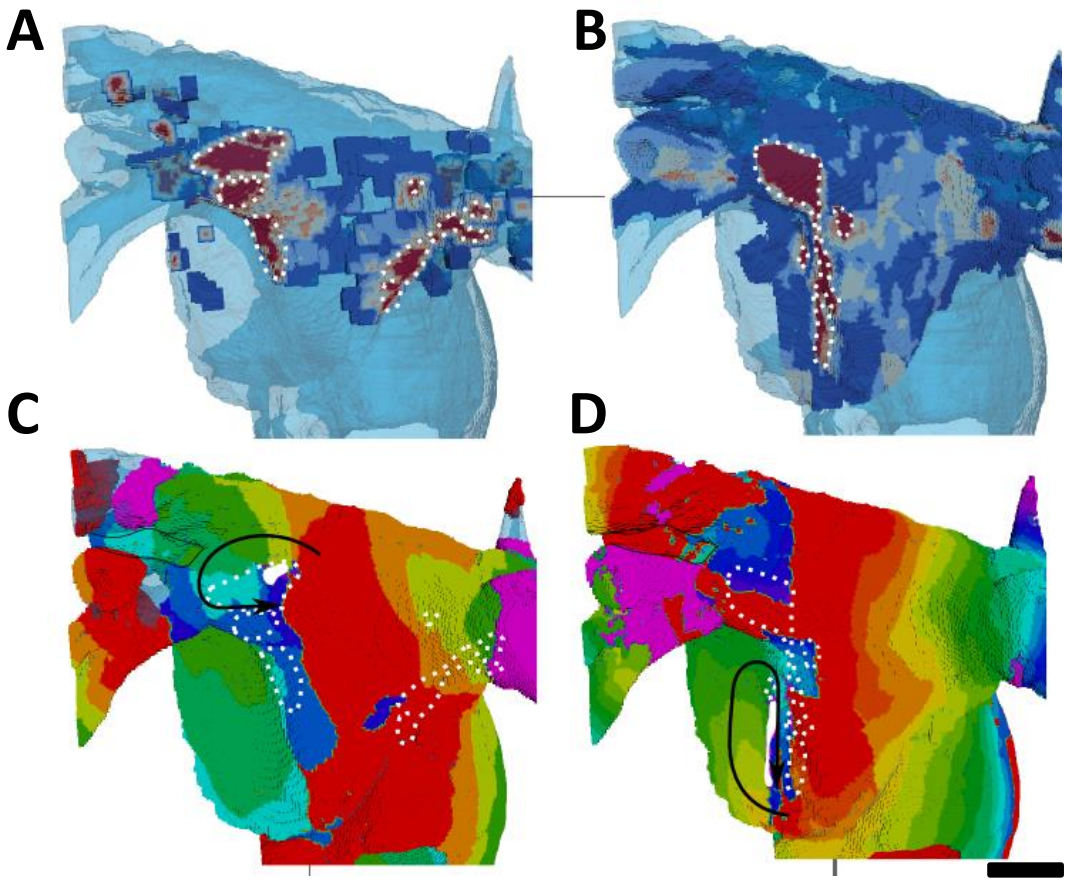


***Figure 39***. *Stabilization of rotors in patchy fibrosis regions. A and B show two different patient-specific fibrosis distributions, and C and D show the respective single rotor period activation maps. The activation maps illustrate the variation of rotor pinning specific to the distributions of fibrosis. Wave propagation direction is denoted by the black arrow, the core of the rotor is indicated by the solid white shape and central dense fibrosis regions are indicated by the dotted white lines. C shows a rotor pinned directly to a dense fibrotic region. D shows a rotor with the core adjacent to a dense fibrotic region, but rotating within a border zone.*

In 3D atrial model simulations, short duration pinning to the fibrotic region was seen in most cases, both for different patients and for different methods of generation patient-specific fibrosis (Figures 39-41). Permanent rotor stabilisation in the border zone was seen in 2 cases, where rotor was pinned until the end of simulation. One of these simulations produced rotor movement directly around an area of dense fibrosis and another within an adjacent border zone of less severe patchy fibrosis (Figure 39). In both case, the rotor core was within regions of broadly defined patchy fibrosis, characterised by severity indices between 3 and 5. Spatio-temporal dynamics of these rotors is illustrated in Figure 40.

In patient-specific 3D atrial model simulations with variation of LGE MRI intensity threshold, different behaviours were observed (Figure 41). In simulations with the higher thresholds (lower fibrosis level) no stable rotor pinning was observed, with only short lived (less than 1 second) meandering re-entry in the LA fibrotic regions in two patients (Figure 41A and B).

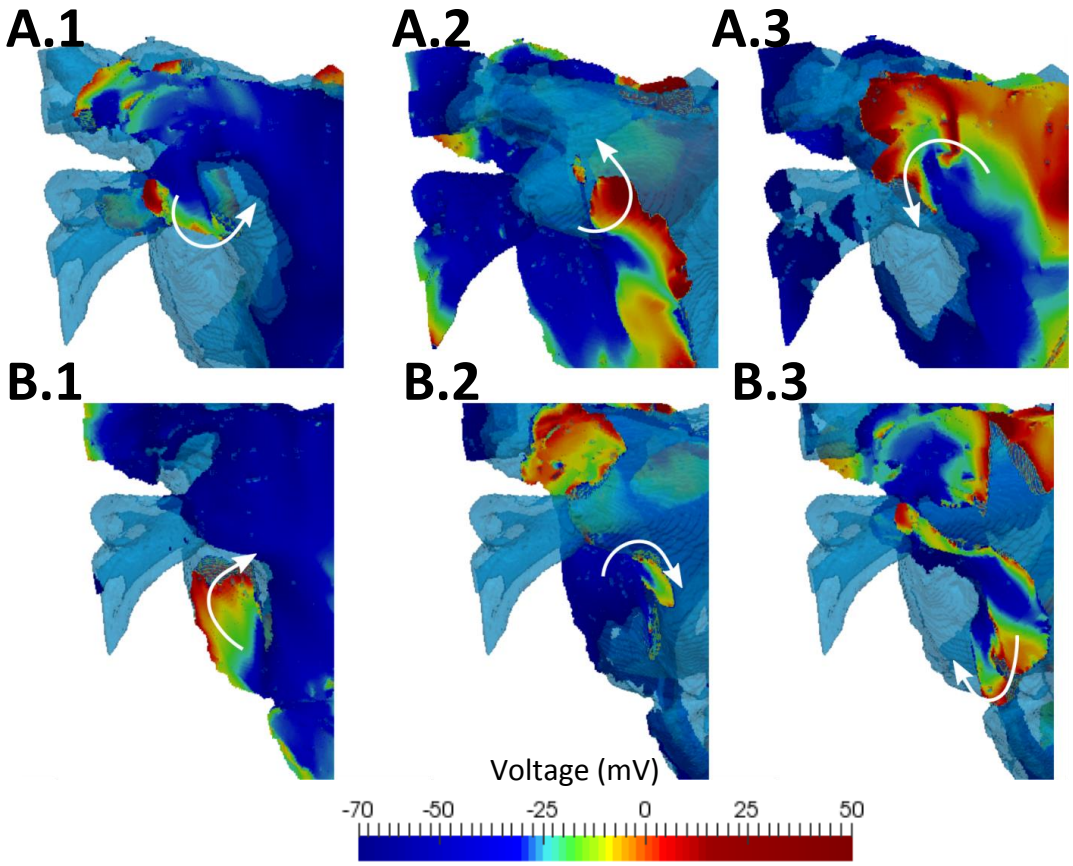


***Figure 40**. Spatio-temporal dynamics of rotors pinned to fibrotic regions. A.1-A.3 show the rotor progression with the fibrosis distribution shown in Figure 39.A and B.1-B.3 show the rotor progression with the fibrosis distribution, shown in Figure 39.B. Snapshots showing the voltage distribution in the posterior LA are 30ms apart, and the rotor direction is indicated with the white arrows.*

Simulations of the same two patient-specific atrial models with the lower threshold (higher fibrosis level) showed severe wave breakdown, with multiple re-entrant wavelets in the left and to a lesser extent the right atria. The wavelets in the fibrotic region created complex interactions that prevented a single mother rotor to form (Figure 41B and D). The complex electrical activity in both 3D patient-specific atria was characteristic of AF and was sustained to the end of simulation (10 seconds).

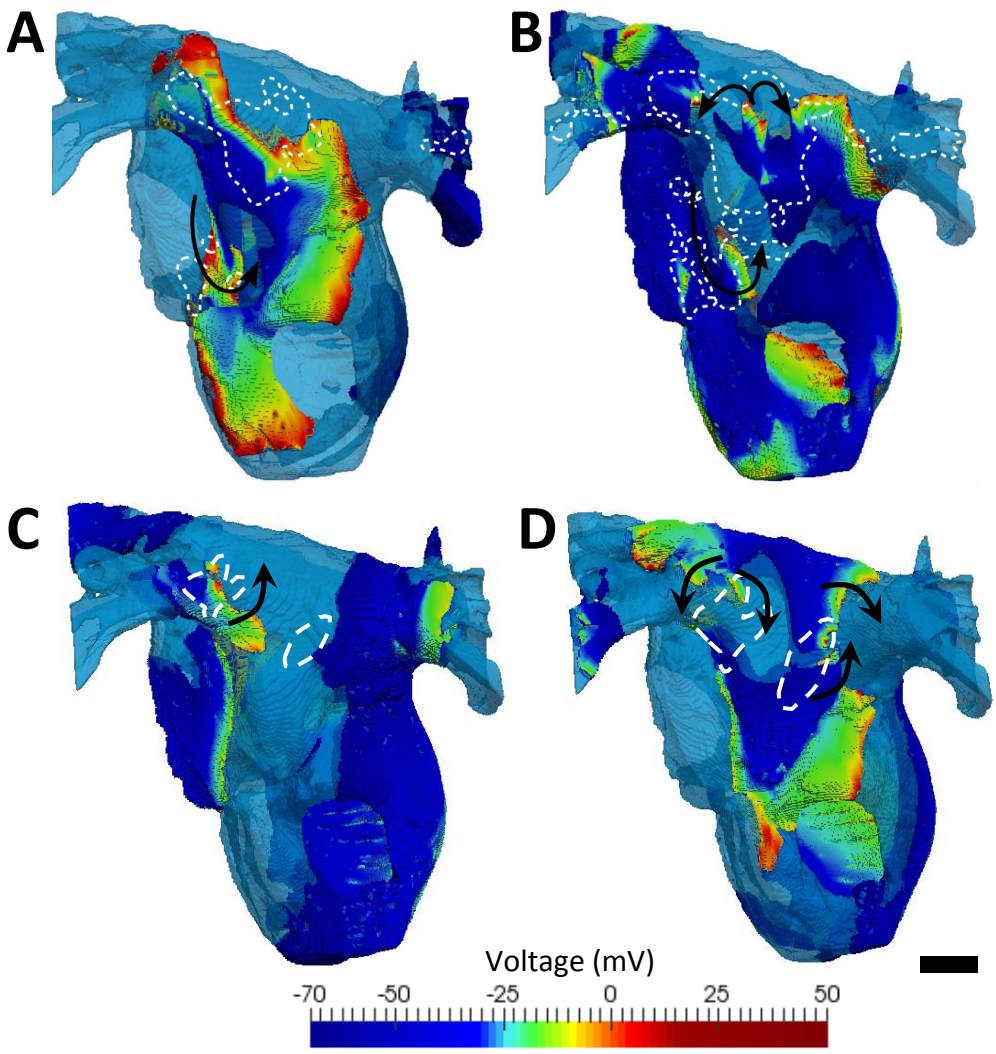


***Figure 41***. *Snapshots of re-entry in 3D atria with fibrosis distributions based on high and low thresholded LGE MRI intensity datasets. A and C show two patient cases with a high threshold (lower amount of fibrosis) and B and D show the respective cases with a low threshold (higher fibrosis). The rows delineate different patients (A,B and C,D). In the high threshold cases (A and C), only a short lived rotor (indicated) was present in the LA. In the high threshold cases (B and D), multiple re-entrant waves are present in the LA fibrotic regions. Black arrows show directions of wave propagation, white dashed lines indicate level 5 fibrosis.*

## 5.4. Discussion

The 3D atrial simulations performed for this chapter indicate the importance of using patient-specific LGE MRI data to study AF. They also allude to the importance

of fibrosis in arrhythmogenesis due to the unique wave interactions for different fibrotic distributions. The developed image processing pipeline could also be useful for image-guided clinical interventions that are increasingly reliant on patient-specific knowledge about fibrosis patterns. In future, linking patient fibrosis distributions and arrhythmogenesis could lead to bespoke and more accurate ablation techniques, with reduced procedure time and lower AF recurrence rates.

### 5.4.1. Fibrosis segmentation

Although the threshold segmentation method requires further validation, this work aims to investigate the effect of substantial fibrosis regions, which can be observed in MRI images. This method was based around the theory that the LGE MRI intensity histogram right skew was a quantification of fibrosis. This has been recently quantified with post ablation scar[154].

The pipeline enabled the creation of unique non-binary fibrosis distributions for each patient. The reconstructed patient datasets showed increased fibrosis distribution on the LA posterior wall. This region is well known for its association with AF ablation, and may be statistically prone to fibrotic infiltration. However, it may also be due to partial volume averaging from the spinal connective tissues or descending aorta which have a high LGE MRI intensity (see Figure 31A and D).

The lower extent of fibrosis on the roof and floor of the LA may be due to the lower Z axis resolution of the MRI scan. Regardless of the limitations of the imaging method, LGE MRI intensity has been strongly linked to fibrosis, and the reconstructed fibrosis distributions agree with existing knowledge of fibrosis

distributions. Moreover, results of this work show the patient-specific variation of such distributions and their effects on the variable wave dynamics underlying AF.

Two different methods of fibrosis segmentation were used in this work, (i) binary dense fibrosis segmentation with a synthetic BZ and (ii) thresholded LGE MRI intensity. Although the former relies on a more complex segmentation technique, there is a good spacial correlation between the locations of the dense fibrosis segmentations in cases (i) and (ii) (Figure 34). However, the shape and extent of the BZs of patchy fibrosis are significantly different. This may be due to the simplicity of the thresholding method or due to the UTAH segmentation method being applied slice by slice along the Z axis. Which account for the inherent variation of contrast in MRI slices. However the concentricity and connectivity of the fibrosis threshold levels segmentation, suggest that the fibrosis is less susceptible to contrast variation between layers.

### 5.4.2. Simulations of patient specific fibrosis

The 3D atrial model simulations showed a wide range of electrophysiological behaviours with different fibrosis datasets and distributions. In the simplest case, the fibrosis was originally mapped onto the 3D atria as a binary region of dense fibrosis (Figure 34A). Initial simulations where this region was set as either non-conductive or with severely reduced conductivity did not produce any arrhythmogenic effects, with waves simply passing around the region. Only when a fibrotic BZ was implemented, rotor initiation (and in some cases, stabilisation) occurred.

Stabilised rotor formation was observed in 2 simulations; one for a fibrosis distribution with synthetic BZ and one with LGE MRI intensity threshold. The former produced a larger circus movement around a dense fibrosis region (Figure 39 C) and the latter produced a smaller rotor adjacent to a dense region (Figure 39 D). In both these cases the simulation had high gradients of fibrosis density, which may be a mechanism for rotor stabilisation.

In this research the simulations also show that patient specific fibrosis distributions can induce wave breakdown (Figure 41B and D) which is symptomatic of AF. This was only observed in simulation of high levels of fibrosis (obtained with a low LGE MRI intensity threshold) and resulted in permanent AF for the duration of the simulation (10s). Smaller re-entrant wavelets were observed in these simulations moving chaotically throughout the fibrotic region. Contrarily, in simulations of lower levels of fibrosis in the same patient (obtained by using a higher LGE MRI intensity threshold) produced very short duration re-entry that was neither stable nor resulted in wave breakdown. Note that the cumulative amount of fibrosis was not very different between the high and low thresholds (Figure 36), rather, it was distributed more in fibrosis levels 3-5 with a lower threshold. The simulations show that the wave dynamics underlying AF should be determined by the amount of severe dense fibrosis (levels 3-5), rather than total size of fibrotic areas.

### 5.4.3. Challenges of fibrosis imaging in the atria

The difference between the high and low levels of fibrosis shows that the developed image processing and modelling pipeline is sensitive to the choice of parameters (such as LGE MRI intensity threshold) and can yield very different

results. Whilst there is little quantification available for LGE MRI intensity and amount of fibrosis from patients, the LGE MRI intensity should indicate higher areas of fibrosis[136] in comparison to the rest of the tissue. The LGE MR images may also suffer from partial volume averaging, in which neighbouring tissues influence the wall mask because of the coarse resolution of the image. This is particularly prevalent in regions where the distance between the atrium and the adjacent tissues is small or when adjacent tissues are particularly high intensity. For example descending aorta or spine.

### 5.4.4. Conclusions

It is clear from this work that inhomogeneous fibrosis distributions in the atria significantly affect the propagation of atrial waves in complex ways that are difficult to predict. It has been shown that a wide range of re-entrant behaviour between different patient specific distributions, from wavefront disruption and re-entry to multiple wavelet formation. The general trend was for waves to propagate closer to the inner denser areas of the patchy fibrosis region, reminiscent of electrical behaviour seen around the infarct border zones. However, the association of re-entrant waves with the patchy fibrosis border zones in 3D atrial simulations was not absolute, indicating a potential role of other factors that can affect re-entrant waves. Of one such factors, the atrial wall thickness, is studied in the next chapter.

# 6. Role of atrial wall thickness

## 6.1. Introduction

As discussed in previous chapters AF dynamics are highly variable between patients. This work has explored patient specificity in terms of disease state, i.e. fibrosis level, but for a more representative study, variation of other factors of atrial structure must be considered. It is clear from anatomical studies that the atrial wall structure is highly heterogeneous and that intra-patient and intra-regional structural differences have distinct effects on the electrophysiological and mechanical function of the heart. Moreover, volumetric reconstructions of the atrial wall can be applied as the mask for fibrosis reconstructions, and hence greatly improve accuracy of the latter. Knowledge of the atrial wall variation from region to region (e.g., thicker LA to thinner PV) may provide a more personalised approach to catheter ablation in different patients and in different atrial regions (see below). However, the extent of knowledge of atrial wall thickness is sparse and is subject to large variation (Table 7). Thus, gaining insight into the role of atrial wall thickness and the extent of its variation in the atria are both important for better understanding AF and its treatment.

### 6.1.1. Atrial wall thickness effects on ablation

Ablation therapy is based on creating a functional block in the tissue by creating a non-conductive lesion. The lesion must transmurally penetrate the myocardium for conduction block to occur. Ablation therapy sufferers from high AF recurrence rates. This may be due to insufficient lesion penetration, preventing full isolation of arrhythmogenic regions. If the ablation energy is insufficient, inflammation at lesion

sites may be also responsible for temporary “false positive” isolation, as the tissue may be functional repaired. Severe complications can occur, if excessive energy is applied during ablation, which include puncture[155], PV stenosis[156], tamponade, thrombosis or oesophageal ulceration[157]. The operator relies on estimates of energy required and success is measured by functional isolation, which may be a false positive. Further research is required to assess about the atrial wall thickness, whether that is patient specific or statistical, i.e. based upon patient categorisation.

### 6.1.2. Wall thickness effects on electrophysiology

Wall thickness also has a significant effect on atrial electrophysiology (as discussed in chapter 4). It is worth noting that these specific effects are related to structural changes in wall thickness rather than its dynamic changes due to the contraction. The latter does not change the electrotonic distance measured in space constants. Note also that the wall thickness is referred to in mm, rather than space constants. It has been hypothesised as a potential mechanism for arrhythmogenesis, with links being found between thickness gradients and stabilisation of rotors[40,158]. These parameters more thoroughly discussed in Chapter 4 and are based upon sink-source relationships, where current is divided in positive thickness gradients. This has been shown recently by in theoretical studies of simple tissue slabs, where rotors show a tendency to move along high thickness gradient areas[158]. However, these studies utilised simplistic tissue geometries and cell electrophysiology models, and have not considered realistic atrial shape and thickness variations. In studies with realistic, volumetric atrial geometries, patient specific wall thickness gradients are often overlooked. Recent models are moving towards a computationally efficient, but greatly simplified bilayer approach[159] which does not

consider the atrial wall to be a continuum. However, patient studies provide increasing evidence for relationship of atrial wall thickness with CFAEs and therefore drivers for AF[160,161].

### 6.1.3. Wall thickness for fibrosis imaging

A further advantage of accurate atrial wall thickness reconstruction is the potential for use of atrial wall segmentations as a volumetric mask in fibrosis imaging. The segmentation of fibrosis from LGE MRI is susceptible to over segmentation, as external structures such as the descending aorta can falsely identify fibrosis. A wall thickness mask could be used in these cases to avoid interference with non-atrial tissues. A statistical atlas of thickness could guide the dilation of the endocardial surface, in cases where the atrial wall cannot be directly imaged.

### 6.1.4. Imaging wall thickness

Research on atrial wall thickness is sparse and shows great variation of values, partially due to measurement inconsistency. Ex vivo anatomical studies on wall thickness have investigated the variation throughout the atria[151,162–171]. These studies only consider discrete sample-point thickness measurements, where wall thickness is measured using callipers in ex-vivo hearts. Additionally, these studies may not be representative of active tissue, as the wall thickness varies due to contraction and blood pressure, and ex-vivo tissue may not represent vivo myocardium.

The same issue has hindered in-vivo imaging studies of the atrial wall thickness, as they also commonly utilise discrete sample points and do not measure wall thickness for the whole atria. Until now, these studies have all utilised computed

tomography[157,160,161,172–177] which has a higher resolution than MRI but a low soft tissue contrast. Later in this chapter, we will demonstrate how novel MRI protocols can be applied to reconstruct the wall thickness non-invasively and with acceptable resolution in the entire atria.

Imaging of atrial wall thickness is non-trivial. Unlike the ventricular wall which can be imaged with great success using conventional medical imaging modalities, the atrial wall is much thinner (1-5mm compared to 11mm), therefore any motion has a greater effect during image acquisition compared to the thicker ventricular wall. This causes problems for imaging methods with non-instantaneous acquisition such as MRI, as movement throughout the cardiac cycle ensures that the wall tissue does not continuously occupy the same voxels. Conventional atrial MRI considers the atria as a 2D surface which can be extracted from a contrast enhanced blood pool inside it. This is due to the low contrast between wall and lung preventing the extraction of the epicardial surface. There is also a partial volume effect with the low resolutions associated with MRI which further reduces the edge contrast and accuracy of the measurement. However the method offers significant advantages over other available methods; it is minimally invasive, it has good soft tissue contrast and is routinely applied to AF patients.

### 6.1.5. Wall thickness measurement

Atrial wall thickness has been previously studied as discreet points or regions rather than measuring a contiguous map. Reconstructing an entire 3D map offers a better insight into atrial electrophysiology but causes new image processing challenges.

Firstly segmentation is non-trivial due to the relatively low and variable contrast between the atrial wall, lung and blood. Most conventional methods of automatic and semi-automatic segmentation are not applicable. They cannot identify the inter-tissue borders continuously, and hence either over or under estimate the structure. Currently manual image segmentation, combined with automatic post-processing, although labour intensive and time consuming, still offers the best accuracy for this application.

The second issue is measurement of the wall thickness. The outcomes of such measurements can be very dependent of the algorithm used. If surface meshes of the endo- and epicardium are utilised rather than the 3D volumetric wall, measurements can be more easily performed. Studies measuring human cortical thicknesses using MRI have developed and used different automatic approaches for this. The highly convoluted nature of the cerebral cortex draws significant parallels to atrial wall, as simplistic measurement methods such as nearest-neighbour or surface normal are unsuitable, as structures can be missed.[178] A study comparing several methods found that the most accurate measurements were provided by averaged nearest neighbour (from both inner and outer surfaces)[178]. This method also has the advantage of been relatively computationally inexpensive and easy to implement, and hence was used in the current study.

The aims of this chapter were to investigate the inherent variation of the atrial wall thickness in both AF sufferers and healthy volunteers, and ascertain how these changes affect arrhythmogenesis. This was achieved by developing an image

processing pipeline converting atrial MRI data into 3D volumetric datasets for wall thickness measurements and related electrophysiology simulations.

## 6.2. Methods

This section describes the methodology for the development and analysis of the atrial wall thickness in patients and volunteers and how it can be used in computational modelling. The subjects for this work were 10 healthy volunteers (21-30years old, 3 female) and 3 pre-ablation patients (24-78 years old, 1 female) with persistent AF.

### 6.2.1. Imaging protocols

During the progression of this work a novel MRI protocol was developed in our group.[70] Images were acquired in a para-axial plane using a black blood phase-sensitive inverse recovery (PSIR) sequence with 1.4-mm isotropic resolution, but different cardiac triggering was applied for volunteers and patients.

Movements of the heart during a cardiac cycle can impede imaging in high resolution. Therefore, the optimum timing is to acquire the image when wall movement in the atria is minimised. This occurs several times, at different cardiac phases. The longest period of constant atrial volume, which indicates minimal atrial motion, is between the passive and the active atrial emptying phase (booster pump) in late diastole. This was used for volunteers using the R-wave as a trigger. In AF patient scans, the images were acquired at maximum atrial volume, after completion of atrial filling and prior to the passive emptying phase. This enabled the images to be in kept phase with standard pre-ablation angiographic gadolinium images. The gadolinium angiographic images can be used to improve the wall

segmentation. Due to the earlier acquisition point in AF patients (compared to healthy volunteers) the R-wave was insufficient and a pulse oximeter was used as a trigger (Figure 42).

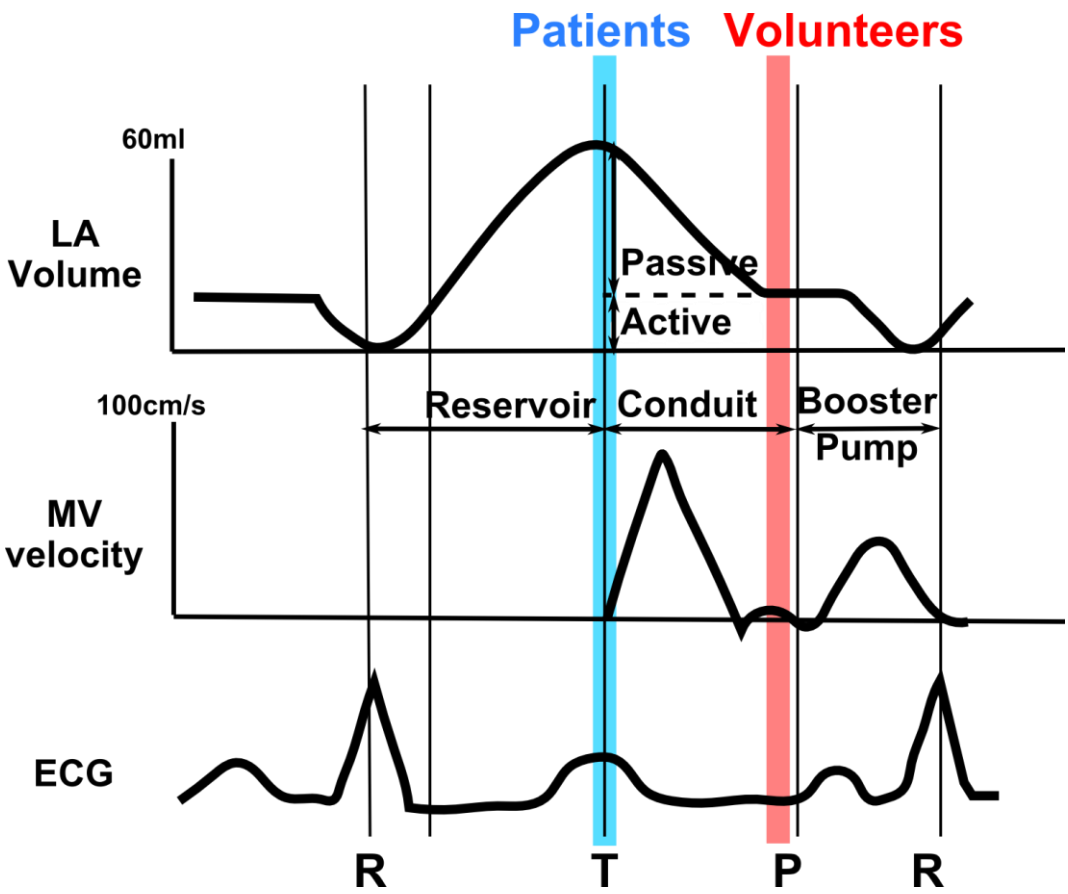


***Figure 42***. *Atrial MRI acquisition timing. The figure shows the LA volume the mitral valve velocity and the ECG during one full phase of the cardiac cycle. The blue line shows the image acquisition start for patients and the red for volunteers. The atrial phases of the atrium are indicated; the reservoir (filling) the conduit (passive emptying) and the booster pump (active emptying).*

In both subject groups respiratory gating, fat suppression and blood nulling were implemented to reduce cardiac motion and increase tissue contrast. To reduce scan time in patients the field of view was reduced and only the LA was investigated, whereas in volunteers both atria were imaged. An image quality rating was created

to qualitatively rate the likelihood of a successful segmentation. Images were rated on coverage and image quality, which accounted for Signal to Noise Ratio (SNR), blood-wall contrast and absence of artefacts. This value was essentially a segmentability measure showing the confidence in wall accuracy.

### 6.2.2. Image segmentation methods

For the images to be quantified, the atria must be segmented. Identification of the atrial wall is non-trivial. Even in successful images, only manual segmentation provided adequate results because of the low contrast and the variability of MRI intensity. The ratio of intensity between wall, lung and blood changes throughout the 3D image, making automatic segmentation difficult. Initial trials in automatic and semi-automatic segmentation were unsuccessfully implemented. This will be considered more thoroughly in future work.

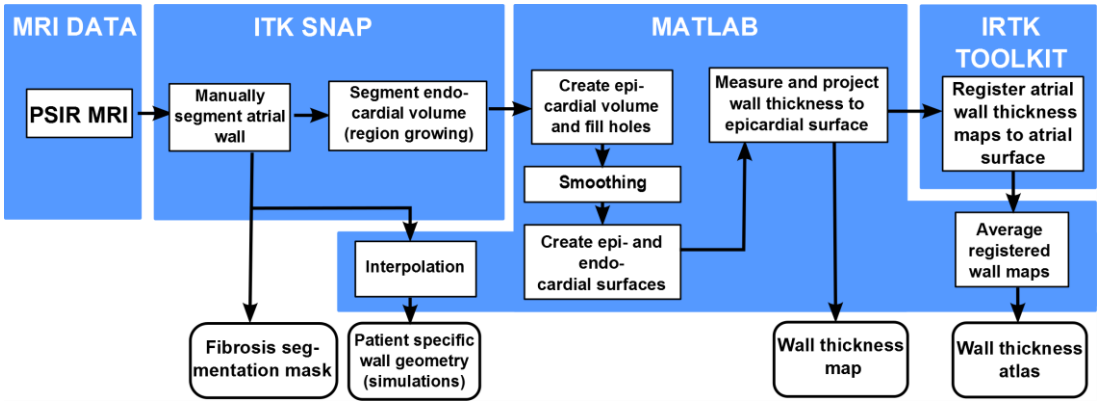


***Figure 43***. *Flowchart of image processing pipeline. Blue areas indicate the program used for each stage of the pipeline. Square boxes indicate processes and rounded boxes indicate products.*

Manual segmentation was performed in ITK-Snap™ using a 'paintbrush' tool. Each atrium was segmented slice by slice coronally and corrected in second and third passes in sagittal and axial planes. The segmented atrial wall volume is used to

create a volumetric blood image of the atrium (corresponding to the volume enclosed by the endocardial surface). This is achieved using a region growing algorithm, built into ITK Snap. Points are seeded within the blood volume of the segmented atrial wall image. These iteratively dilate until the volume reaches the boundary of the atrial wall. No smoothing is implemented to the blood volume at this stage and vessel openings are manually cropped to tidy up over-spill of the region growing algorithm.

Some atrial structures were difficult to segment. In most images PVs were not included due to the difficulty in segmentation of their thin walls. PVs and atrial septa typically have thicknesses below 1.4mm and thus could not be accurately segmented. The atrial appendages were also difficult to segment due to the high density of pectinate muscles inside them.

Variation between segmenters was investigated: 2 different datasets (both right and left atrium) were segmented twice and the differences were compared using a Dice score.

### 6.2.3. Image post processing

For thickness measurement, epi- and endocardial surface meshes need to be extracted from the volumetric data, which allows for extra-planar comparison between the two surfaces. Unless stated all post-processing was executed in Matlab$^{TM}$. A flowchart of the image processing pipeline can be seen in Figure 43.

The two segmented volumes (3D atrial wall and blood/endocardial volume) are first combined to make an epicardial surface; any holes (less than 1 voxel) in this volume

are filled using the Matlab function '*imfill*'. Meshes of the endo- and epicardial surfaces were then created with a marching cubes algorithm. The mesh quality was improved using mesh refinement and smoothing algorithms. For the volunteer datasets, the meshes were smoothed in MeshLab whereas patient cases were smoothed at the volume stage with a neighbourhood based smoothing algorithm and subsequent thresholding. This simplified the pipeline by reducing file format conversions between programs.

### 6.2.4. Thickness measurement

Various thickness measuring techniques were considered, with two being investigated in a simulated phantom (see appendix). This consisted of two concentric, yet offset, spheres which provide a controlled variation in thickness which could be calculated mathematically. These were the snake method [179](a gradient vector flow variant) and the average nearest neighbour and were both simulated in Matlab. The former uses an energy minimising spline that iteratively deforms an endocardial mesh. The mesh is contained by an MRI contour of the epicardial surface. The deformed surface can be compared on a vertex by vertex basis to the original undeformed endocardial surface mesh (Figure 44A).

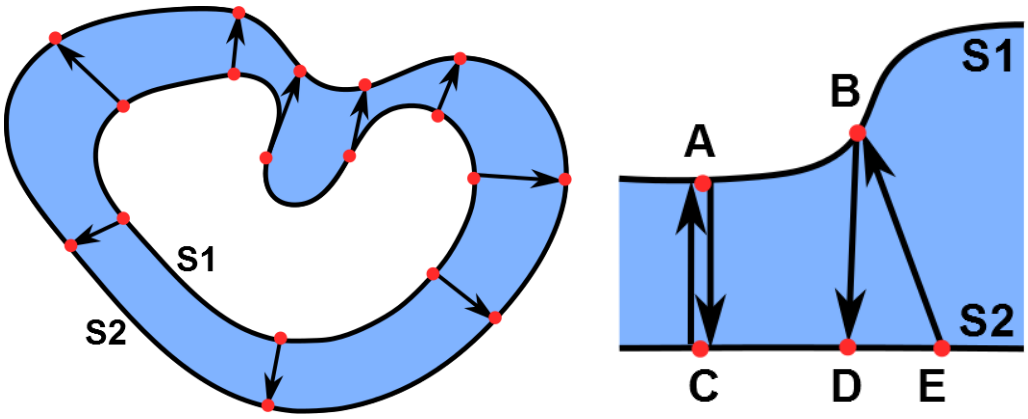


***Figure 44***. *Atrial wall thickness measurement techniques. A. Shows the snake method, where the endocardial surface (S1, black line) is deformed in the image (blue volume) to create the epicardial surface (S2 black line). The amount of deformation (black arrows) for each vertex (red circles) is the thickness. B shows the averaged nearest neighbour method. Two surfaces are compared to find the nearest neighbour for each node. In cases where both epi- and endocardial nodes are the nearest neighbours of each other (A and C) the distance is the magnitude of the vector AC. For nodes that do not have mutual transmural nearest neighbours (i.e., B) an average of the nearest neighbour vectors is calculated for each node. For example the thickness at point B is calculated as (BD+EB)/2.*

As the mesh is deformed, a mathematical balance between curvature expansion and image intensity is maintained. This ensures that each vertex is evenly spaced rather than allowing points to preferentially congregate in thinner areas. The even spacing of the deformed mesh ensures irregular wall geometries are measured accurately.

The average nearest neighbour method used an epi- and endocardial surface and for each voxel in both meshes finds a nearest neighbour on the opposite surface (see Figure 44B). In cases where nearest neighbours are mutual the distance between the vertices is the thickness. In vertices that are not mutual, nearest neighbours the average of the nearest neighbour vectors is calculated.

### 6.2.5. Atrial atlas building

The atlas of the volunteer datasets was built using the same tools as used in Chapter 5. The atrial wall thickness meshes were non-linearly registered to a single atrial geometry using the IRTK-toolkit. The LA and RA were processed separately into 2 separate geometries.

### 6.2.6. Image-based atrial simulations

The 3D computational models used in Chapters 3-5 were implemented using the volunteer atrial geometry datasets. In order to purely investigate the effects of thickness and shape, the model was devoid of fibre orientation, regional heterogeneity and fibrosis. All parameters of the monodomain equation and its numeral solver were the same as the model described in Chapter 3, but utilising only the higher (longitudinal) diffusion coefficient value. In these simulations AF based ionic remodelling was implemented so that a stable rotor could be initiated. Which was achieved with cross-field protocol (Figure 8B). This was highly controlled, by holding the opposite side of the atria inactive until the rotor had stabilised, thus preventing additional rotor initiation and rotor meandering to the other side in the initial stages of the simulation.

Due to the smaller space step required for the numerical integration of the 3D atrial model, the volunteer datasets were interpolated from 1.4mm to 0.3mm in Matlab. This had an additional beneficial effect of smoothing the “staircase” effect seen in the segmented volumes. The atria were simulated separately; this reduced the complexity of the wave dynamics and permitted rotor tracking.

For simplicity, rotor tracking was performing in pseudo 3D in Matlab, by projecting activation patterns onto a 2D plane. Subsequent voltage iso-lines of -30mV were compared and their intersection provided the rotor tip. The approach was semi-automatic and required user guidance in order to verify the correct intersection.

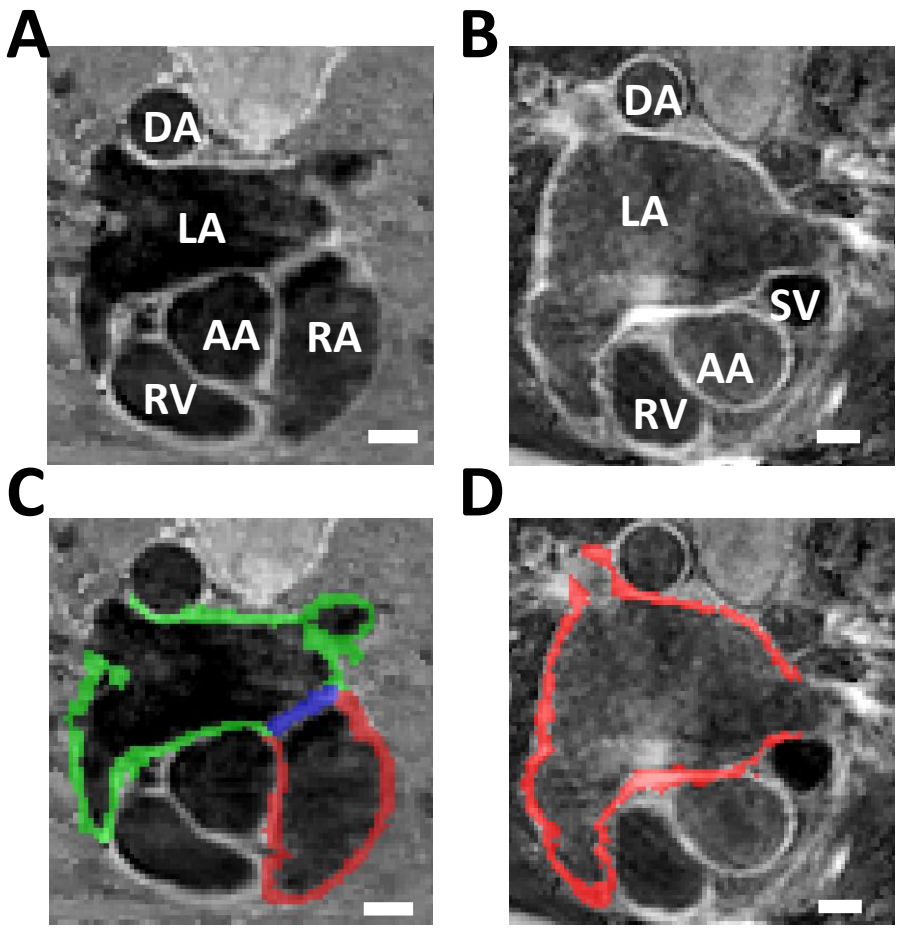


***Figure 45****. Segmentation of patient and volunteer MR images. A and C show a volunteer image without (A) and with (C) manual atrial segmentation. Green indicates the left atrium, red the right atrium and blue the atrial septum. B and D show a patient scan without (B) and with (D) manual atrial segmentation. In this instance the left atrium is indicated in red. White lines in the bottom right corner indicate a 1cm scale. Structures in A and B are annotated: DA and AA indicate the descending and ascending aorta, RV indicates right ventricle and SVC the superior vena cava. Scale bars are 10mm.*

Preliminary simulations were performed in our group[180] using a simplified cardiac electrophysiological model, the Fenton-Karma[66] (FK). This showed rotor stabilisation in regions of highly heterogeneous wall thickness, particularly the rotor meandering occurred along the CT. In these simulations, rotors were sensitive to the proximity to structural heterogeneity, i.e. rotors that were 'out-of-range' did not react to the presence of wall thickness heterogeneities. This gives a good opportunity to compare the two models (FK used previously in our group and CRN used in this study) within the same geometry, and whether the structural properties have the same effects.

## 6.3. Results

### 6.3.1. Atrial MRI data acquisition

The MR images seen in Figure 45 show a good contrast between the myocardium and the blood in both volunteers and patients. However, there was still significant variation in contrast and SNR between subjects exemplified by the difference between Figure 45A and B. The success rate was highly dependent on patient heart and breathing rate.

Segmentations for both patients and volunteers were performed on all datasets with a moderate or higher quality rating. Segmentation accuracy was reduced in highly convoluted atria due to the difficulty identifying adjacent regions (particularly with convoluted PV morphologies), and in some instances the AS was not observable.

The Dice coefficient estimated in each of the atria of two randomly chosen volunteers was 0.82 ± 0.06, ranging from 0.73 to 0.86. This shows a good agreement between atrial segmentations performed by different segmenters.

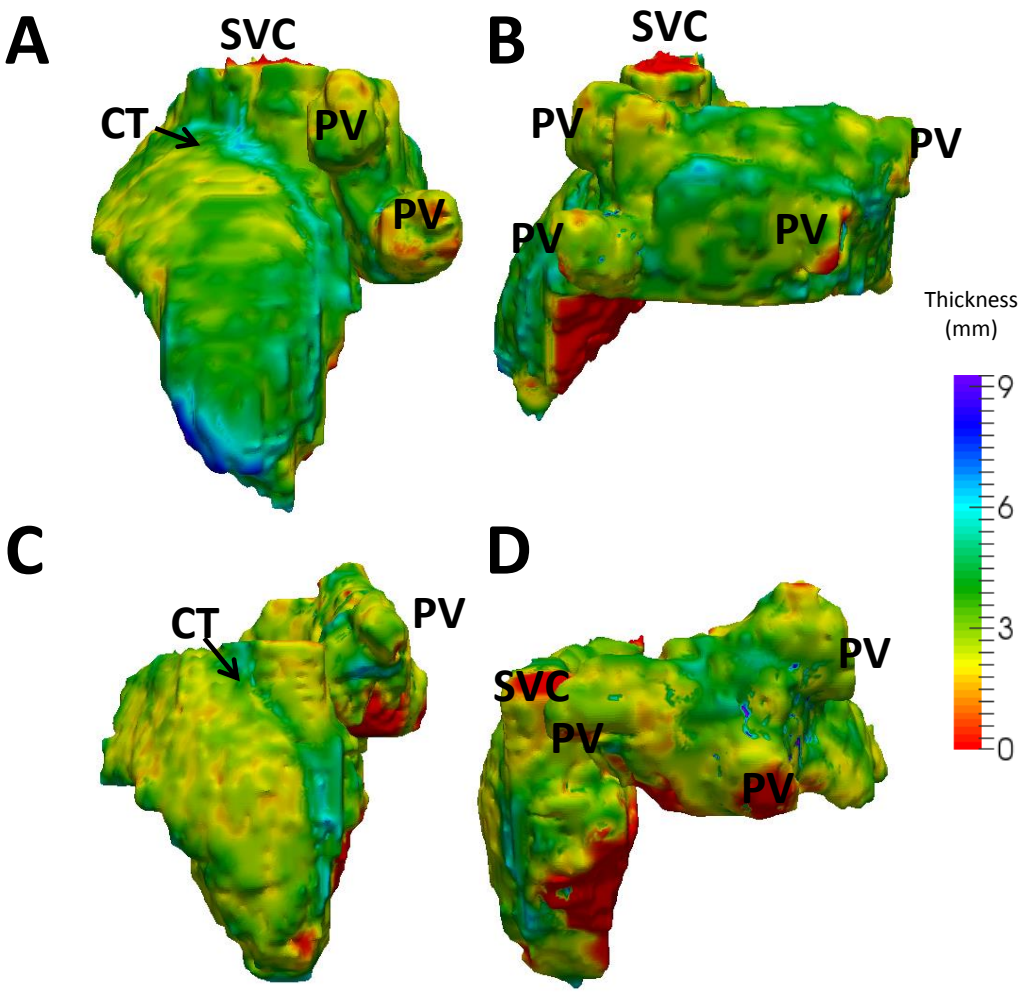


***Figure 46***. *Atrial wall thickness maps of two volunteers. A and C show the right atrium maps of the two volunteers and B and D show the corresponding left atria. Atrial structures are annotated, including the CT which can be observed as a significantly thicker region in the right atria. Red areas indicate vessel openings hence zero thickness.*

### 6.3.2. Wall thickness in volunteers

Each of the 10 volunteer MRI datasets was processed to produce a unique atrial wall thickness map (Figure 46). All maps showed regional variation of the atrial wall thickness, but the measured values were within bounds reported in the literature (Table 7).

The mean thickness for volunteers was 2.4 ± 0.7 mm in the LA and 2.7 ± 0.7 mm in the RA. Between subjects the variation was less than 1mm. This is in good agreement with both literature measurements using computed tomography and ex-vivo anatomical dissection. Only in two instances are the results towards the upper limit, for the LIPV and the anterior LA.

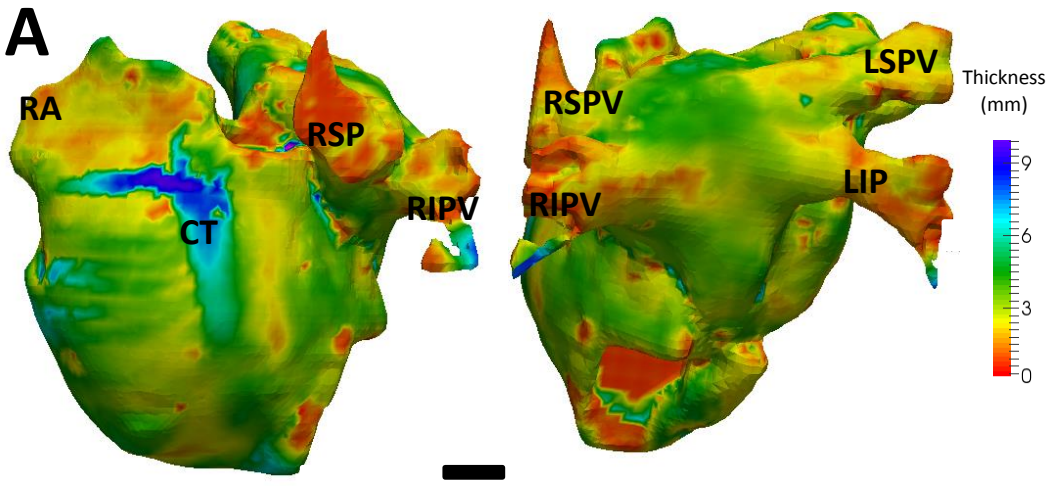


***Figure 47****. Atrial thickness map in the Visible Human Female dataset. A shows the RA and B focuses on the LA. The thicker CT and PM in the RA and the thinner PVs in the LA are seen clearly, similar to the reconstructions in Figures 4-5.*

Thickness variation in the reconstructed maps enabled the observation of different atrial structures, such as the CT which had larger thickness of 3.5-4.2mm

(contributing to higher mean thickness in the RA), and the PVs which had a lower thickness of 1.5-2mm.

A thickness map of the Visible Human Female dataset (which was used in the previous chapters) was also investigated. This compared well to the thicknesses obtained from volunteer MRI data, and had an average thickness of 2.7± 1.4mm.

The volunteer datasets were non-linearly registered to produce a unique atlas of regionally averaged wall thicknesses in the entire atria (Figure 49).

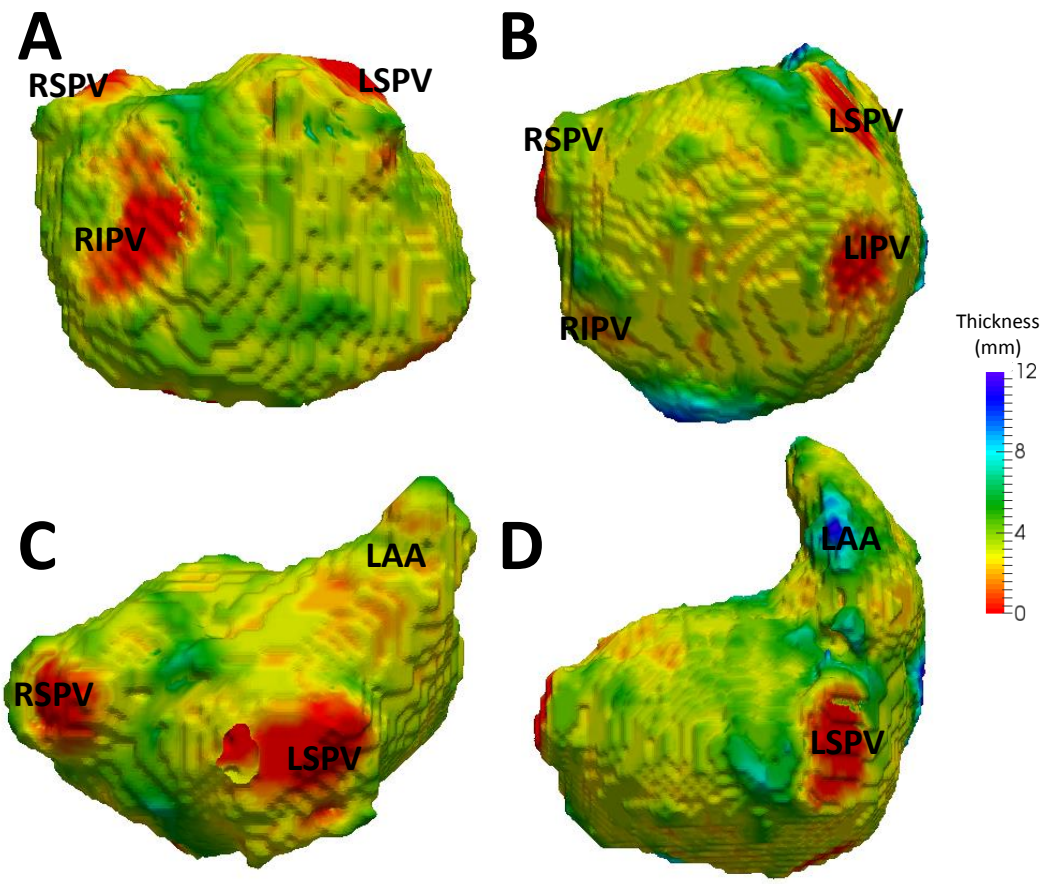


***Figure 48**. Left atrial wall thickness maps of two patients. A and C show posterior views of two different patient datasets and B and D show the corresponding top views for the same patients. In these segmentations PVs are cropped flat with the atrium due to incomplete segmentation.*

### 6.3.3. Wall thickness in patients

All of the 3 patient MRI datasets were also processed to produce left atrial wall thickness maps illustrated in Figure 48. The thin PV trunks were too difficult to accurately segment and were not included.

One of the three subjects datasets does not include a LAA, which may be due to an abnormally small appendage or that it may have been out of view. The mean of the patient datasets wall thickness was higher than the average of volunteer datasets. However 3 datasets is not a significant enough sample to extrapolate a concrete relationship between patients and volunteers. This may be due to the presence of disease or because the data acquisition was in a different phase of cardiac

The average LA value was 3.2mm +/-0.9mm, with the regional variations displayed in Table 7.

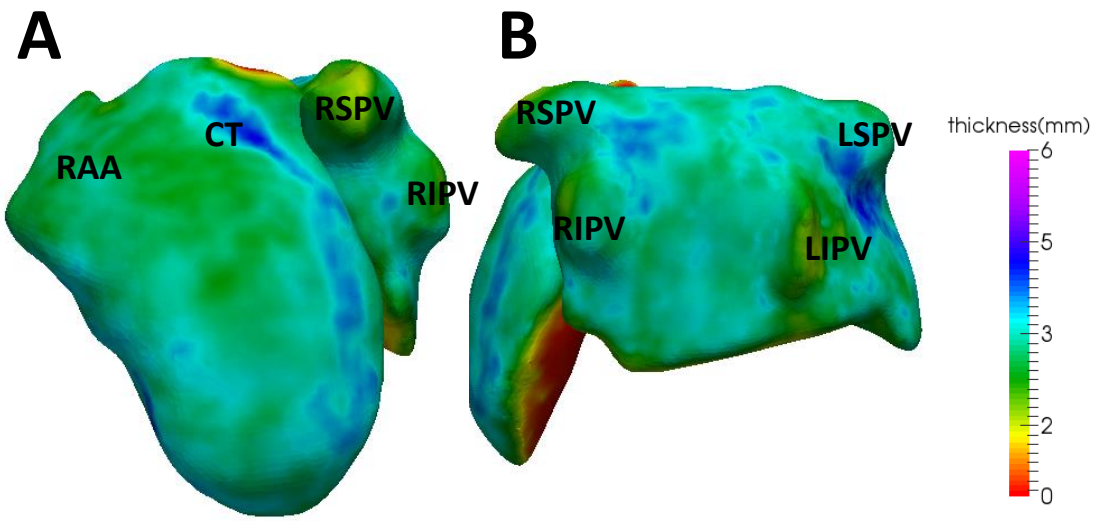


***Figure 49**. The atrial wall thickness atlas for 10 volunteer datasets. A shows the RA and B focuses on the left. Note the thicker CT in the RA and the thinner PVs in the LA.*

### 6.3.4. Image-based 3D atrial simulations

Simulations of the 3D atrial model based on the reconstructed volunteer RA geometry and CRN electrophysiology model with AF remodelling showed a stable rotor with significant meandering (Figure 50). The rotor tip tracking effectively monitored the rotor dynamics to explore how the multiple thickness transitions of the atria affect its meandering. Previous simulations with the FK kinetics produced neat 'petals' of a typical flower-pattern meander (Figure 50A), whereas new simulations with the remodelled CRN kinetics producing a much more extensive hyper-meander (Figure 50B). The rotor movement directions were also different, with the FK model producing rotor movement along the CT and the CRN to the thinnest part of the atria.

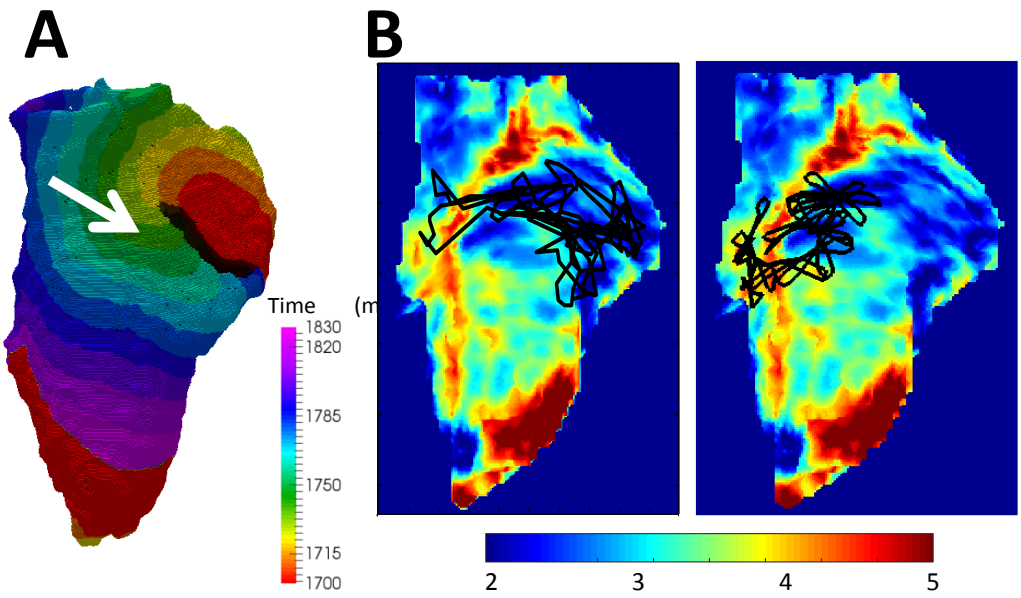


***Figure 50***. *Atrial activation map and rotor tracking maps. A shows an activation map of a rotor in the RA with the remodelled CRN model in a volunteer RA. The white arrow indicates the movement of the rotor core. B shows the corresponding rotor tracking pattern. C shows simulations in the same geometry but with the FK model performed previously by our group*[180]*. Notice the difference in rotor meander patterns (black lines) and direction (arrows) in relation to the wall thickness (palette below).*

Areas of high thickness heterogeneity did not have the same effect in simulations with different ionic models. Note that previous studies have also reported conflicting hypothesis regarding the rotors movement near the thickness gradients, with the rotors pinned to the thick CT[158], moving along the thickness gradient[38] or moving down the gradient into the thinnest region.[40] These results provide further evidence that rotor movement may be determined by a combination of geometry and ionic kinetics, such as the interplay between the relative extent of thickness gradients and rotor meander.

## 6.4. Discussion

This chapter presents the first reconstructions of atrial wall thickness maps obtained from black-blood PSIR MRI of 10 healthy volunteers and 3 patients with persistent AF. Good agreement of wall thickness estimates with previous reports (Table 7) and with the 0.33mm resolution Visible Female atrial model suggests the MRI spatial resolution of 1.4mm did not introduce detectable systematic errors in the wall thickness measurement. These reconstructions were also used as proof-of-concept for image-based 3D atrial simulations.

### 6.4.1. Atrial wall imaging

In terms of the image acquisition, there were significant differences between the patients and the volunteers. Primarily, the higher thickness values in patients may be explained by the fact that the images were acquired in different phases of cardiac cycle. In 2 patients, the images were acquired in atrial diastole and the atrial myocardium was minimally contracted. The higher thickness in patients may also be due to the pathology of their disorder or age related wall changes.

It should also be noted that in the patient scans, the LA volume was also maximised, which may stretch the wall longitudinally, thus changing the thickness compared to late atrial diastole (volunteers).

### 6.4.2. Wall thickness measurement

In terms of the wall thickness measurements, both methods considered performed well in the geometric phantom, but the average nearest neighbour methods was more efficient in atrial geometries. This was because the snake method was computationally expensive and proved too difficult to implement in complex atrial geometries. In regions of highly convoluted tissue structure, such as the appendages, the deformed mesh of the snake method became twisted and would not conform to the epicardial surface.

The average nearest neighbour method has been shown to have good results in previous studies, specifically when used to measure cortical thicknesses in the brain.[178] This research's implementation was computationally inexpensive and provided the meshes were sufficiently dense, produced accurate wall thickness measurements.

Atrial wall thicknesses and thickness variations for both volunteers and patients match those measured in literature for both imaging studies and ex-vivo anatomical studies. The regional variation shown in this study, matches the literature, with the PV (when segmented) having lower thickness and the CT having higher thickness. The wall thickness of these structures is critically important to understanding the role of geometric factors in mechanisms of AF.

| Study | 181 | 171 | 170 | 169 | 176 | 175 | 174 | 157 | 161 | 160 | 173 | 177 | 151 | 168 | 167 | 166 | 172 | 165 | 163 | 164 | 162 | Current Study Vol | Current Study Pat |
|---|---|---|---|---|---|---|---|---|---|---|---|---|---|---|---|---|---|---|---|---|---|---|---|
| No. hearts | 10 | 15 | 20 | 8 | 9 | 42 | 33 | 50 | 33 | 31 | 86 | 54 | 20 | 20 | 7 | 26 | 60 | 34 | 97 | 45 | 239 | 10 | 3 |
| Method | T | A | A | A | T | T | T | T | T | T | T | T | A | A | A | A | T | A | A | A | A | MRI | MRI |
| **Superior LA** | | 4.6 ± 1.2 | | | | | | | 2.0 ± 0.6 | | | | | | | | 2.2 ± 0.5 | 1.1 ± 0.5 | | | 2.3 ± 1.0 | 2.2 ± 0.4 | 3.6 ±0.2 |
| **Middle LA** | | 3.1 ± 1.5 | | | 0.7 ± 0.2 | | | 2.2 ± 0.9 | | | | 1.8 ± 0.2 | | | | | 1.9 ± 0.5 | 1.4 ± 0.5 | | 2.5 ± 0.5 | 2.6 ± 1.0 | 2.7 ± 0.3 | 3.4 ±0.4 |
| **Inferior LA** | | 3.2 ± 1.4 | | | | | | | | | | | | 1.7 ± 0.6 | | | 1.8 ± 0.4 | | | 4.2 ± 1.0 | 2.9 ± 1.3 | 3.1 ± 0.5 | 3.0 ±0.8 |
| **Anterior LA** | | | | | 2.0 ± 0.9 | | | | 1.8 ± 0.3 | | 1.9 ± 0.2 | | | 1.6 ± 0.5 | | | | 1.9 ± 0.6 | | | | 2.2 ± 0.2 | 3.9 ±1.2 |
| **LA Isthmus** | | | 2.8 ± 0.7 | | | | | | | | | | | | | | 2.1 ± 0.6 | 1.6 ± 0.5 | | | | 2.1 ± 0.3 | 2.9 ±1.1 |
| **Roof LA** | | | | | | | | | | | | 3.0 ± 0.3 | | | | | | | | | | 2.9 ± 0.2 | 3.4 ±0.9 |
| **Septum** | | | | | | | | | 2.4 ± 0.8 | | | | | | | | | 2.2 ± 0.8 | | | | 2.5 ± 0.6 | 2.4 ±0.5 |
| **LA average** | 0.9 ± 0.4 | | | 1.8 ± 0.5 | | 2.4 ± 0.5 | 2.6 | | | 2.4 ± 0.4 | | | | | 5.4 | | 1.9 ± 0.5 | | | | | 2.4 ± 0.7 | |
| **LIPV** | | | | | | | | | | | | 1.7 ± 0.2 | 0.4 ± 0.2 | 0.5 ±0.2 | | 1.5 ±0.4 | | | | | | 2.6 ± 0.4 | |
| **LSPV** | | 2.4 ± 0.5 | 3.0 ± 1.5 | | | | | | | | | 2.2 ± 0.3 | 0.7 ± 0.4 | 0.5 ± 0.2 | | 2.8 ± 0.5 | | | | | | 3.1 ± 0.1 | |
| **RIPV** | | | | | | | | | | | | 2.0 ± 0.2 | 0.2 ± 0.2 | 0.5 ± 0.2 | | 2.0 ± 0.4 | | | | | | 2.5 ±0.2 | |
| **RSPV** | | 2.0 ± 0.8 | | | | | | | | | | 2.1 ± 0.2 | 0.6 ± 0.2 | 0.5 ± 0.2 | | 2.5 ± 0.5 | | | | | | 2.7 ± 0.4 | |
| **RA average** | | | | 1.8 ± 0.4 | | | | | | | | | | | 3.8 | | | | | | | 2.7 ± 0.7 | |
| **CT** | | | | | | | | | | | | | | | | | | | 5.2 ± 1.3 | | | 5.7 ± 1.1 | |

***Table 7****. Atrial wall thickness measured in volunteers, patients and literature. "Study" corresponds to the number of a respective reference in this chapter, "Vol" and "Pat" are volunteers and patients. T = Computed tomography, A = Ex-vivo anatomical studies, pAF= persistent AF. Measurements in mm.*

The imaging pipeline developed in this study can be used in AF patients and can be appended to existing MRI protocols to produce patient-specific atrial wall thickness maps. These are likely to be of particular interest for electro-anatomical mapping and ablation therapy in AF patients. The maps may offer a particularly useful tool for ablation, as knowing the atrial thickness variation can help make the choice of the appropriate RF power for creating fully transmural lesions, thus making the procedure safer and more effective.

### 6.4.3. Simulations of wall thickness effects

Knowledge of the atrial wall thickness may also lead to better understanding of atrial electrophysiological properties by establishing quantitative links between the atrial structure and function. The simulations performed in this chapter showed that rotor movement in the RA was sensitive to the wall thickness. Although highly heterogeneous, wall thickness did not have a stabilising effect on rotors, it did have conduction velocity slowing effects that can be seen in the rotor moving either along the thick CT (Figure 50A) or down the gradient into the thinner tissue (Figure 50B).The difference may come from the increased extent and complexity of rotor meandering in the CRN model (applied in Figure 50B) compared to the simpler FK model (applied in Figure 50B). The FK model produces a smaller radius and more regular rotor meandering, which may make it more susceptible to sharp wall thickness gradients near the CT. The CRN model produces extensive hyper-meandering and in these simulations, the rotor meanders from the thicker areas in the posterior wall of the RA to the lower RAA In this region conduction velocity is reduced due to significantly thinner atrial wall of the latter areas. These results show that the atrial wall thickness can have an effect on the rotor movement

additional to that due to patchy fibrosis. Future availability of PSIR and LGE MRI data from the same patient in future should enable detailed studies of the interplay between these two structural factors.

### 6.4.4. Conclusion

The current proof-of-concept computational work provides further evidence that atrial wall thickness can contribute significantly to arrhythmogenesis. Due to high inter-patient and inter-atrial heterogeneity, the effects of patient specific atrial structure must be considered when studying AF computationally. The current 3D atrial simulations were considerably less biophysically detailed than that described in previous chapters. This helps isolate the wall thickness effects from the effects of tissue anisotropy and ionic heterogeneity. Future studies will combine the detailed 3D models of atrial heterogeneity and fibre orientation with patient-specific wall thickness and fibrosis distribution. Notably, the reconstructed atrial wall volumes can be directly applied as 3D masks for the identification and segmentation of fibrosis from patient LGE MRI scans. This opens new pathways to integrating various imaging modalities and computational approaches for the improved understanding of AF mechanisms, and ultimately for better stratification of AF patients.

# 7. Conclusions

This work set out to understand how fibrosis affects arrhythmogenesis in the atria. Due to the clinically observed correlation between AF progression and fibrosis deposition in the atria, an empirical link has been previously proposed. The aim of this work was to understand and substantiate this link with the aid of state-of-the-art computational modelling and non-invasive imaging techniques. The computational investigation was multi-scale, building up from single atrial myocyte and fibroblast models to the 3D whole human atrial model. Medical imaging provided patient-specific atrial structural data and fibrosis distributions for the 3D atrial models, which enabled the investigation of inter-patient variation. The in-silico nature of this work has the ability to study aspects of the disorder inaccessible to in-vivo analysis, such as mechanistic links between atrial fibrosis and arrhythmia.

## 7.1. Main Findings

The main findings of this work correspond with the structure of its chapters. As the models were developed and explored from single cell to 3D atria levels, different aspects of the problem were interpreted.

1. **Electrophysiological properties of atrial fibroblasts are significantly different from those of ventricular fibroblasts**. A novel model of electrophysiology of a single atrial fibroblast (based on detailed experimental data by Wu et al.[85]) and its coupling to the atrial myocyte were developed. Atrial fibroblasts in the model had higher (more positive) resting potential compared to the previous models of ventricular fibroblasts (MacCannell et al.[58]), and therefore a stronger effect on the excitability of

atrial myocytes. Effects of M-F coupling with atrial fibroblasts on the APD were smaller than those of ventricular fibroblasts. The use of relevant electrophysiological data for the atrial fibroblast model make it more representative of atrial electrophysiology and better suited for the studies of atrial M-F coupling.

2. **The main effect of atrial M-F coupling is on the conduction velocity rather than the wavelength.** M-F coupling with the developed atrial fibroblast model had a substantially smaller effect on the wavelength than either M-F coupling with the MacCannell et al. ventricular fibroblast model or ionic remodelling. However, stronger effect of coupling with atrial fibroblasts on the excitability of myocytes resulted in slower conduction in atrial tissue. This functional effect should contribute to the overall conduction slowing due to structural remodelling of fibrotic atrial tissue.
3. **The structural effects of fibrosis on atrial conduction are greater than the M-F coupling effects.** In the developed 3D human atrial model, decreased M-M coupling and increased anisotropy of atrial tissue (both associated with interstitial collagen depositions due to fibrosis) had a far greater effect on atrial conduction than the electrophysiological effects associated with the M-F coupling. Hence, both functional effects of M-F coupling and structural effects of fibrosis contributed to arrhythmogenesis through the slowed conduction and generation of re-entry, but the structural effects played substantially more prominent role.
4. **Heterogeneous patchy fibrosis had a strong stabilising effect on atrial arrhythmogenesis**. While progressive conduction slowing and increased

anisotropy resulted in the generation of increasing number of re-entrant circuits in the 3D atrial model. The addition of large areas of patchy fibrosis appeared to stabilise re-entrant rotors. This was a common feature of a wide range of behaviours seen for different patient-specific distributions of fibrosis reconstructed from LGE MRI data. This provides a mechanistic explanation for AF stabilisation seen in chronic patients, and for recent successes in ablations around fibrotic areas.

5. **Atrial wall thickness is variable within the atria and between subjects and plays an important role in arrhythmogenesis**. Novel MRI techniques enabled unique reconstructions of subject-specific atrial wall thickness maps. The data clearly highlights large thickness variations throughout the atria, providing means for the generation of a unique statistical atlas. This data was integrated into simple atrial models to demonstrate the role of wall thickness gradients in the atrial rotor dynamics.
6. **Patient-specific atrial structure and fibrosis distribution are critically important factors for arrhythmogenesis**. Integration of patient-specific fibrosis distribution and atrial geometry into the 3D atrial model, enables simulations of vastly different forms of re-entry. The model provides means for systemising these scenarios and understanding the mechanistic links between patient variations of electrophysiological dysfunction and underlying atrial tissue substrate. Novel pipelines for MRI processing and combination with 3D atrial models were developed in this study. They provided important tools for future patient-specific studies of AF and may provide useful tools for the guidance of clinical ablation procedures.

## 7.2. Future work

The logical next step for the computational model development is to include more biophysical detail, for further model personalisation. In particular, the addition of personalised fibre orientation for patient geometry datasets, which could lead to a substantial improvement of the predictive power of the models. However, the existing imaging modalities cannot provide such information for a patient. Along with the current anatomical knowledge, future rule-based fibre orientation models should account for patient-specific atrial activation sequences. Such methods are currently being developed at the Karlsruhe Institute of Technology.

Another major limitation of the computational modelling in this work is the lack of comprehensive clinical validation. Myocyte electrophysiology has been extensively studied, with detailed experimental data available from ionic channel to myofibre levels for model validation. However only limited information is available when it comes to complex whole-atria electrophysiology. Filling the gap in knowledge between in-vivo measurement of single cell dynamics and 3D atrial wave propagation will provide a challenge for future experimental studies. In the current study, such a gap is filled using image-based modelling. However to complete the validation, improvement of clinical electro-anatomical mapping, including better resolution on mapping catheters and whole atria-coverage, is required. It would provide a vastly better understanding of rotor dynamics, mechanisms of wave breakdown and when combined with atrial imaging, a better understanding of the arrhythmogenic properties of atrial tissue structure.

# Appendix

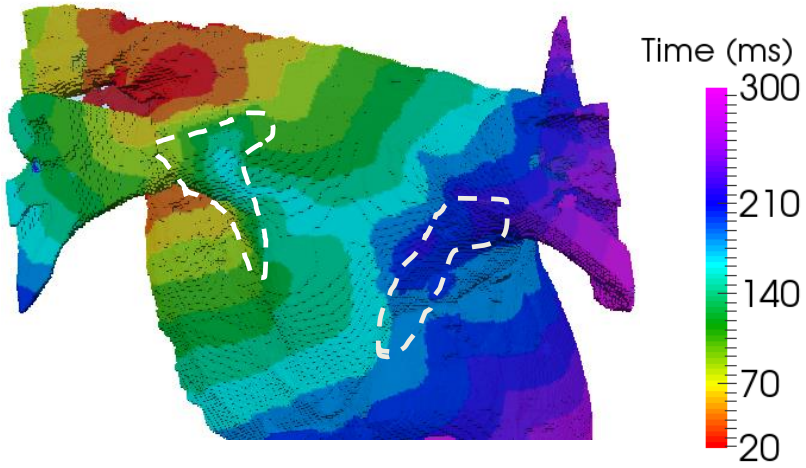


***Figure 51***. *Normal conduction in the patient specific fibrosis model. White dashed lines indicate the areas of dense fibrosis (level 4-5). This simulations shows wave front deformation in dense fibrosis region but the pacing frequency is not sufficient for re-entry.*

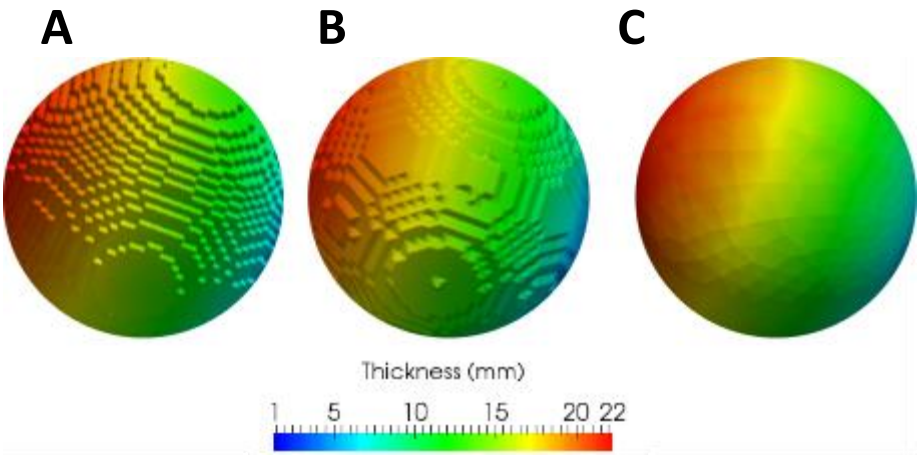


***Figure 52***. *Atrial wall measurement methods. A shows the averaged nearest neighbour method, B shows the snake method and C shows the ground truth calculated mathematically and registered to a spherical mesh.*

## M-F atrial fibroblast model

The following is the Matlab script for generating the ionic current $I_{Gap}$ from the atrial fibroblast.

```
naiF =1.117e+01;
nacF= 140.;
kcF = 5.4;
kiF =1.390e+02;
gbnaF = 0.0006744375;
GKURF=0.6;
gtoF = 0.1652*0.1;
GT1F=0.95;

for time=0:1:tmax


      EnaF = 26.71*log(nacF/naiF)  ;
      EkF = 26.71*log(kcF/kiF)  ;

      insF = 0.018*vF;   % nonspecific current
      ik1F = 0.03*(vF+86.75)/(1+exp(0.05*(vF+20)));
      %modified ik1
      %to super impose with ins
      gkurF = GKURF*0.005+0.05/(1+exp(-(vF -15)/13.0));
      itoF = gtoF*oaF *oaF *oaF *oiF *(vF -EkF);
      ikurF = gkurF*uaF *uaF *uaF *uiF *(vF -EkF);
      %/*** Na background current ***/
      ibnaF =9*gbnaF*(vF - EnaF); % increased back na %5x to get to
      resting potential of 47.68
           inak_fibro = inak_fibro_max * (kc / (kc +
      kmk_binding_fibro))...
              * (     sqrt(Nai_fibro*Nai_fibro*Nai_fibro)...
              / ( sqrt(Nai_fibro*Nai_fibro*Nai_fibro)...
              +
      sqrt(kmna_binding_fibro*kmna_binding_fibro*kmna_binding_fibro)
      ))...
              * ((vF - v_revF) / (vF - B_fibro));

          % update oa ito gate (dt in ms) */
      vshift = -10;
      a = 0.65./(exp((vF -vshift+0.0)./-8.5)+exp((vF -vshift-
      40.0)./-59.0));
      b = 0.65./(2.5+exp((vF -vshift+72.0)./17.0));
      tau = 15*1./(a+b);                              % 15*with
      added scalling factors to time constants x15
      inf = 1./(1+exp((vF -vshift+10.47)./-17.54));

      oaF = inf + (oaF -inf)*exp(-Tfac*dt/tau);
      % update oi ito gate */
      vshift = -10;
      a = 1./(18.53+exp((vF -vshift+103.7)./10.95));
      b = 1./(35.56+exp((vF -vshift-8.74)./-7.44));
      tau = 15*1./(a+b);                               %15 with
      added scalling factors to time constants x15
      inf = 1./(1+exp((vF -vshift+33.1)./5.3));
      oiF = inf + (oiF -inf)*exp(-Tfac*dt/tau);
```

```
        % update ua ikur gate */
        vshift = -10;%0;
        a = 0.65./(exp((vF-vshift+0.0)./-8.5)+exp((vF-vshift-40.0)./-
        59.0
        b = 0.65./(2.5+exp((vF-vshift+72.00)./17.0));
        tau = 1./(a+b);                                  % not scaled
        by 5
        inf = 1./(1+exp((vF-vshift+20.3)./-9.6));
        uaF  = inf + (uaF -inf)*exp(-Tfac*dt/tau);
        % update ui ikur gate */
        vshift = -10;
        a = 1./(21+exp((vF-vshift-195)./-28));
        b = 1./(exp((vF-vshift-168)./-16));
        tau = 5*1./(a+b);
        %5*with added scalling factors to time constants x5
        inf = 1./(1+exp((vF-vshift-109.45)./27.48));
        uiF  = inf + (uiF -inf)*exp(-Tfac*dt/tau);

                %//total current across fibroblast
        itot_fibro = itoF +ik1F +insF +ibnaF +inak_fibro + ikurF;%+
        inakF;%;%

        %%%%%%%%%%%%%%%%%%%%%%%%%%%%%%%%%%%%%%%%%%%%
        I_gap = GgapF * (vF - V) / CmF;%=0;
        if COUPLING==0
            I_gap=0;
        end
        vF = vF - dt * (itot_fibro + I_gap);

        I_gap2 = COUPLING * GgapF * (V - vF) / Cm;


end
```

# List of figures

# List of tables

# References


1. Schoonderwoerd, B. a., Van Gelder, I. C., Van Veldhuisen, D. J., Van Den Berg, M. P. & Crijns, H. J. G. M. Electrical and structural remodeling: Role in the genesis and maintenance of atrial fibrillation. *Prog. Cardiovasc. Dis.* **48,** 153–168 (2005).

2. Jahangir, A. *et al.* Long-term progression and outcomes with aging in patients with lone atrial fibrillation: A 30-year follow-up study. *Circulation* **115,** 3050–3056 (2007).

3. Kannel, W. B., Wolf, P. A., Benjamin, E. J. & Levy, D. Prevalence, incidence, prognosis, and predisposing conditions for atrial fibrillation: population-based estimates. *Am. J. Cardiol.* **82,** 2N–9N (1998).

4. Wang, T. J. *et al.* Temporal relations of atrial fibrillation and congestive heart failure and their joint influence on mortality: the Framingham Heart Study. *Circulation* **107,** 2920–2925 (2003).

5. Lubitz, S. A., Benjamin, E. J. & Ellinor, P. T. Atrial fibrillation in congestive heart failure. *Heart Fail. Clin.* **6,** 187–200 (2010).

6. Lloyd-Jones, D. M. *et al.* Lifetime risk for development of atrial fibrillation: the Framingham Heart Study. *Circulation* **110,** 1042–1046 (2004).

7. Chugh, S. S. *et al.* Worldwide Epidemiology of Atrial Fibrillation: A Global Burden of Disease 2010 Study. *Circulation* **129,** 837–847 (2014).

8. Han, F. T. & Marrouche, N. An atrial fibrosis-based approach for atrial

fibrillation ablation. *Future Cardiol.* **11,** 673–681 (2015).

9. Kottkamp, H., Berg, J., Bender, R., Rieger, A. & Schreiber, D. Box Isolation of Fibrotic Areas (BIFA): A Patient-Tailored Substrate Modification Approach for Ablation of Atrial Fibrillation. *J. Cardiovasc. Electrophysiol.* **27,** n/a–n/a (2015).

10. Al-Saady, N. M., Obel, O. a & Camm, a J. Left atrial appendage: structure, function, and role in thromboembolism. *Heart* **82,** 547–554 (1999).

11. Platonov, P. G., Mitrofanova, L., Ivanov, V. & Ho, S. Y. Substrates for intra-atrial and interatrial conduction in the atrial septum: anatomical study on 84 human hearts. *Heart Rhythm* **5,** 1189–95 (2008).

12. Platonov, P. G. *et al.* Preferential conduction patterns along the coronary sinus during atrial fibrillation in humans and their modification by pulmonary vein isolation. *J Electrocardiol* **44,** 157–163 (2011).

13. Ho, S. Y., Cabrera, J. A. & Sanchez-Quintana, D. Left atrial anatomy revisited. *Circ. Arrhythm. Electrophysiol.* **5,** 220–8 (2012).

14. Klatt, Edward, C. Normal myocardial histology. *WebPath* http://library.med.utah.edu/WebPath/HISTHTML/NORMA (2016).

15. Nattel, S. & Carlsson, L. Innovative approaches to anti-arrhythmic drug therapy. *Nat. Rev. Drug Discov.* **5,** 1034–1049 (2006).

16. Graux, P. *et al.* Wavelength and atrial vulnerability: an endocavitary approach in humans. *Pacing Clin. Electrophysiol.* **21,** 202–208 (1998).

17. Maceira, A. M., Cosín-Sales, J., Roughton, M., Prasad, S. K. & Pennell, D. J. Reference left atrial dimensions and volumes by steady state free precession cardiovascular magnetic resonance. *J. Cardiovasc. Magn. Reson.* **12,** 1–10 (2010).

18. Roy, D. *et al.* Amiodarone to prevent recurrence of atrial fibrillation. Canadian Trial of Atrial Fibrillation Investigators. *N. Engl. J. Med.* **342,** 913–920 (2000).

19. Weerasooriya, R. *et al.* Catheter ablation for atrial fibrillation: are results maintained at 5 years of follow-up? *J. Am. Coll. Cardiol.* **57,** 160–6 (2011).

20. Calkins, H. *et al.* 2012 HRS/EHRA/ECAS expert consensus statement on catheter and surgical ablation of atrial fibrillation: recommendations for patient selection, procedural techniques, patient management and follow-up, definitions, endpoints, and research trial design: a re. *Heart Rhythm* **9,** 632–696.e21 (2012).

21. Trayanova, N. A. *et al.* Computational cardiology: how computer simulations could be used to develop new therapies and advance existing ones. *Europace* **14,** v82–9 (2012).

22. Zahid, S. *et al.* Patient-derived models link re-entrant driver localization in atrial fibrillation to fibrosis spatial pattern. *Cardiovasc. Res.* **110,** 443–454 (2016).

23. Jacquemet, V. Lessons from computer simulations of ablation of atrial fibrillation. *J. Physiol.* **594,** 2417–2430 (2016).

24. Wijffels, M. C., Kirchhof, C. J., Dorland, R. & Allessie, M. A. Atrial fibrillation begets atrial fibrillation. A study in awake chronically instrumented goats. *Circulation* **92,** 1954–1968 (1995).

25. Zipes, D. P. & Jalife, J. *Cardiac Electrophysiology: From Cell to Bedside*. (Saunders/Elsevier, 2009).

26. Schotten, U., Verheule, S., Kirchhof, P. & Goette, A. Pathophysiological mechanisms of atrial fibrillation: a translational appraisal. *Physiol. Rev.* **91,** 265–325 (2011).

27. Nattel, S. & Dobrev, D. The multidimensional role of calcium in atrial fibrillation pathophysiology: mechanistic insights and therapeutic opportunities. *Eur. Heart J.* **33,** 1870–1877 (2012).

28. Jalife, J., Berenfeld, O. & Mansour, M. Mother rotors and fibrillatory conduction: A mechanism of atrial fibrillation. *Cardiovasc. Res.* **54,** 204–216 (2002).

29. Comtois, P., Kneller, J. & Nattel, S. Of circles and spirals: bridging the gap between the leading circle and spiral wave concepts of cardiac reentry. *Europace* **7,** 10–20 (2005).

30. Narayan, S. M. *et al.* Ablation of Rotor and Focal Sources Reduces Late Recurrence of Atrial Fibrillation Compared With Trigger Ablation Alone. *J. Am. Coll. Cardiol.* **63,** 1761–1768 (2014).

31. Narayan, S. M., Krummen, D. E., Clopton, P., Shivkumar, K. & Miller, J. M.

Direct or coincidental elimination of stable rotors or focal sources may explain successful atrial fibrillation ablation: on-treatment analysis of the CONFIRM trial (Conventional ablation for AF with or without focal impulse and rotor modulation). *J. Am. Coll. Cardiol.* **62,** 138–47 (2013).

32. Gray, R. A. *et al.* Mechanisms of cardiac fibrillation. *Science (New York, N.Y.)* **270,** 1222–1225 (1995).

33. Moe, G., Rheinboldt, W. & Abildskov, J. A computer model of atrial fibrillation. *Am. Heart J.* **67,** 200–220 (1964).

34. Chen, S. -a. *et al.* Initiation of Atrial Fibrillation by Ectopic Beats Originating From the Pulmonary Veins : Electrophysiological Characteristics, Pharmacological Responses, and Effects of Radiofrequency Ablation. *Circulation* **100,** 1879–1886 (1999).

35. Cabo, C. *et al.* Wave-Front Curvature as a Cause of Slow Conduction and Block in Isolated Cardiac Muscle. *Circ Res.* **75,** 1014–1029 (1994).

36. Wang, Y. G. *et al.* Electrical interactions between a real ventricular cell and an anisotropic two-dimensional sheet of model cells. *Am. J. Physiol. Heart Circ. Physiol.* **278,** H452–60 (2000).

37. Feng, J., Yue, L., Wang, Z. & Nattel, S. Ionic mechanisms of regional action potential heterogeneity in the canine right atrium. *Circ. Res.* **83,** 541–551 (1998).

38. Aslanidi, O. V *et al.* 3D virtual human atria: A computational platform for

studying clinical atrial fibrillation. *Prog. Biophys. Mol. Biol.* **107,** 156–168 (2011).

39. Aslanidi, O. V *et al.* Heterogeneous and anisotropic integrative model of pulmonary veins: computational study of arrhythmogenic substrate for atrial fibrillation. *Interface Focus* **3,** 20120069 (2013).

40. Yamazaki, M. *et al.* Heterogeneous atrial wall thickness and stretch promote scroll waves anchoring during atrial fibrillation. *Cardiovasc. Res.* **94,** 48–57 (2012).

41. Ong, J. J. *et al.* The relation between atrial fibrillation wavefront characteristics and accessory pathway conduction. *J. Clin. Invest.* **96,** 2284–96 (1995).

42. Colman, M. a *et al.* Pro-arrhythmogenic Effects of Atrial Fibrillation Induced Electrical Remodelling- Insights from 3D Virtual Human Atria. *J. Physiol.* **591,** 1–24 (2013).

43. Nattel, S., Burstein, B. & Dobrev, D. Atrial remodeling and atrial fibrillation: mechanisms and implications. *Circ. Arrhythm. Electrophysiol.* **1,** 62–73 (2008).

44. Kneller, J. Cholinergic Atrial Fibrillation in a Computer Model of a Two-Dimensional Sheet of Canine Atrial Cells With Realistic Ionic Properties. *Circ. Res.* **90,** 73e–87 (2002).

45. Nattel, S., Maguy, A., Le Bouter, S. & Yeh, Y.-H. Arrhythmogenic ion-channel

remodeling in the heart: heart failure, myocardial infarction, and atrial fibrillation. *Physiol. Rev.* **87,** 425–56 (2007).

46. Gramley, F. *et al.* Atrial fibrosis and atrial fibrillation: the role of the TGF-β1 signaling pathway. *Int. J. Cardiol.* **143,** 405–13 (2010).

47. Souders, C. A., Bowers, S. L. K. & Baudino, T. A. Cardiac fibroblast: the renaissance cell. *Circ. Res.* **105,** 1164–1176 (2009).

48. Clayton, R. H. *et al.* Models of cardiac tissue electrophysiology: progress, challenges and open questions. *Prog. Biophys. Mol. Biol.* **104,** 22–48 (2011).

49. de Bakker, J. M. *et al.* Reentry as a cause of ventricular tachycardia in patients with chronic ischemic heart disease: electrophysiologic and anatomic correlation. *Circulation* **77,** 589–606 (1988).

50. de Bakker, J. M. *et al.* Slow conduction in the infarcted human heart. 'Zigzag' course of activation. *Circulation* **88,** 915–926 (1993).

51. Spach, M. S. *et al.* The functional role of structural complexities in the propagation of depolarization in the atrium of the dog. Cardiac conduction disturbances due to discontinuities of effective axial resistivity. *Circ. Res.* **50,** 175–191 (1982).

52. de Jong, S., van Veen, T. a B., van Rijen, H. V. M. & de Bakker, J. M. T. Fibrosis and cardiac arrhythmias. *J. Cardiovasc. Pharmacol.* **57,** 630–8 (2011).

53. Kawara, T. *et al.* Activation delay after premature stimulation in chronically diseased human myocardium relates to the architecture of interstitial

fibrosis. *Circulation* **104,** 3069–75 (2001).

54. Baum, J. R., Long, B., Cabo, C. & Duffy, H. S. Myofibroblasts cause heterogeneous Cx43 reduction and are unlikely to be coupled to myocytes in the healing canine infarct. *AJP Hear. Circ. Physiol.* **302,** H790–H800 (2011).

55. Torre-Amione, G. *et al.* Proinflammatory cytokine levels in patients with depressed left ventricular ejection fraction: a report from the Studies of Left Ventricular Dysfunction (SOLVD). *J. Am. Coll. Cardiol.* **27,** 1201–1206 (1996).

56. Kohl, P., Camelliti, P., Burton, F. L. & Smith, G. L. Electrical coupling of fibroblasts and myocytes: relevance for cardiac propagation. *J. Electrocardiol.* **38,** 45–50 (2005).

57. Li, G.-R. *et al.* Characterization of multiple ion channels in cultured human cardiac fibroblasts. *PLoS One* **4,** e7307 (2009).

58. MacCannell, K. A. *et al.* A mathematical model of electrotonic interactions between ventricular myocytes and fibroblasts. *Biophys. J.* **92,** 4121–32 (2007).

59. Chilton, L. *et al.* K+ currents regulate the resting membrane potential, proliferation, and contractile responses in ventricular fibroblasts and myofibroblasts. *Am. J. Physiol. Heart Circ. Physiol.* **288,** H2931–9 (2005).

60. Taccardi, B. *et al.* Useful lessons from body surface mapping. *J. Cardiovasc. Electrophysiol.* **9,** 773–786 (1998).

61. O'Hara, T. & Rudy, Y. Quantitative comparison of cardiac ventricular myocyte

electrophysiology and response to drugs in human and nonhuman species. *Am. J. Physiol. - Hear. Circ. Physiol.* **302,** H1023–H1030 (2012).

62. Potse, M., Dubé, B., Richer, J., Vinet, A. & Gulrajani, R. M. A Comparison of Monodomain and Bidomain Reaction-Diffusion Models for Action Potential Propagation in the Human Heart. *Conf Proc IEEE Eng Med Biol Soc* 1:3895–8 (2006).

63. Trayanova, N., Plank, G. & Rodríguez, B. What have we learned from mathematical models of defibrillation and postshock arrhythmogenesis? Application of bidomain simulations. *Heart Rhythm* **3,** 1232–5 (2006).

64. Courtemanche, M., Ramirez, R. J. & Nattel, S. Ionic mechanisms underlying human atrial action potential properties: insights from a mathematical model. *Am. J. Physiol.* **275,** H301–21 (1998).

65. ten Tusscher, K. H. W. J., Noble, D., Noble, P. J. & Panfilov, A. V. A model for human ventricular tissue. *Am. J. Physiol. Heart Circ. Physiol.* **286,** H1573–89 (2004).

66. Fenton, F. & Karma, A. Vortex dynamics in three-dimensional continuous myocardium with fiber rotation: Filament instability and fibrillation. *Chaos* **8,** 20–47 (1998).

67. Grandi, E., Pasqualini, F. S. & Bers, D. M. A Novel Computational Model of the Human Ventricular Action Potential and Ca Transient. *Journal of molecular and cellular cardiology* **48,** 112 (2010).

68. Westebbe, B., Thiele, J. & Kraft, M. A Mobile Gait Analysis System For Optimization Of Prosthetic Alignments. *Biomed. Eng. (NY).* **58,** 24–25 (2013).

69. Colman, M. A. Development of a Biophysically Detailed Model of the Human Atria for the Investigation of the Mechanisms of Atrial Arrhythmias Table of Contents. (The University of Manchester, 2012).

70. Varela, M. *et al.* 3D high-resolution atrial wall thickness maps using black-blood PSIR. *J. Cardiovasc. Magn. Reson.* **17,** P239 (2015).

71. Doltra, A., Amundsen, B. H., Gebker, R., Fleck, E. & Kelle, S. Emerging concepts for myocardial late gadolinium enhancement MRI. *Curr. Cardiol. Rev.* **9,** 185–90 (2013).

72. Nag, A. C. Study of non-muscle cells of the adult mammalian heart: a fine structural analysis and distribution. *Cytobios* **28,** 41–61 (1980).

73. Porter, K. E. & Turner, N. A. Cardiac fibroblasts: at the heart of myocardial remodeling. *Pharmacol. Ther.* **123,** 255–278 (2009).

74. Dawson, K., Wu, C.-T., Qi, X. Y. & Nattel, S. Congestive heart failure effects on atrial fibroblast phenotype: differences between freshly-isolated and cultured cells. *PLoS One* **7,** e52032 (2012).

75. Chang, H. Y. *et al.* Diversity, topographic differentiation, and positional memory in human fibroblasts. *Proc. Natl. Acad. Sci. U. S. A.* **99,** 12877–12882 (2002).

76. Baum, J. & Duffy, H. S. Fibroblasts and Myofibroblasts : What are we talking

about ? *J. Cardiovasc. Pharmacol.* **57,** 376–379 (2012).

77. Hanna, N., Cardin, S., Leung, T.-K. & Nattel, S. Differences in atrial versus ventricular remodeling in dogs with ventricular tachypacing-induced congestive heart failure. *Cardiovasc. Res.* **63,** 236–244 (2004).

78. Burstein, B., Libby, E., Calderone, A. & Nattel, S. Differential behaviors of atrial versus ventricular fibroblasts: A potential role for platelet-derived growth factor in atrial-ventricular remodeling differences. *Circulation* **117,** 1630–1641 (2008).

79. Kardami, E. & Fandrich, R. R. Basic fibroblast growth factor in atria and ventricles of the vertebrate heart. *J. Cell Biol.* **109,** 1865–1875 (1989).

80. Kohl, P., Kamkin, A. G., Kiseleva, I. S. & Noble, D. Mechanosensitive fibroblasts in the sino-atrial node region of rat heart : interaction with cardiomyocytes and possible role. *Exp. Physiol.* **79,** 943–956 (1994).

81. Rook, M. B. *et al.* Differences in gap junction channels between cardiac myocytes , fibroblasts , and heterologous pairs. *Am. J. Physiol.* **263,** C959–77 (1992).

82. Gaudesius, G., Miragoli, M., Thomas, S. P. & Rohr, S. Coupling of cardiac electrical activity over extended distances by fibroblasts of cardiac origin. *Circ. Res.* **93,** 421–8 (2003).

83. Camelliti, P., Green, C. R., LeGrice, I. & Kohl, P. Fibroblast network in rabbit sinoatrial node: structural and functional identification of homogeneous and

heterogeneous cell coupling. *Circ. Res.* **94,** 828–835 (2004).

84. He, K. *et al.* Long-distance intercellular connectivity between cardiomyocytes and cardiofibroblasts mediated by membrane nanotubes. *Cardiovasc. Res.* **92,** 39–47 (2011).

85. Wu, C.-T. *et al.* Disease and region-related cardiac fibroblast potassium current variations and potential functional significance. *Cardiovasc. Res.* **102,** 487–96 (2014).

86. Shibukawa, Y., Chilton, E. L., Maccannell, K. A., Clark, R. B. & Giles, W. R. K+ currents activated by depolarization in cardiac fibroblasts. *Biophys. J.* **88,** 3924–35 (2005).

87. Kiseleva, I. *et al.* Electrophysiological properties of mechanosensitive atrial fibroblasts from chronic infarcted rat heart. *J. Mol. Cell. Cardiol.* **30,** 1083–1093 (1998).

88. Kamkin, A., Kiseleva, I. & Isenberg, G. Activation and inactivation of a non-selective cation conductance by local mechanical deformation of acutely isolated cardiac fibroblasts. *Cardiovasc. Res.* **57,** 793–803 (2003).

89. Wang, J., Chen, H., Seth, A. & McCulloch, C. a. Mechanical force regulation of myofibroblast differentiation in cardiac fibroblasts. *Am. J. Physiol. Heart Circ. Physiol.* **285,** H1871–H1881 (2003).

90. Miragoli, M., Gaudesius, G. & Rohr, S. Electrotonic modulation of cardiac impulse conduction by myofibroblasts. *Circ. Res.* **98,** 801–10 (2006).

91. Vasquez, C., Benamer, N. & Morley, G. E. The cardiac fibroblast: functional and electrophysiological considerations in healthy and diseased hearts. *J. Cardiovasc. Pharmacol.* **57,** 380–8 (2011).

92. Jacquemet, V. & Henriquez, C. S. Loading effect of fibroblast-myocyte coupling on resting potential, impulse propagation, and repolarization: insights from a microstructure model. *Am. J. Physiol. Heart Circ. Physiol.* **294,** H2040–52 (2008).

93. Maleckar, M. M., Greenstein, J. L., Giles, W. R. & Trayanova, N. a. Electrotonic coupling between human atrial myocytes and fibroblasts alters myocyte excitability and repolarization. *Biophys. J.* **97,** 2179–2190 (2009).

94. Sachse, F. B., Moreno, A. P. & Abildskov, J. a. Electrophysiological modeling of fibroblasts and their interaction with myocytes. *Ann. Biomed. Eng.* **36,** 41–56 (2008).

95. Jacquemet, V. & Henriquez, C. S. Modelling cardiac fibroblasts: interactions with myocytes and their impact on impulse propagation. *Europace* **9 Suppl 6,** vi29–37 (2007).

96. Zlochiver, S. *et al.* Electrotonic myofibroblast-to-myocyte coupling increases propensity to reentrant arrhythmias in two-dimensional cardiac monolayers. *Biophys. J.* **95,** 4469–4480 (2008).

97. Dierckx, H., Brisard, E., Verschelde, H. & Panfilov, A. V. Drift laws for spiral waves on curved anisotropic surfaces. *Phys. Rev. E. Stat. Nonlin. Soft Matter Phys.* **88,** 012908 (2013).

98. McDowell, K. S. *et al.* Methodology for patient-specific modeling of atrial fibrosis as a substrate for atrial fibrillation. *J. Electrocardiol.* **45,** 640–5 (2012).

99. Ho, S. Y., Anderson, R. H. & Sánchez-Quintana, D. Atrial structure and fibres: morphologic bases of atrial conduction. *Cardiovasc Res* **54,** 325–36 (2002).

100. Bieging, E., Morris, A., Cates, J., Marrouche, N. & McGann, C. Left atrial shape predicts recurrence after atrial fibrillation ablation. *J. Am. Coll. Cardiol.* **65,** A1294 (2015).

101. Cabo, C. *et al.* Vortex shedding as a precursor of turbulent electrical activity in cardiac muscle. *Biophys. J.* **70,** 1105–1111 (1996).

102. Klos, M. *et al.* Atrial Septopulmonary Bundle of the Posterior Left Atrium Provides a Substrate for Atrial Fibrillation Initiation in a Model of Vagally Mediated Pulmonary Vein Tachycardia of the Structurally Normal Heart. *Circ. Arrhythmia Electrophysiol.* **1,** 175–183 (2008).

103. Pandit, S. V & Jalife, J. Rotors and the dynamics of cardiac fibrillation. *Circ. Res.* **112,** 849–62 (2013).

104. Gray, R. A., Pertsov, A. M. & Jalife, J. Incomplete reentry and epicardial breakthrough patterns during atrial fibrillation in the sheep heart. *Circulation* **94,** 2649–2661 (1996).

105. Ho, S. Y. & Sánchez-Quintana, D. The importance of atrial structure and fibers. *Clin. Anat.* **22,** 52–63 (2009).

106. Aslanidi, O. V *et al.* Application of micro-computed tomography with iodine

staining to cardiac imaging, segmentation, and computational model development. *IEEE Trans. Med. Imaging* **32,** 8–17 (2013).

107. Cosio, F. G. *et al.* Electrophysiologic studies in atrial fibrillation. Slow conduction of premature impulses: a possible manifestation of the background for reentry. *Am. J. Cardiol.* **51,** 122–130 (1983).

108. Papageorgiou, P. *et al.* Site-dependent intra-atrial conduction delay. Relationship to initiation of atrial fibrillation. *Circulation* **94,** 384–389 (1996).

109. Platonov, P. G. *et al.* Further evidence of localized posterior interatrial conduction delay in lone paroxysmal atrial fibrillation. *Europace* **3,** 100–107 (2001).

110. Lalani, G. G. *et al.* Atrial Conduction Slows Immediately Before the Onset of Human Atrial Fibrillation. *J. Am. Coll. Cardiol.* **59,** 595–606 (2012).

111. Li, D., Fareh, S., Leung, T. K. & Nattel, S. Promotion of atrial fibrillation by heart failure in dogs: atrial remodeling of a different sort. *Circulation* **100,** 87–95 (1999).

112. Kawara, T. *et al.* Activation delay after premature stimulation in chronically diseased human myocardium relates to the architecture of interstitial fibrosis. *Circulation* **104,** 3069–75 (2001).

113. Jansen, J. A. *et al.* Arrhythmia Vulnerability of Aged Haploinsufficient Cx43 Mice is Determined by Heterogeneous Downregulation of Cx43 Combined with Increased Fibrosis. *Circulation* **118,** (2008).

114. Krul, S. P. J. *et al.* Atrial Fibrosis and Conduction Slowing in the Left Atrial Appendage of Patients Undergoing Thoracoscopic Surgical Pulmonary Vein Isolation for Atrial Fibrillation. *Circ. Arrhythmia Electrophysiol.* **8,** 288–295 (2015).

115. Tobón, C. *et al.* A Three-Dimensional Human Atrial Model with Fiber Orientation. Electrograms and Arrhythmic Activation Patterns Relationship. *PLoS One* **8,** e50883 (2013).

116. Seemann, G. *et al.* Heterogeneous three-dimensional anatomical and electrophysiological model of human atria. *Philos. Trans. A. Math. Phys. Eng. Sci.* **364,** 1465–1481 (2006).

117. Krueger, M. W. *et al.* Modeling Atrial Fiber Orientation in Patient-Specific Geometries : A Semi-automatic Rule-Based Approach. *Funct. Imaging Model. Hear.* **6666,** 223–232 (2011).

118. Harrild, D. & Henriquez, C. A computer model of normal conduction in the human atria. *Circ. Res.* **87,** E25–E36 (2000).

119. Yamamoto, M., Honjo, H., Niwa, R. & Kodama, I. Low-frequency extracellular potentials recorded from the sinoatrial node. *Cardiovasc. Res.* **39,** 360–372 (1998).

120. Liu, T. Y. *et al.* Functional characterization of the crista terminalis in patients with atrial flutter: Implications for radiofrequency ablation. *J. Am. Coll. Cardiol.* **43,** 1639–1645 (2004).

121. Hansson, A. *et al.* Right atrial free wall conduction velocity and degree of anisotropy in patients with stable sinus rhythm studied during open heart surgery. *Eur. Heart J.* **19,** 293–300 (1998).

122. Kléber, A. G., Janse, M. J. & Fast, V. G. in *Comprehensive Physiology* (John Wiley & Sons, Inc., 2011). doi:10.1002/cphy.cp020112

123. Koura, T. *et al.* Anisotropic conduction properties in canine atria analyzed by high-resolution optical mapping: Preferential direction of conduction block changes from longitudinal to transverse with increasing age. *Circulation* **105,** 2092–2098 (2002).

124. Verheule, S. *et al.* Loss of continuity in the thin epicardial layer because of endomysial fibrosis increases the complexity of atrial fibrillatory conduction. *Circ. Arrhythmia Electrophysiol.* **6,** 202–211 (2013).

125. Angel, N. *et al.* Diverse Fibrosis Architecture and Premature Stimulation Facilitate Initiation of Reentrant Activity Following Chronic Atrial Fibrillation. *J. Cardiovasc. Electrophysiol.* **26,** 1352–1360 (2015).

126. Ellis, W. S., SippensGroenewegen, A., Auslander, D. M. & Lesh, M. D. The role of the crista terminalis in atrial flutter and fibrillation: a computer modeling study. *Ann. Biomed. Eng.* **28,** 742–754 (2000).

127. Labarthe, S., Coudiere, Y., Henry, J. & Cochet, H. A Semi-Automatic Method To Construct Atrial Fibre Structures : a Tool for Atrial Simulations. *CINC - Comput. Cardiol.* 881–884 (2012).

128. Haïssaguerre, M. *et al.* Spontaneous initiation of atrial fibrillation by ectopic beats originating in the pulmonary veins. *N. Engl. J. Med.* **339,** 659–66 (1998).

129. Tsai, C. F. *et al.* Initiation of atrial fibrillation by ectopic beats originating from the superior vena cava: electrophysiological characteristics and results of radiofrequency ablation. *Circulation* **102,** 67–74 (2000).

130. Benson, a. P., Gilbert, S. H., Li, P., Newton, S. M. & Holden, A. V. Reconstruction and Quantification of Diffusion Tensor Imaging-Derived Cardiac Fibre and Sheet Structure in Ventricular Regions used in Studies of Excitation Propagation. *Math. Model. Nat. Phenom.* **3,** 101–130 (2008).

131. Lemery, R. *et al.* Normal atrial activation and voltage during sinus rhythm in the human heart: An endocardial and epicardial mapping study in patients with a history of atrial fibrillation. *J. Cardiovasc. Electrophysiol.* **18,** 402–408 (2007).

132. Chang, H.-Y. *et al.* Sinus node dysfunction in atrial fibrillation patients: the evidence of regional atrial substrate remodelling. *Europace* **15,** 205–211 (2013).

133. Gray, R. A., Pertsov, A. M. & Jalife, J. Spatial and temporal organization during cardiac fibrillation. *Nature* **392,** 75–78 (1998).

134. Chen, J. *et al.* Dynamics of wavelets and their role in atrial fibrillation in the isolated sheep heart. *Cardiovasc. Res.* **48,** 220–232 (2000).

135. Spach, M. S., Dolber, P. C. & Heidlage, J. F. Interaction of inhomogeneities of

repolarization with anisotropic propagation in dog atria. A mechanism for both preventing and initiating reentry. *Circ. Res.* **65,** 1612–1631 (1989).

136. McGann, C. *et al.* Atrial fibrillation ablation outcome is predicted by left atrial remodeling on MRI. *Circ. Arrhythmia Electrophysiol.* **7,** 23–30 (2014).

137. Rutherford, S. L., Trew, M. L., Sands, G. B., Legrice, I. J. & Smaill, B. H. High-resolution 3-dimensional reconstruction of the infarct border zone: Impact of structural remodeling on electrical activation. *Circ. Res.* **111,** 301–311 (2012).

138. Lau, D. H. *et al.* Novel mechanisms in the pathogenesis of atrial fibrillation: practical applications. *Eur. Heart J.* ehv375– (2015). doi:10.1093/eurheartj/ehv375

139. Marrouche, N. F. *et al.* Association of atrial tissue fibrosis identified by delayed enhancement MRI and atrial fibrillation catheter ablation: the DECAAF study. *JAMA* **311,** 498–506 (2014).

140. Gal, P. & Marrouche, N. F. Magnetic resonance imaging of atrial fibrosis: redefining atrial fibrillation to a syndrome. *Eur. Heart J.* ehv514 (2015). doi:10.1093/eurheartj/ehv514

141. Jadidi, A. S. *et al.* Inverse relationship between fractionated electrograms and atrial fibrosis in persistent atrial fibrillation: combined magnetic resonance imaging and high-density mapping. *J. Am. Coll. Cardiol.* **62,** 802–12 (2013).

142. Roten, L., Derval, N. & Jaïs, P. Catheter ablation for persistent atrial fibrillation: Elimination of triggers is not sufficient. *Circ. Arrhythmia*

*Electrophysiol.* **5,** 1224–1231 (2012).

143. Hunter, R. J. *et al.* Characterization of fractionated atrial electrograms critical for maintenance of atrial fibrillation a randomized, controlled trial of ablation strategies (the CFAE AF trial). *Circ. Arrhythmia Electrophysiol.* **4,** 622–629 (2011).

144. Takahashi, Y. *et al.* Characterization of Electrograms Associated With Termination of Chronic Atrial Fibrillation by Catheter Ablation. *J. Am. Coll. Cardiol.* **51,** 1003–1010 (2008).

145. Peters, N. S., Coromilas, J., Severs, N. J. & Wit, A. L. Disturbed connexin43 gap junction distribution correlates with the location of reentrant circuits in the epicardial border zone of healing canine infarcts that cause ventricular tachycardia. *Circulation* **95,** 988–996 (1997).

146. Vigmond, E. *et al.* Towards predictive modelling of the electrophysiology of the heart. *Exp. Physiol.* **94,** 563–577 (2009).

147. Dosdall, D. J. *et al.* Chronic atrial fibrillation causes left ventricular dysfunction in dogs but not goats: experience with dogs, goats, and pigs. *Am. J. Physiol. Heart Circ. Physiol.* **305,** H725–31 (2013).

148. Bauer, A., McDonald, A. D. & Donahue, J. K. Pathophysiological findings in a model of persistent atrial fibrillation and severe congestive heart failure. *Cardiovasc. Res.* **61,** 764–770 (2004).

149. Lin, C.-S. *et al.* Increased expression of extracellular matrix proteins in rapid

atrial pacing-induced atrial fibrillation. *Heart Rhythm* **4,** 938–949 (2007).

150. Lin, J.-L. *et al.* Electrophysiological mapping and histological examinations of the swine atrium with sustained (> or =24 h) atrial fibrillation: a suitable animal model for studying human atrial fibrillation. *Cardiology* **99,** 78–84 (2003).

151. Ho, S. Y. *et al.* Architecture of the pulmonary veins: relevance to radiofrequency ablation. *Heart* **86,** 265–270 (2001).

152. McGann, C. J. *et al.* New magnetic resonance imaging-based method for defining the extent of left atrial wall injury after the ablation of atrial fibrillation. *J. Am. Coll. Cardiol.* **52,** 1263–1271 (2008).

153. Karim, R. *et al.* Automatic Segmentation of Left Atrial Scar from Delayed-Enhancement Magnetic Resonance Imaging. in *Functional Imaging and Modeling of the Heart - 6th International Conference* 63–70 (2011). doi:10.1007/978-3-642-21028-0_8

154. Benito, E. *et al.* Left atrial fibrosis quantification by late gadolinium enhancement MRI: can we find the optimal normalized thresholds. in *Europace,* 17 (suppl 3) iii89–iii91; (2015). doi:10.1093/europace/euv159

155. Aras, D. *et al.* Inadvertent puncture of the aortic noncoronary cusp during postoperative left atrial tachycardia ablation. *J. arrhythmia* **31,** 235–237 (2015).

156. Han, S. & Hwang, C. How to Achieve Complete and Permanent Pulmonary

Vein Isolation without Complications. *Korean Circ. J.* **44,** 291–300 (2014).

157. Lemola, K. *et al.* Computed tomographic analysis of the anatomy of the left atrium and the esophagus: implications for left atrial catheter ablation. *Circulation* **110,** 3655–3660 (2004).

158. Biktasheva, I. V, Dierckx, H. & Biktashev, V. N. Drift of scroll waves in thin layers caused by thickness features: asymptotic theory and numerical simulations. *Phys. Rev. Lett.* **114,** 68302 (2015).

159. Labarthe, S. *et al.* A bilayer model of human atria: mathematical background, construction, and assessment. *Eur. Eur. pacing, arrhythmias, Card. Electrophysiol. J. Work. groups Card. pacing, arrhythmias, Card. Cell. Electrophysiol. Eur. Soc. Cardiol.* **16 Suppl 4,** iv21–iv29 (2014).

160. Wi, J. *et al.* Complex fractionated atrial electrograms related to left atrial wall thickness. *J. Cardiovasc. Electrophysiol.* **25,** 1141–1149 (2014).

161. Park, J. *et al.* Left atrial wall thickness rather than epicardial fat thickness is related to complex fractionated atrial electrogram. *International journal of cardiology* **172,** e411–3 (2014).

162. Platonov, P. G., Ivanov, V., Ho, S. Y. & Mitrofanova, L. Left atrial posterior wall thickness in patients with and without atrial fibrillation: data from 298 consecutive autopsies. *J. Cardiovasc. Electrophysiol.* **19,** 689–692 (2008).

163. Sanchez-Quintana, D. *et al.* The terminal crest: morphological features relevant to electrophysiology. *Heart* **88,** 406–411 (2002).

164. Sanchez-Quintana, D. *et al.* Anatomic relations between the esophagus and left atrium and relevance for ablation of atrial fibrillation. *Circulation* **112,** 1400–1405 (2005).

165. Hall, B. *et al.* Variation in left atrial transmural wall thickness at sites commonly targeted for ablation of atrial fibrillation. *J. Interv. Card. Electrophysiol.* **17,** 127–132 (2006).

166. Ho, S. Y., Sanchez-Quintana, D., Cabrera, J. A. & Anderson, R. H. Anatomy of the left atrium: implications for radiofrequency ablation of atrial fibrillation. *J. Cardiovasc. Electrophysiol.* **10,** 1525–1533 (1999).

167. Deneke, T. *et al.* Histopathology of intraoperatively induced linear radiofrequency ablation lesions in patients with chronic atrial fibrillation. *Eur. Heart J.* **26,** 1797–1803 (2005).

168. Hassink, R. J., Aretz, H. T., Ruskin, J. & Keane, D. Morphology of atrial myocardium in human pulmonary veins: a postmortem analysis in patients with and without atrial fibrillation. *J. Am. Coll. Cardiol.* **42,** 1108–1114 (2003).

169. Wolf, C. M. *et al.* Atrial remodeling after the Fontan operation. *Am. J. Cardiol.* **104,** 1737–1742 (2009).

170. Becker, A. E. Left atrial isthmus: anatomic aspects relevant for linear catheter ablation procedures in humans. *J. Cardiovasc. Electrophysiol.* **15,** 809–812 (2004).

171. Schwartzman, D., Schoedel, K., Stolz, D. B. & Di Martino, E. Morphological

and mechanical examination of the atrial 'intima'. *Europace* **15,** 1557–61 (2013).

172. Beinart, R. *et al.* Left atrial wall thickness variability measured by CT scans in patients undergoing pulmonary vein isolation. *J. Cardiovasc. Electrophysiol.* **22,** 1232–1236 (2011).

173. Nakamura, K. *et al.* Left atrial wall thickness in paroxysmal atrial fibrillation by multislice-CT is initial marker of structural remodeling and predictor of transition from paroxysmal to chronic form. *Int. J. Cardiol.* **148,** 139–147 (2011).

174. Imada, M. *et al.* Anatomical remodeling of left atria in subjects with chronic and paroxysmal atrial fibrillation evaluated by multislice computed tomography. *International journal of cardiology* **119,** 384–388 (2007).

175. Hoffmeister, P. S. *et al.* Evaluation of left atrial and posterior mediastinal anatomy by multidetector helical computed tomography imaging: relevance to ablation. *J. Interv. Card. Electrophysiol.* **18,** 217–223 (2007).

176. Pan, N.-H., Tsao, H.-M., Chang, N.-C., Chen, Y.-J. & Chen, S.-A. Aging dilates atrium and pulmonary veins: implications for the genesis of atrial fibrillation. *Chest* **133,** 190–196 (2008).

177. Suenari, K. *et al.* Left atrial thickness under the catheter ablation lines in patients with paroxysmal atrial fibrillation: insights from 64-slice multidetector computed tomography. *Heart Vessels* **28,** 360–368 (2013).

178. Lerch, J. P. & Evans, A. C. Cortical thickness analysis examined through power analysis and a population simulation. *Neuroimage* **24,** 163–173 (2005).

179. Xu, C. & Prince, J. L. Snakes, shapes, and gradient vector flow. *IEEE Trans. Image Process.* **7,** 359–369 (1998).

180. Marta Varela, Ross Morgan, Adeline Theron, Madalena Peyroteo, Leonor Piqueiro, M. & Henningsson, Paul Aljabar, Christoph Kolbitsch, Tobias Schaeffter, O. A. Atlas of atrial wall thickness as a tool for catheter ablation procedures. in *Atrial Signals 2015 meeting* (2015).

181. Bishop, M. *et al.* Three-dimensional atrial wall thickness maps to inform catheter ablation procedures for atrial fibrillation. *Europace* **18,** 376–83 (2016).

.